UNIVERSITY OF CALIFORNIA
RIVERSIDE

# Nanoscience for Public Health: Applications for ZrN and YSZ

A Dissertation submitted in partial satisfaction
of the requirements for the degree of

Doctor of Philosophy

in

Mechanical Engineering

by

Chris Rudnicki

September 2023

Dissertation (use Thesis for Master's) Committee:
Dr. Lorenzo Mangolini
Dr. Richard Wilson
Dr. Bhargav Rallabandi

The Dissertation of Chris Rudnicki is approved:

---

---

---

Committee Chairperson

University of California, Riverside

ACKNOWLEDGEMENTS:

I acknowledge previously published work has been used in its entirety from the Journal of Nanoparticle Research, volume 22, February 2020 (Chapter 4). I am the primary contributor to this article, while Dr. Exarhos, Dr. Mangolini are also acknowledged as contributors. Crystal Mariano is acknowledged as a contributing undergraduate research assistant.

I also acknowledge that previously published work has been reprinted or partially reprinted from the journal ACS Applied Bio Materials, volume 108, June 2020 (Chapter 5). I am the primary contributor to this article while Changlu Xu, Dr. Uahengo, Dr. Halaney, Dr. Garay, Dr. Mangolini, Dr. Aguilar, and Dr. Liu are also acknowledged as contributors.

I acknowledge Dr. Mangolini for without his guidance and instruction this work would not have been possible.

I acknowledge Dr. Schwan and the rest of my labmates who always provided help and support when needed.

I acknowledge the senior graduate students and post doctorates during my work Dr. Exarhos, Dr. Alvarez Barragan, Dr. Nava and Dr. Berrospe Rodriguez for without their training and contribution this work would not be possible.

I also acknowledge Andres, Mae, Pedro and the rest of my loved ones whom without their support this work would not be completed.

to a previous evolution

ABSTRACT OF THE DISSERTATION

Nanoscience for Public Health: Applications for ZrN and YSZ

by

Chris Rudnicki

Doctor of Philosophy, Graduate Program in Mechanical Engineering
University of California, Riverside, September 2023
Dr. Lorenzo Mangolini, Chairperson

The interaction of light with a small metallic particle creates a strong local electromagnetic wave that can be exploited in the public health arena for photochemistry, biosensing, drug delivery and more. In this dissertation, I discuss the synthesis and application of two different nanoparticles for public health, zirconium nitride (ZrN) and yttria-stabilized zirconia (YSZ). ZrN is investigated as an alternative plasmonic material to efficiently convert the sun's visible radiation into chemical energy to remove heavy metals from water. The photothermal and photelectric mechanisms of plasmonic ZrN particles are considered and characterized. YSZ is proposed as a ceramic cranial implant for the improvement of diagnostic and treatments of brain disorders. YSZ nanoparticles synthesized with an Aerosol Spray Pyrolysis system are densified with a Spark-Plasma Sintering process to obtain dense bulk nanostructure. I work to optimize the mechanical properties of 3YSZ with the optical properties of 8YSZ. Additionally, I comment on the potential for nanotechnology to contribute to public health.

Table of Contents

Chapter 1: Introduction ..... 1

1.1: Nanotechnology for Public Health ..... 1

1.2: Nanotechnology Background ..... 2

1.3: Light-matter Interactions ..... 4

1.5: Dissertation Direction ..... 11

1.6: References ..... 15

Chapter 2: Plasmonic Zirconium Nitride Nanoparticles for Light-driven Cr (VI) Reduction ..... 18

2.1: Introduction ..... 18

2.2: Experimental Methods ..... 21

2.3: Results and Discussion ..... 29

2.4: Conclusions ..... 47

2.5: References ..... 49

Chapter 3: Plasmonic Nanoparticle Photochemistry with Methanol ..... 57

3.1: Introduction ..... 57

3.2: Platinum Experimental Methods ..... 60

3.3: Platinum Results and Discussion ..... 62

3.4: Cr (VI) Experimental Methods ..... 67

3.5: Cr (VI) Reduction Results and Discussion ..... 68

3.6: Conclusions ..... 73

3.7: References ..... 75

Chapter 4: Spray Pyrolysis of Yttria-Stabilized Zirconia Nanoparticles and Their Densification into Bulk Transparent Windows ..... 78

4.1: Introduction ..... 78

4.2: Experimental Methods ..... 80

4.3: Results and Discussion ..... 84

4.4: Conclusions ..... 91

4.5: References ..... 93

Chapter 5: Nanocrystalline Yttria-Stabilized Zirconia for Cranial Widow Applications . 97

5.1: Introduction ..... 97

5.2: Experimental Methods ..... 99

5.3: Results and Discussion ..... 106

5.4: Conclusions ..... 121

5.5: References ..... 123

Chapter 6: Conclusion and Outlook ..... 126

List of Figures

Chapter 1:

1.1. Schematic of Local dipole due to an external electric field. ..... 4

1.2. Schematic of Localized surface plasmon resonance (LSPR). ..... 8

Chapter 2:

2.1. Photograph of the plasma reactor and cross-section efficiency of ZrN ..... 21

2.2. Setup of Cr (VI) photocatalytic experiments.. ..... 22

2.3. Optical spectrum of Hg-Xe Arc Lamp. ..... 24

2.4. The diphenyl carbazide absorbance spectrum. ..... 25

2.5. Calibration curve for the diphenyl carbazide method ..... 26

2.6. XRD analysis and TEM image of ZrN nanoparticles ..... 29

2.7. The absorbance of .005 g/L of ZrNand $TiO_2$. ..... 30

2.8. Absorbance of 1 g/L of ZrN and $TiO_2$ ..... 31

2.9. Cr (VI) Reduction, Quantum Yield and Power studies ..... 35

2.10. Power Fit Cr(VI) reduction with ZrN ..... 36

2.11. Cr (VI) Reduction study with 500 mg/L of ZrN and $TiO_2$. ..... 37

2.12. Dark reduction of Cr (VI) and Ttemperature vs. Illumination Power ..... 39

2.13. Z-scan measurement and table of nonlinear Coefficients. ..... 41

2.14. Extinction of ZrN nanoparticles and XPS data before and after illumination ..... 44

2.15. Full XPS Spectrum for ZrN ..... 44

2.16. XPS data of ZrN particle control and cumulative fit ..... 46

Chapter 3:

3.1. Schematic of Pt deposition experiments .....59

3.2. The absorbance spectrum of ZrN and TiN .....61

3.3. TEM Images of Pt deposited on to the ZrN nanoparticles. .....63

3.4. Pt-Zr (Ti) atomic ratio vs. photo plating time .....64

3.5. Absorption of ZrN nanoparticles and Action plot with Pt-Zr ratio .....65

3.6. Cr (VI) Reduction Time Study. .....66

3.7. Cr (VI) Reduction vs Illumination Power .....69

3.8. Action Plot showing the Quantum Yield for ZrN and $TiO_2$ .....71

Chapter 4:

4.1. Schematic of the YSZ aerosol spray pyrolysis synthesis apparatus. .....80

4.2. EDS composition and crystallite size of YSZ .....82

4.3. Raman spectra XRD pattern of YSZ. .....83

4.4. TEM image and particle size distribution of YSZ .....84

4.5. Air annealing optical transmission experiment 8YSZ .....86

4.6. Air annealing crystal structure characterization 8YSZ and 6YSZ .....86

4.7. Transmission of 8YSZ and 6YSZ. .....88

4.8. SEM images of the cross section YSZ sintered samples .....89

4.9. Table of 8YSZ and 6YSZ mechanical properties .....89

Chapter 5:

5.1. Schematics of the BMSCs under direct and indirect contact conditions. .....103

5.2. Photographs the transparent YSZ discs. .....106

5.3. Surface morphologies before and after polishing. .....109

5.4. Surface roughness and contact angles of YSZ discs. .....110

5.5. Fluorescence images after 24-hour direct culture .....111

5.6. Spreading areas and aspect ratios of BMSC adhered on discs. .....113

5.7. Direct and Indirect contact densities of BMSCs. .....114

5.8. pH values and ion concentrations of post culture media .....117

5.9. XRD of YSZ after cell cycle .....119

List of Equations

Chapter 1:

1.1. Dipole Moment Equation.....5

1.2. Oscilator Motion Equation.....5

1.3. Lorentz Model.....6

1.4. Dielectric function Equation.....6

1.5. Drude Model .....9

1.6. Mie Theory dipole approximation .....10

1.7. Normalize Absorption cross section .....11

1.8. Normalized Scattering cross section.....11

Chapter 2:

2.1. Calculating absorption of diphenyl carbazide.....27

2.2. Langmuir-Hinshelwood kinetics expression.....33

2.3. Reduction half reaction of Cr (VI) .....33

2.4. Oxidation half reaction of water .....34

2.5. Quantum Yield .....36

2.6. Non Linear Absorption Coefficient .....42

2.7. Interfacial heat transfer coefficient .....43

Chapter 3:

3.1. Arrhenius Law .....57

3.2. Calculated nanoparticle teamperature.....58

3.3. Platinum Reduction .....62

3.4. Oxidation of Methanol .....62

3.5. Cr (VI) reduction rate kinetics .....68

3.6. Cr (VI) reduction half reaction .....68

3.7. Oxidation of methanol half reaction .....68

Chapter 5:

5.6. Beer-Lambert Law .....101

# Chapter 1: Introduction

## 1.1: Nanotechnology for Public Health

Nanotechnology has the great potential to improve healthcare techniques because many viruses, including the COVID virus, are somewhere between 50-200 nm in size. During the COVID emergencies in 2020, we witnessed a public health emergency unfolding which increased the risk of the community as well as one's personal health. Developing nanotechnology is important to be ready for future infectious disease emergencies by improving diagnostic techniques, therapeutics, and preventing infections from happening in the first place.[1] Nanotechnology generally has the potential to provide technological innovation in all the core disciplines of public health: epidemiology, biostatistics, health policy management, social and community behavior and environmental health sciences.[2]

The study of materials and their properties over time looked at smaller and smaller scales eventually engineering on the nanoscale, although not stopping at materials generally considered between 10-100 nm in size but sometimes up to 1000 nm. The study of specific nanomaterials is called nanoscience and the use of that knowledge for public health applications in this dissertation contributes are denoted to nanotechnologies.

The rich world on the nanoscale includes a number of natural examples like enzymes, cell membranes, spider silks, and nanoclays. The chemical reactions and processes that contribute to complicated life are monitored by neurons on the nanoscale for the homeostasis with which biological systems live. The colors we evolved to see have

wavelengths that are hundreds of nanometers in size but if they become shorter or longer, we can no longer see them.

Both the material and the structure of that material are important for determining the properties of that thing. Nanostructured materials have different properties than their bulk counterparts in part because as the radius, r, gets smaller; the ratio of their surface area ($\sim r^2$) to volume ($\sim r^3$) increases rapidly. The interior atoms of nanostructured spheres or cylinders are stable because they contain more atoms on the surface of the structure which can also be leveraged for a number of applications.[3] Particular ratios of surface area to volume also appear to be something bacteria seeks to maintain balance and stability.[4]

The nanostructured materials are typically divided into five categories: metal, lipid, ceramic, polymeric and semiconductors.[5] Converging nanotechnologies with biomedical fields holds potential to improve both diagnostic techniques as well as treatments in the healthcare sector. Depending on the material of nanoparticle, they are able to leverage their large surface area to engineer other chemicals onto.

### 1.2: Nanotechnology Background

The word ‘atom’ come from words in ancient Greece meaning “indivisible” but in 1897, J. J. Thompson broke those atoms down now into smaller parts first by measuring the mass of electrons and then a few years later describing the nucleus made of protons and neutrons. The search for the fundamental building blocks continued with modern technology, breaking down those subatomic particles further into quarks. Although likely without

knowledge on nanotechnology, a number of ancient artifacts were making use out of the macroscale effects of nanoparticles.

The Lycurgus Cup is one such artifact that people wondered and speculated for centuries with its extraordinary artistic aspects and for the optical properties of the glass. When the light source is reflected back a green color decorates the cup but when the light is transmitting through, the cup appears red. The dichroic effect describes perceiving two different colors depending on where the light source is located which it did not seem intentionally possible for engineers a century ago to do in this with silver and gold colloids.[6] It was not until Mie came along in the mid-1900s would we begin to understand the optical properties of the cup.

Two other ancient materials were later discovered to contain nanostructures that improved the quality; Damascus sabers and luster from medieval pottery. The blades contained cementite ($Fe_3C$) particles which contributed to the increased strength of the blade.[7] The luster from the 9$^{th}$ century, was a 10-20 nm metal free thin film while there were metal nanocrystals imbedded into the glass below providing both protection for the pottery as well as contributing to the optical beauty.[8] Medieval artisans were able to reproduce these materials making them to be the first nanotechnologists.

In 20$^{th}$ century, a physicist Richard Feynman advocated for developing the technologies to investigate the different properties for nanostructured materials than their bulk counterparts.[9] These lectures were not the start of but encouraged innovation in developing technologies and contributed to what is described as 1970s Moors law where the number of transistors inside an integrated circuit doubled roughly every two years. The process of

creating more powerful computers that can fit inside your pocket than the computers that first allowed people to go to the moon is driven by nanotechnology.

There is great potential for nanotechnology our computing power but research on exposure to nanomaterials via food, water, or medical applications has shown adverse effects on the body but is still ongoing.[10] Some researchers are arguing for precaution until more information is known when there could be permanent damage handling these materials and looking to address the nanomaterial complexities to understand and minimize the hazards.[11,12] Life cycle assessment studies suggest many synthesis methods are not energy efficient causing a large impact on the climate crisis.[13]

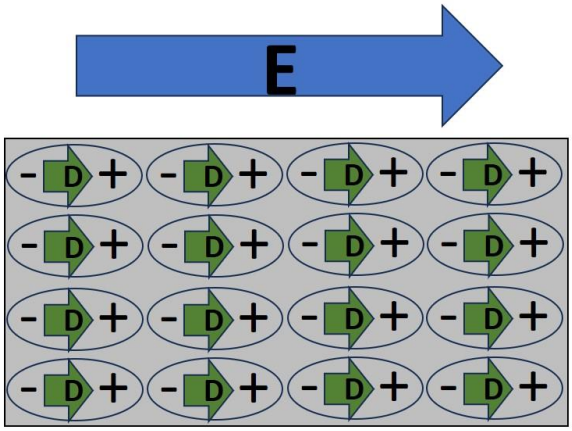


*Figure 1.1. Local dipole field due to an external electric field.*

### 1.3: Light-matter Interactions

The small part of the spectrum of light that comes from the sun that we evolved to see, wavelengths 400 – 900 nanometers spanning from blue to red, color our daily life with light matter interactions. Common phenomenon such as visible light mostly transmitting

through widows or reflecting off many metals giving them an opaque or shinny color. Even the light we cannot see like ultraviolet light (UV, 100-400 nm) and near infrared light (NIR, 700-1400 nm) is perceptible by feeling the heat of asphalt on a summer day.

As a material is placed in a static electric field, the negatively charged electron cloud with the positively charged nucleus interact with the electric field and polarize the atom. As shown in figure 1, the local microscopic displacement dipole is described by:

$$D = \varepsilon_r \varepsilon_0 E \quad (1.1)$$

Where D is the electric displacement of the material, $\varepsilon_0$ is the permittivity of free space, $\varepsilon_r$ is the relative permittivity of the material or the ability of it to hold that energy from the electromagnetic wave related to restoring force and mass of the electrons and protons within the lattice. When the macroscopic electric field starts to oscillate with a particular frequency though, the interactions between neighboring dipoles gives rise to a local electric field that felt more strongly.

A classical theory of optical properties, the Lorentz model, treats the relationship between the electrons and nucleus like that of a spring or a harmonic oscillator that is driven by the force applied from an electromagnetic field. Each oscillator, a mass m and a charge $e$, that is acted on by the electromagnetic field also has a restoring force K much like a spring and x is the displacement from equilibrium. The local field then is dependent on all the identical, independent harmonic oscillators and the motion of them can be described by:

$$m\ddot{\mathrm{x}} + b\dot{\mathrm{x}} + K\mathrm{x} = eE_{local} \quad (1.2)$$

Where the local field $E_{local}$ is the field that is "seen" by a single oscillator which is different than the macroscopic field E which contains the average of all the dipoles. The damping force is $b\dot{x}$, where b is the damping constant. The solution to equation 2 contains a transient part that dies away due to damping and another more interesting oscillatory part with the same frequency as the driving field.

Equipped with the solution to a single oscillator, the dipole moment of a given unit volume is going to follow from the number of oscillators times the charge they carry. From those larger polarizations, the dielectric function, or the material response to a given electromagnetic field from the system of simple harmonic oscillators is:

$$\varepsilon = 1 + \frac{\omega_p^2}{\omega_0^2 - \omega^2 - i\gamma\omega} \qquad (1.3)$$

Where $\omega_p$ is the plasma frequency defined by $\omega_p = \sqrt{Ne^2/m\varepsilon_0}$ , $\omega_0 = \sqrt{K/m}$ and $\gamma = b/m$. The dielectric function contains both real and imaginary parts and many of optical characteristics can be deduced from this simple model. There is a region of high absorbance at frequencies around the resonance frequency $\omega_0$ and also has an associated region of high reflectance with frequencies slightly higher given that $K \gg 1$. Absorption occurs when the oscillations of electrons grow large and the dissipation of that energy from the oscillation goes into the lattice of the material (phonons).

Generally, the real and imaginary parts of the dielectric function are described by:

$$\varepsilon(\omega) = \varepsilon_1(\omega) - i\varepsilon_2(\omega) \qquad (1.4)$$

Where ω is the frequency of light, $\varepsilon_1$ is the real part of the permittivity and $\varepsilon_2$ is the imaginary part of the permittivity meaning that they represent the polarizability and the loss of energy in the medium respectively.

It is important to note that $\varepsilon_1$ and $\varepsilon_2$ both depend on the frequency of light and also are not independent of one another. The maximum value of $\varepsilon_2$ occurs approximately at $\omega_0$ and provided that $\gamma \gg \omega_0$ there will also be a region of high reflectance at frequencies slightly larger than $\omega_0$. At sufficiently high frequencies, $\varepsilon_1$ will approach the free space value as none of the polarization mechanisms of the material are able to respond. At the low frequencies, much lower than the resonance frequency, the imaginary part will approach zero and the real part of the dielectric function will approach a constant that depends on the materials number density of oscillators and their masses.

A prevalent example is that of glass, $SiO_2$, where the resonant frequency of the electron shells is in the far UV part of the spectrum but by inserting some impurities the resonance frequency can be lowered to closer to the visible part of the spectrum. Visible light has a relatively low frequency oscillations compared with UV light and therefore the amplitude of the charge oscillations in glass is relatively small making the material mostly transparent and slightly reflecting. Adding too many impurities would result in an even lower resonant frequency that would start to have absorption features with visible light rather than providing a window.

**1.4: Plasmonic Nanoparticles**

Metal nanoparticles smaller than the wavelength of light impinging on them like those found in the Lycurgus Cup interact with light differently than their bulk counterparts. In

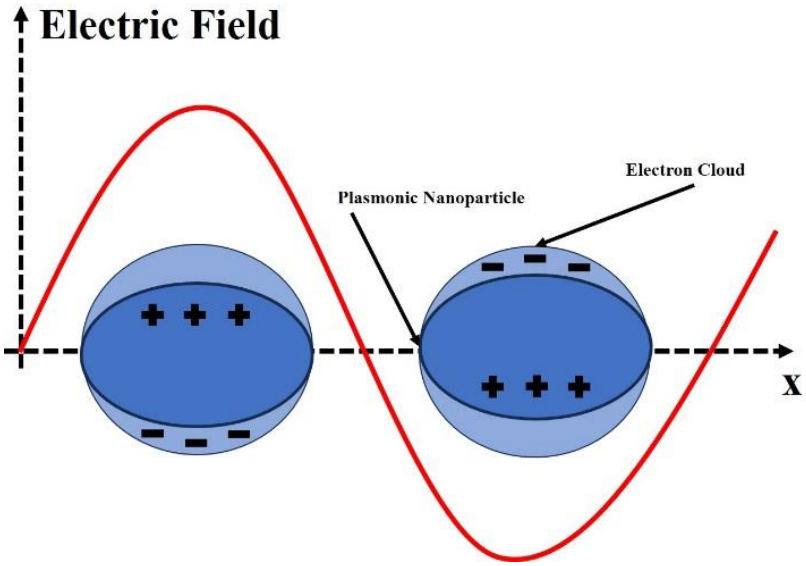


*Figure 2. Localized surface plasmon resonance (LSPR) of a plasmonic nanoparticle. The nanoparticle size is similar to that of the wavelength of light the collective oscillations of electrons produce a strong localized electromagnetic field.*

the mid-1800s, Michael Faraday produced a solution of extremely small gold particles, that turned out to be nanoparticles, and observed a red color that was different than the bulk property of gold. Understanding the properties of small metallic nanoparticles start with the optical differences between insulators which tend to be transparent to visible light while metals tend to be reflecting of light with that same energy.

The difference in the electric band structure of conductors vs. non-conductors of electricity are markedly different and greatly contribute to the understanding of optical properties in a material. Insulators typically have a large band gap where there is a forbidden energy gap between an energy band completely filled with electrons and another that is empty. Metals on the other hand have energy bands that are completely filled and overlap with other empty energy bands. This overlay of energy bands allows for an absorption mechanism of

low frequency photons in metals whereas non-conductors or insulators require a photon with greater energy than their band gap for absorption to occur.

The electrons in metals are easily able to get excited into higher energy states due to the band structure and therefore are often referred to as "free". The result is that we can consider the K value in our simple harmonic oscillator model to be zero, the restoring force of electrons in metals is small and therefore $\omega_0 = 0$. Following the model from Lorentz, the dielectric function modeling the oscillation of electrons in a metal was described by Drude[14]:

$$\varepsilon(\omega) = 1 - \frac{\omega_p^2}{(\omega^2 + i\gamma\omega)} \qquad (1.5)$$

Where $\omega_p$ is the plasma frequency, and $\gamma$, the damping coefficient, relates to how strongly the material's nuclei holds onto electrons. The plasma frequency was used before but within metal it corresponds to the collective longitudinal oscillations due to long range coulomb forces of the electron gas at frequencies when the dielectric function is zero. Since the overall charge of the metal is zero, the nonuniform charge distribution due to the electromagnetic wave produces electron momentum causing them to overshoot the equilibrium position.

This collective oscillation is called a plasmon, or a quanta of plasma oscillations, if the lifetime is sufficiently large $(\omega_p \tau \gg 1)$. Where $\gamma$ is related to the average time between collisions which in the bulk metal is manly electron-phonon scattering. As the particles get smaller, electron-surface scattering starts to become more important and $\gamma$ can be modeled as a function of the radius of the particle. This model of the dielectric function is able to

account for nanoparticles in the 10-100 nm range and the plasmon resonances in the visible part of the spectrum

Electromagnetic theories from Maxwell applied to particles smaller than the wavelength of light determined that the particle resonance frequency from both the material properties, including the density of electrons, the effective electron mass, and also the structure like the size and shape of the charge distribution.[15] By changing the geometry, materials, and also by changing the surroundings of the particle, the plasmonic resonant frequency could be synthesized for specific wavelengths.

Mie, the first do to so successfully, use an electric dipole approximation to describe what became known as surface plasmons or LSPR (figure 2) and further described the transverse electric field modes. Much like a particle in a box, the separation between energy levels increases with decreasing size which for a metal nanoparticle creates a small energy separation in the conduction band. The ensuing net charge difference at the surface of the particle from the electromagnetic wave changes the polarizability of the metal to resonance at optical frequencies. By assuming the bulk dielectric constant of the material applied to the nanoscale and using the boundary conditions of a small spherical object, Mie determined the extinction cross section of the nanoparticle to be roughly[16]:

$$\sigma_{ext} \sim \frac{\varepsilon_2}{[\varepsilon_1(\omega)+2\varepsilon_m(\omega)]^2+\varepsilon_2(\omega)^2} \qquad (1.6)$$

Where $\varepsilon_m$ is the relative permittivity of the surrounding medium and $\omega$ is the frequency of the impinging light. The real and imaginary parts of the dielectric function of the material are, $\varepsilon_1$, and $\varepsilon_2$ respectively.

For sufficiently small spherical particles meaning that the particle's circumference is less than the wavelength of light, Mie theory approximates the values of $Q_{abs}$ and $Q_{sca}$ to be:

$$Q_{abs} \cong 4a\, Im\left(\frac{\varepsilon-1}{\varepsilon+2}\right) \qquad (1.7)$$

$$Q_{sca} \cong \frac{8}{3} a \left|\frac{\varepsilon-1}{\varepsilon+2}\right|^4 \qquad (1.8)$$

Where a, the size parameter or the particles circumference divided by the wavelength of light, $a = \frac{2\pi r}{\lambda}$, must be less than 1. Plasmonic nanoparticles have the property of ε = -2 resulting in a lot of scattering and absorption. Plasmonic materials take advantage of efficiently converting light into energy which can be used to improve public health with biomedical imaging, drug delivery, photothermal therapies, biosensors and as a photocatalysts, the application of focus in this dissertation.[17]

### 1.5: Dissertation Direction

In this work I first focus on the synthesis of and then potential application of alternative plasmonic nanoparticles made of ZrN. Although ZrN is an ionic compound, when it is nanostructured with a novel non-thermal plasma process it is able to leverage high electron mobility on the surface of the particle creating a plasmonic or LSPR response that is also present in metal nanoparticles.

Gold and silver are typically the choice nanoparticles due to their initial discovery and plasmonic response in the visible spectrum. However, these nanoparticles are extremely expensive and melt at temperatures around 700 °C, motivating interest to find alternative plasmonic materials such as metal nitrides.[18] Particularly, titanium nitride (TiN) and

zirconium nitride (ZrN) display the properties to replace gold and silver, since they are inexpensive earth abundant materials and have higher melting points. ZrN however displays a sharper and blue shifted plasmonic response compared with that of TiN.[19]

There are two problems that optimization of plasmonic ZrN hopes to address. First, transitioning energy generation away from fossil fuels as quickly as possible will require efficient use of the over 40% of the sun's energy in the visible part of the spectrum by converting visible light into chemical energy. There is increased pressure on public health systems due to climate disasters caused by fossil fuel energy production.[20] Improvement in public health could come from more green energy production.

The second issue that ZrN is applied is as late as 2016, dangerous levels of Chromium (VI) were found in over 90% of water systems sampled in the US.[21] Back in 1993, hexavalent Chromium was determined to be the cause of an illness in California.[22]

Chapter 2 focuses on ZrN and its photocatalytic abilities compared with a semi-conductor $TiO_2$ for the treatment of water without the addition of an alcohol catalyst. ZrN nanoparticles are invoked to reduce chromium (VI) to a less dangerous form chromium (III) with light. By both taking advantage of the high surface area of nanoparticles and their ability to absorb both ultraviolet light and visible light, the nanoparticles are able to facilitate the reduction of chromium (VI) to chromium (III) in solution.

In chapter 3, plasmonic ZrN is invoked again to reduce heavy metals using methanol as a catalyst in water first with platinum then with chromium (VI). The addition of methanol increases the rate of reaction and shows the potential for ZrN in photocatalytic applications. ZrN is compared in this chapter first with TiN to reduce platinum 4+ to the neutral form,

which other researchers achieved including our group.[23,24] The ZrN is compared with $TiO_2$ in the reduction of chromium (VI) in a solution of water and methanol.

In the second half of this dissertation, I developed a nanostructured yttria-stabilized zirconia (YSZ) "Window to the Brain" which aimed to have a material that was both optically transparent and structurally sound such that it would protect the brain if used to replace a part of the skull. Brain health conditions are on the rise and account for more than 15% of all health losses: even more than cardiovascular diseases and cancer.[25] Furthermore, COVID is increasing the number of people developing long term brain consequences. These chronic diseases could need to be repeatedly imaged or in need of optical treatment that a YSZ window to the brain has the potential to provide.[26]

YSZ is often applied in dentistry for crowns due to its white and opaque color and like a coffee cup, that is very hard but if it breaks it will break into a million pieces.[27] The addition of 3% by mol of $Y_2O_3$ to $ZrO_2$ (3YSZ) stabilizes the crystal structure in tetrahedral and the material becomes tougher thanks to the transformation toughening.[28] Add 8% by mol of $Y_2O_3$ (8YSZ) and the crystal structure changes to cubic resulting in the material becoming more brittle, a problem for a cranial implant.

As 3YSZ has the desired mechanical properties for a cranial implant, 8YSZ has the optical properties due to its cubic isotropic structure. A major source of scattering in nanostructured materials is there is a difference in the index of refraction going different directions produced from different crystal structures.[29] Additionally, when starting with nanoparticles densified into a bulk solid, it is possible to keep the grains smaller than the wavelength of light, then the light is not scattered off the boundaries.[30]

Other sources of opaqueness discussed in this dissertation is the reduction of oxygen vacancies and pores in the material from the densification process. These oxygen vacancies and defects are spaces that can absorb light within the material and need to be annealed in air to oxidize the material and make it more transparent.[31] Pores have a different index of fraction as the YSZ and so change the path of the light. Apetz et al. were able to develop a theory of pore scattering using the same Mie theory as before for plasmonic nanoparticles modeling with good accuracy the transparency of $Al_2O_3$ ceramic microstructures applying Mie theory to spherical pores.[32]

In chapter 4, I demonstrate controllable synthesis of YSZ nanoparticles with an aerosol spray pyrolysis technique that allows for the control of the crystal structure of the particles from 3YSZ to 8YSZ and size of those particles. The synthesized nanoparticles are then densified using a Spark Plasma Sintering method into a dense, puck-like bulk material which is then tested for its mechanical and optical properties of YSZ. By nanostructuring the yttria stabilized zirconia, small particles are sintered together, much like a high-tech Mesopotamian clay brick, to optimized both the mechanical and optical properties.

In chapter 5 commercial YSZ nanoparticles densified with the current-activated pressure-assisted (CAPAD) method is comped with in-house synthesized particles densified with SPS. Once again, the optical properties are assessed in relation to the grain sizes of the nanostructured material. In addition to investigation the optimization of the mechanical and optical properties, the cytocompatibility of densified YSZ structure is investigated to determine the potential for YSZ window to the brain.

## 1.6: References


(1) Tobin, E.; Brenner, S. Nanotechnology Fundamentals Applied to Clinical Infectious Diseases and Public Health. *Open Forum Infect. Dis.* **2021**, *8* (12), 1–10. https://doi.org/10.1093/ofid/ofab583.

(2) Pautler, M.; Brenner, S. Nanomedicine: Promises and Challenges for the Future of Public Health. *Int. J. Nanomedicine* **2010**, *5* (1), 803–809. https://doi.org/10.2147/IJN.S13816.

(3) Roduner, E. Size Matters: Why Nanomaterials Are Different. *Chem. Soc. Rev.* **2006**, *35* (7), 583–592. https://doi.org/10.1039/b502142c.

(4) Harris, L. K.; Theriot, J. A. Surface Area to Volume Ratio: A Natural Variable for Bacterial Morphogenesis. *Trends Microbiol.* **2018**, *26* (10), 815–832. https://doi.org/10.1016/j.tim.2018.04.008.

(5) Anjum, S.; Ishaque, S.; Fatima, H.; Farooq, W.; Hano, C.; Abbasi, B. H.; Anjum, I. Emerging Applications of Nanotechnology in Healthcare Systems: Grand Challenges and Perspectives. *Pharmaceuticals* **2021**, *14* (8), 1–26. https://doi.org/10.3390/ph14080707.

(6) Freestone, I.; Meeks, N.; Sax, M.; Higgitt, C. The Lycurgus Cup - A Roman Nanotechnology. *Gold Bull.* **2008**, *40* (4), 270–277. https://doi.org/10.1007/BF03215599.

(7) Reibold, M.; Pätzke, N.; Levin, A. A.; Kochmann, W.; Shakhverdova, I. P.; Paufler, P.; Meyer, D. C. Structure of Several Historic Blades at Nanoscale. *Cryst. Res. Technol.* **2009**, *44* (10), 1139–1146. https://doi.org/10.1002/crat.200900445.

(8) Pérez-Arantegui, J.; Molera, J.; Larrea, A.; Pradell, T.; Vendrell-Saz, M.; Borgia, I.; Brunetti, B. G.; Cariati, F.; Fermo, P.; Mellini, M.; Sgamellotti, A.; Viti, C. Luster Pottery from the Thirteenth Century to the Sixteenth Century: A Nanostructured Thin Metallic Film. *J. Am. Ceram. Soc.* **2001**, *84* (2), 442–446. https://doi.org/10.1111/j.1151-2916.2001.tb00674.x.

(9) Feynman, R. P. There's Plenty of Room at the Bottom; 1960.

(10) Handy, R. D.; Shaw, B. J. Toxic Effects of Nanoparticles and Nanomaterials: Implications for Public Health, Risk Assessment and the Public Perception of Nanotechnology. *Heal. Risk Soc.* **2007**, *9* (2), 125–144. https://doi.org/10.1080/13698570701306807.

(11) Matsuda, M.; Hunt, G. Nanotechnology and Public Health. *Japanese J. Public Heal.* **2005**, *923* (11), 923–927.

(12) Hutchison, J. E. Greener Nanoscience: A Proactive Approach to Advancing Applications and Reducing Implications of Nanotechnology. *ACS Nano* **2008**, *2* (3), 395–402. https://doi.org/10.1021/nn800131j.

(13) Kim, H. C.; Fthenakis, V. Life Cycle Energy and Climate Change Implications of Nanotechnologies: A Critical Review. *J. Ind. Ecol.* **2013**, *17* (4), 528–541. https://doi.org/10.1111/j.1530-9290.2012.00538.x.

(14) Bohren, C. F. How Can a Particle Absorb More than the Light Incident on It? *Am. J. Phys.* **1983**, *51* (4), 323–327. https://doi.org/10.1119/1.13262.

(15) Boltasseva, A.; Atwater, H. A. Low-Loss Plasmonic Metamaterials. *AAAS* **2011**, *331* (January), 290–292.

(16) Link, S.; El-Sayed, M. A. *Shape and Size Dependence of Radiative, Non-Radiative and Photothermal Properties of Gold Nanocrystals*; 2000; Vol. 19. https://doi.org/10.1080/01442350050034180.

(17) Liao, H.; Nehl, C. L.; Hafner, J. H. Biomedical Applications of Plasmon Resonant Metal Nanoparticles. *Nanomedicine* **2006**, *1* (2), 201–208. https://doi.org/10.2217/17435889.1.2.201.

(18) Guler, U.; Shalaev, V. M.; Boltasseva, A. Nanoparticle Plasmonics : Going Practical with Transition Metal Nitrides. *Biochem. Pharmacol.* **2015**, *18* (4), 227–237. https://doi.org/10.1016/j.mattod.2014.10.039.

(19) Exarhos, S.; Alvarez Barragan, A.; Aytan, E.; Balandin, A. A.; Mangolini, L. Plasmonic Core-Shell Zirconium Nitride – Silicon Oxynitride Nanoparticles. *ACS Energy Lett.* **2018**, No. September, acsenergylett.8b01478. https://doi.org/10.1021/acsenergylett.8b01478.

(20) Burkle, F. M. Challenges of Global Public Health Emergencies: Development of a Health-Crisis Management Framework. *Tohoku J. Exp. Med.* **2019**, *249* (1), 33–41. https://doi.org/10.1620/tjem.249.33.

(21) Scutti, S. Should I worry about chromium-6 in my drinking water? https://www.cnn.com/2016/09/21/health/chromium-6-drinking-water-questions/index.html.

(22) Banks, S. *The "Erin Brockovich Effect": How Media Shapes Toxics Policy*; 2002.

(23) Barragan, A. A.; Hanukovich, S.; Bozhilov, K.; Yamijala, S. S. R. K. C.; Wong, B. M.; Christopher, P.; Mangolini, L. Photochemistry of Plasmonic Titanium Nitride Nanocrystals. *J. Phys. Chem. C* **2019**, *123* (35), 21796–21804. https://doi.org/10.1021/acs.jpcc.9b06257.

(24) Naldoni, A.; Guler, U.; Wang, Z.; Marelli, M.; Malara, F.; Meng, X.; Besteiro, L. V.; Govorov, A. O.; Kildishev, A. V.; Boltasseva, A.; Shalaev, V. M. Broadband Hot-Electron Collection for Solar Water Splitting with Plasmonic Titanium Nitride. *Adv. Opt. Mater.* **2017**, *5* (15), 1–11. https://doi.org/10.1002/adom.201601031.

(25) Political Studio. Global data is key to tackling the rise in brain health conditions

https://www.politico.eu/sponsored-content/global-data-is-key-to-tackling-the-rise-in-brain-health-conditions/.

(26) Halaney, D. L.; Jonak, C. R.; Liu, J.; Davoodzadeh, N.; Cano-Velázquez, M. S.; Ehtiyatkar, P.; Park, H.; Binder, D. K.; Aguilar, G. Chronic Brain Imaging Across a Transparent Nanocrystalline Yttria-Stabilized-Zirconia Cranial Implant. *Front. Bioeng. Biotechnol.* **2020**, *8* (June), 1–13. https://doi.org/10.3389/fbioe.2020.00659.

(27) Denry, I.; Kelly, J. R. State of the Art of Zirconia for Dental Applications. **2007**, *4*, 299–307. https://doi.org/10.1016/j.dental.2007.05.007.

(28) Garvie, R. C.; Hannink, R. H.; Pascoe, R. T. Ceramic Steel? *Nature* **1975**, *258* (5537), 703–704. https://doi.org/10.1038/258703a0.

(29) Kodera, Y.; Hardin, C. L.; Garay, J. E. Transmitting, Emitting and Controlling Light: Processing of Transparent Ceramics Using Current-Activated Pressure-Assisted Densification. *Scr. Mater.* **2013**, *69* (2), 149–154. https://doi.org/10.1016/j.scriptamat.2013.02.013.

(30) Klimke, J.; Trunec, M.; Krell, A. Transparent Tetragonal Yttria-Stabilized Zirconia Ceramics: Influence of Scattering Caused by Birefringence. *J. Am. Ceram. Soc.* **2011**, *94* (6), 1850–1858. https://doi.org/10.1111/j.1551-2916.2010.04322.x.

(31) Alaniz, J. E.; Perez-Gutierrez, F. G.; Aguilar, G.; Garay, J. E. Optical Properties of Transparent Nanocrystalline Yttria Stabilized Zirconia. *Opt. Mater. (Amst).* **2009**, *32* (1), 62–68. https://doi.org/10.1016/j.optmat.2009.06.004.

(32) Apetz, R.; Van Bruggen, M. P. B. Transparent Alumina: A Light-Scattering Model. *J. Am. Ceram. Soc.* **2003**, *86* (3), 480–486. https://doi.org/10.1111/j.1151-2916.2003.tb03325.x.

# Chapter 2: Plasmonic Zirconium Nitride Nanoparticles for Light-driven Cr (VI) Reduction

## 2.1: Introduction

Chromate and dichromate ions are common toxins found in agricultural soil[1], in groundwater[2] and even drinking water.[3,4] Furthermore, these toxins are present and left over from industrial processes such as metallurgy, metal plating, wood processing, leather tanning, and metal corrosion inhibition.[5] The World Health Organization recommends limiting the amount of Cr (VI) to below 0.05 mg/L in drinking and surface water.[6] Cr (VI) is extremely carcinogenic[7] due to its high mobility with the ability to penetrate cell walls[3,8] and toxic, targeting the kidneys, liver, nerves and other soft tissues.[5,9,10] However, Cr (III) is needed to metabolize sugars and fats[11] and it appears to be a nutrient to some plants.[12] These considerations motivate the search for effective ways to reduce Cr (VI) to Cr (III).

The most effective and widely used techniques for removal and reduction of hexavalent chromium species are membrane filtration,[13] and coagulation,[14] while other methods have been effective as well such as absorption with activated carbons,[15] biosorbants[16] and ion exchange,[17] among others.[18,19] Semiconductor nanoparticles have also been used to photo-reduce Cr (VI) to Cr (III)[20–23]. $TiO_2$ has received the most attention due to its photoactivity and low costs,[22–24] followed by ZnO due to its similar band gap.[25] However, due to the wide band gaps of $TiO_2$ and ZnO (3.2[26] and 3.3[27] eV respectively), these semiconductors utilize only UV light, wasting the visible part of the solar spectrum.

In recent years, there has been growing interest towards the use of plasmonic particles to drive photochemical reactions, motivated by their inherently large extinction cross sections which in principle allow harnessing the solar radiation in an efficient manner.[28–32] Their properties have led to their investigation for many applications, including for photocatalysts,[33,34] photovoltaic devices,[28,34,35] photochemistry, [36–38] surface enhanced Raman spectroscopy (SERS),[39] sensing[40] and biophotonics.[41] Gold and silver show plasmonic resonance in the visible part of the spectrum.[42] Unfortunately gold and silver are expensive, motivating the search for alternative plasmonic materials such as oxides and nitrides.[43,44] Metal nitrides exhibit plasmonic properties in the visible and near infrared (NIR) spectrum as well as high bulk melting temperatures.[45,46] Several groups have investigated the properties of titanium nitride (TiN) nanoparticles, including our own.[47] Zirconium nitride, on the other hand, has received less attention despite having a stronger plasmonic response in the visible range compared to TiN.[30] This is partially due to the fact that ZrN in nanoparticle form is not readily available, although recent reports on the synthesis of nitride nanoparticles via non-thermal plasmas offer a promising approach to their preparation.[47,48]

The relaxation of plasmonic oscillations can lead to the formation of a non-thermal electron energy distribution, often referred as “hot” electrons which can drive chemical reactions and improve the efficiency of semiconductors.[31,49–52] Direct charge transfer can also occur from plasmonic nanoparticles, increasing the rates of reaction.[53] However, recent papers have interpreted the chemical activity of plasmonic nanostructures in terms of photothermal effects, i.e. localized heating induced by the large absorption cross sections

of these materials.[54,55] It is well accepted that it is difficult to distinguish between the photothermal and the electronic contributions to the reactivity of plasmonic nanostructures.[56]

In this work, we discuss for the first time the use of ZrN nanoparticles as a photocatalyst to reduce Cr (VI) to Cr (III), demonstrating its chemical activity under visible irradiation and confirming its potential for sustainable water treatment. ZrN plasmonic nanoparticles are produced in house using a non-thermal plasma synthesis technique.[48] We compare the Cr (VI) reduction kinetics from plasmonic ZrN to that obtained from commonly available $TiO_2$ nanoparticles, and show that ZrN reduces Cr (VI) more efficiently. We observe a 90% reduction in Cr (VI) concentration after 10 hours of illumination at 120 W/cm$^2$. We stress that the measurements reported here are obtained using a broadband non-coherent light source, all while actively cooling the nanoparticle dispersion to keep it near to room temperature. Spectrally resolved measurements conclusively confirm that Cr (VI) photoreduction occurs when visible light is coupled to the ZrN nanoparticles. In addition, control reduction experiments performed in the dark indicate that temperatures as high as 70°C are needed to achieve a reduction rate that is comparable to that observed under illumination. This study not only demonstrates the potential of alternative plasmonic materials for water treatment, but it also provides conclusive evidence of a reduction process is mediated by photo-generated charge carriers, rather than by a photothermal effect due to careful X-ray Photoelectron Spectroscopy (XPS) material characterizations.

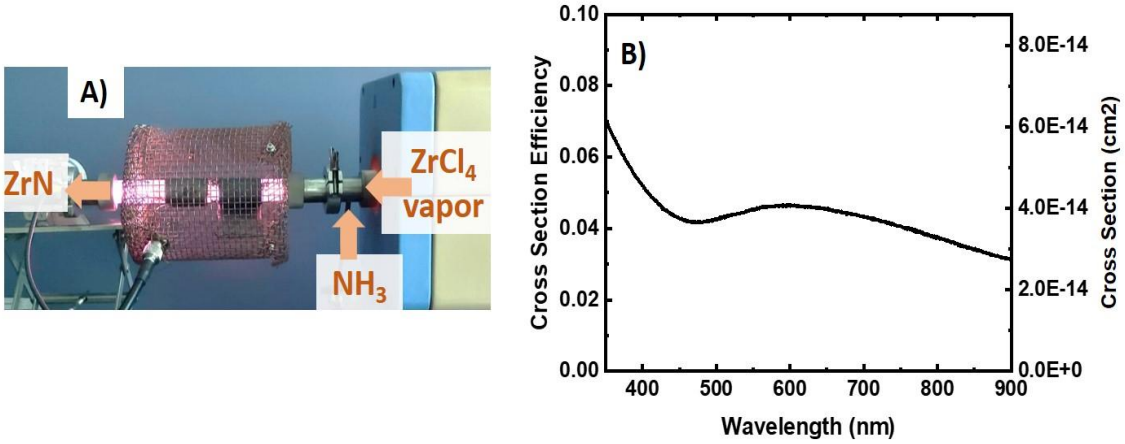


*Figure 2.1. A) Photograph of the plasma reactor making ZrN nanoparticles. The furnace contains ZrCl4 which is sublimated and flows downstream to the left where the particles are collected on a stainless-steel mesh filter. B) The cross-section efficiency for ZrN determined through the absorbance of a solution containing .005 g/L of ZrN nanoparticles. On the Secondary Axis (right axis) the absorbance cross section of the material is shown.*

## 2.2: Experimental Methods

### *2.2.1: Synthesis of ZrN nanoparticles*

Non-thermal plasma synthesis provides an innovative way to produce ultra-high purity nitride nanoparticles that are difficult to fabricate using other methods.[57–59] The non-thermal plasma synthesis of ZrN nanoparticles is described in detail in a previous contribution from our group.[48] In summary and with a picture in figure 1, ~1000 mg of a $ZrCl_4$ solid precursor (from Alfa Aesar) is placed in a crucible inside of a tube furnace, evacuated and heated to 185$^o$ C. 90 sccm of argon carries the sublimated $ZrCl_4$ downstream into a plasma reactor, where ammonia is injected into the reactor through an inlet after the furnace and before the plasma as shown in figure 1. The pressure is kept at 5 torr, while a non-thermal plasma is sustained by supplying 180 W at 13.56 MHz. The ZrN nanoparticles are collected in a stainless-steel mesh filter downstream of the plasma volume. After

synthesis, the particles are annealed in argon for one hour at 250$^{o}$ C to remove any ammonium chloride biproducts. An image of the reactor and the cross-section efficiency of the ZrN nanoparticles are shown in Figure 1.

The absorbance cross section was determined using the Beer Lambert Law using a solution of .005 g/L of ZrN to minimize the contributions to scattering. The quartz cuvette was 1 cm in path length and the absorption was measured using a double beam scanning UV/Vis/NIR spectrophotometer (Varian Carry 500).

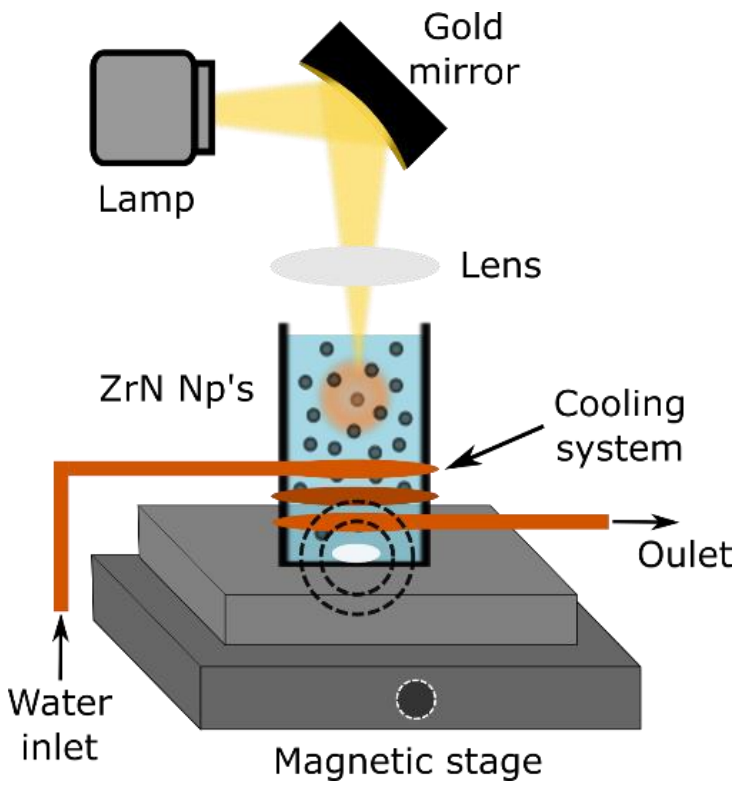


*Figure 2.2. Setup of photocatalytic experiments. A 500 W Hg−Xe Newport 67005 arc lamp was reflected off a gold mirror down to a solution consisting of nanoparticles, chromium, and methanol. A water-cooling system was used to standardize the effects of heating. A magnetic stir bar insured that the full solution would get illuminated.*

We compare the reactivity of our ZrN nanoparticles against that of $TiO_2$ nanoparticles. This choice is motivated by the fact that $TiO_2$ is a ubiquitous photo-active material, therefore providing a good benchmark. Commercially available $TiO_2$ nanoparticles (Sigma Aldrich part number 718467) are used for in our study. For completeness, we have also tested the Cr (VI) reduction rate for a dispersion of commercially available gold nanoparticles (from nanoComposix, JCP1043-MGM2238). These particles show a plasmon resonance in the visible spectrum, therefore providing a good comparison against our ZrN alternative plasmonic nanomaterials.

*2.2.2: Photocatalytic reduction of Cr (VI)*

Figure 2 displays the setup for the photocatalytic experiments. A solution of water, particles, and Cr (VI) is placed in 20 ml glass vials, while stirring with a magnetic bar throughout the duration of the experiment to assure uniform mixing. A glass slide is attached at the top of the vial to prevent evaporation and at the same time, allow the light to pass into the solution. The initial Cr (VI) concentration is 0.55 mM for all the experiments discussed here. The vial is placed in a cooling system consisting of a large beaker with 100 ml of water and a copper coil with flowing water around the solution. This prevents the temperature of the sample from reaching values above 30 $^{o}$ C for the entire duration of the experiment. The samples are illuminated with a 500 W Hg−Xe arc lamplight source (Newport 67005), using a 90-degree gold mirror and focusing the light into the solution with a lens (focal distance f = 20 cm), as is shown in Figure 2.

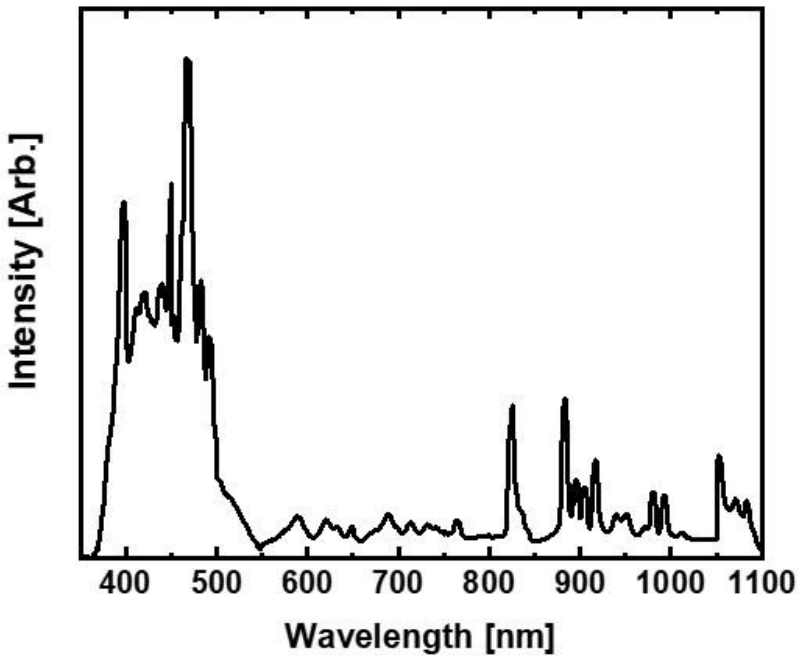


*Figure 2.3. The optical spectrum of the incident light for the photocatalytic reaction s acquired with monochromator connected to a power meter from 500 W (3 W/cm$^2$) Hg-Xe Newport 67005 Arc Lamp.*

The visible spectrum from the Hg-Xe arc lamp is measured with a Czerny-Turner Monochromator (Horiba Scientific) connected to an optical power meter, as is shown in figure 3. The same monochromator is used to perform the photo-reduction measurements at selected wavelengths from 375 nm to 900 nm, to compare the response between $TiO_2$ and ZrN. We quantify the quantum yield (Eqn. 5 below) of the reduction reaction by means of a calibrated photodiode (DET 10A(/M) Thorlabs), with a responsivity range from 200 to 1000 nm. The radiation induced voltage of the photodiode measured with an oscilloscope (Tektronix TDS 2024C) and armed with the knowledge of the photon energy at the specifically selected wavelength, we are able to calculate the photon flux into the

reaction solution. The quantum yield (Eqn. 4) is then defined as the number of reduced Cr (VI) molecules, calculated with the diphenyl carbazide method described below, per absorbed photon such that the amount of reduction at selected wavelengths are comparable.

The power density of the Hg-Xe arc lamp was varied using stainless steel mesh to cast a shadow on the reactor vial lowering the total power. We then measured the power using the same calibrated photodiode with neutral density filters to prevent photodiode saturation and calculated the total power from the induced voltage in the photodiode measured with the same oscilloscope taking into account the light blocked by the neutral density filters.

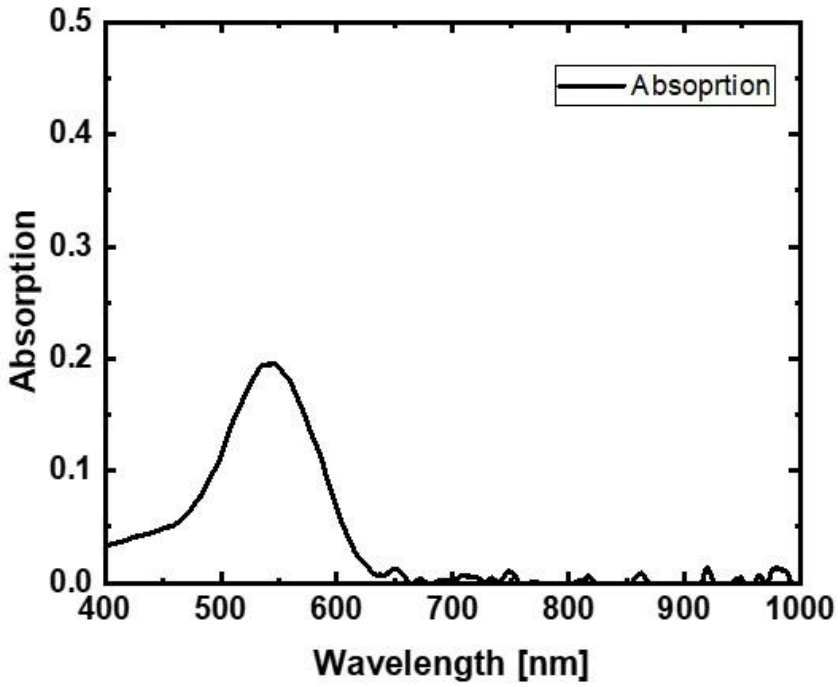


*Figure 2.4. Sample absorbance spectrum using the diphenyl carbazide method with .5mMol of Cr (VI). The absorption at 540 nm is linearly related to the amount of Cr (VI) in the solution.*

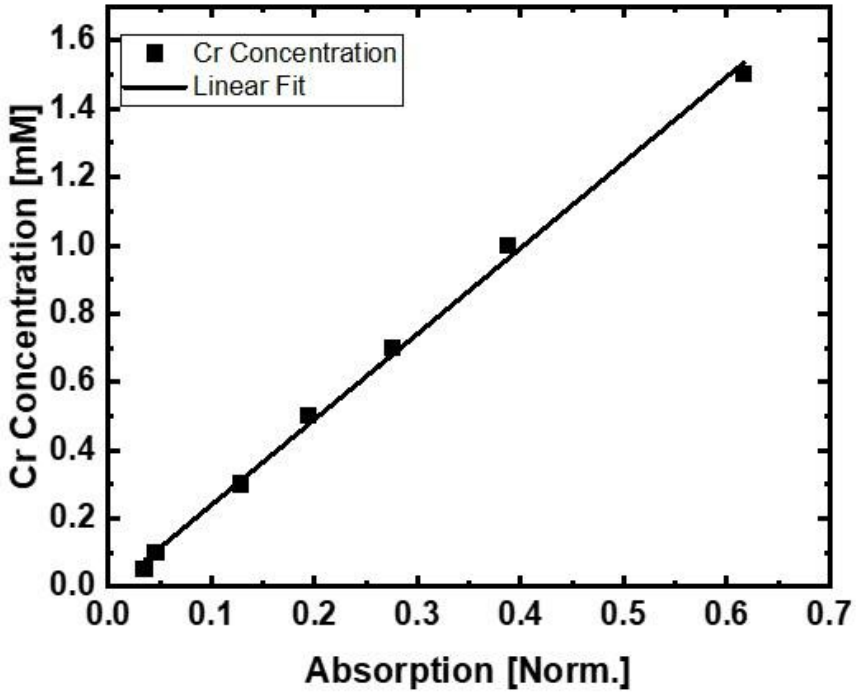


*Figure 2.5. Calibration curve for the amount of Cr (VI) using the diphenyl carbazide method. The 1,5-Diphenylcarbazide bonds to the Cr (VI) which absorbs light at 540 nm. The amount of absorption at 540 nm is linearly proportional to the amount of Cr (VI) in solution.*

### *2.2.3: Cr (VI) diphenyl carbazide method*

Stock Cr (VI) solutions are prepared by dissolving 141.4 mg $K_2Cr_2O_7$ (Sigma-Aldrich) into 100 ml of deionized water creating a solution of 9.6 mM Cr (VI) ions. The amount of Cr (VI) in each sample was measured at the beginning and end of the experiments, using the diphenyl carbazide method.[60] In this method, a dye along with an acid, sulfuric acid in our case, is added to a small amount of solution. The dye forms a complex with the Cr (VI)

ions and provides a signature absorption at 540 nm. The dye is a mixture of 250 g of 1,5-Diphenylcarbazide dissolved in 50 ml of Acetone, both purchased from Sigma-Aldrich.

For each photocatalytic experiment, 2 aliquots of 50 µl each are removed from the illuminated samples. The first aliquot is diluted to 5 ml by adding 4.6 ml of deionized water, 0.250 ml of 0.5 M sulfuric acid, and then 0.1 ml of the dye solution. The second aliquot is diluted in exactly the same way as the first one, except the dye solution is substituted by 0.1 ml of acetone. The Cr (VI) concentration is determined by measuring the absorbance of the diluted first aliquot, using the diluted second aliquot as reference spectrum.

The absorption spectrum of a solution with 0.5 mMol of Cr (VI) is provided in Figure 4. Measuring the transmittance using a broad light source (SLS201L Thorlabs) and a visible light spectrometer (Ocean Optics USB 2000) we can calculate the absorbance of the dye solution using equation 1:

$$A = -log_{10}\frac{T}{T_0} \qquad (2.1)$$

Where the control with acetone is called $T_0$, and then the solution with the dye is T. The dye solution, 250 g of 1,5-Diphenylcarbazide dissolved in 50 ml of Acetone, bonds with the Cr (VI) ions to show a strong absorption at around 540 nm. This peak absorbance can be used to determine the amount of Cr (VI) in solution after creating a calibration curve shown below.

The diphenyl carbazide method relies on the complexing between 1,5-Diphenylcarbazide and Cr (VI), which turns the solution pink-like color and provides a clear absorption peak at 540 nm. The absorbance at 540 nm is linearly proportional to the amount of Cr (VI), as shown in figure 5.

Using Stock Cr (VI) solutions prepared by dissolving 141.4 mg $K_2Cr_2O_7$ (Sigma-Aldrich) into 100 ml of deionized water creating a solution of 9.6 mM Cr (VI) ions we created a number of solutions with concentrations between 0 and 1.6 mMol of Cr (VI). Then we measured the absorption of the solutions at 540 nm and plotted that along with the known Cr (VI) concentration to create a linear calibration curve that could be used to determine the amount of Cr (VI) in our experiments.

*2.2.4: X-ray Photoelectron Spectroscopy (XPS) Measurements*

We performed XPS measurements to monitor any changes to the particle chemical composition that may occur during the photoreduction experiments using a Kratos Analytical Axis Ultra Delay-Line Detector Imaging XPS. Samples were processed for 5 hours without illumination nor heat ("Control" sample), under illumination ("Light" sample), and while heating to 70°C without illumination ("Heat" sample). The samples were then rinsed with DI water and dried in vacuum for 48 hours before performing XPS measurements to determine whether the chemical composition of the ZrN particles changed during the Cr (VI) reduction.

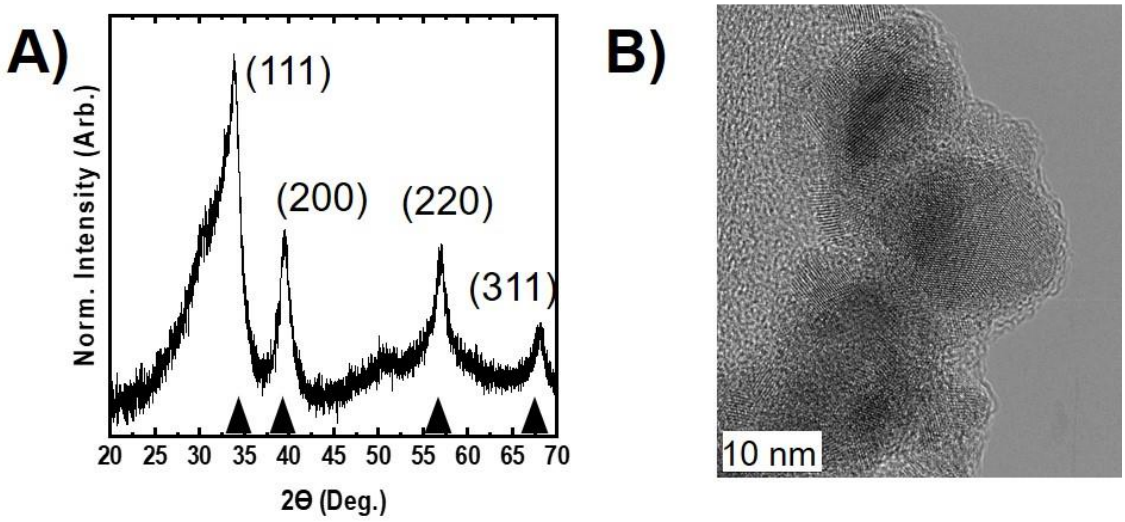


*Figure 2.6. A) XRD analysis of ZrN nanoparticles confirming a cubic structure and particle size of roughly 10 nm. B) TEM image of ZrN nanoparticles, where a particle size of ~10 nm and spherical a is confirmed.*

## 2.3: Results and Discussion

### *2.3.1: Material Characterization*

Figure 6 displays the material characterization of non-thermal plasma synthetized ZrN, used in this photochemical study. The XRD pattern in Figure 6A, confirm the cubic structure of ZrN with the 111, 200, 220 and 311 peaks at 34°, 39°, 56° and 67° degrees respectively.[61] The small shoulder on the 111 peak at 30 degrees and the peak at 50 degrees, indicate the formation of an oxide shell around the particles when they are exposed to air, consistent with our previous findings.[48] We estimate a particle size of ~10 nm using Scherrer analysis of the XRD plot, and can be further observed in the TEM micrograph of Figure 6B.

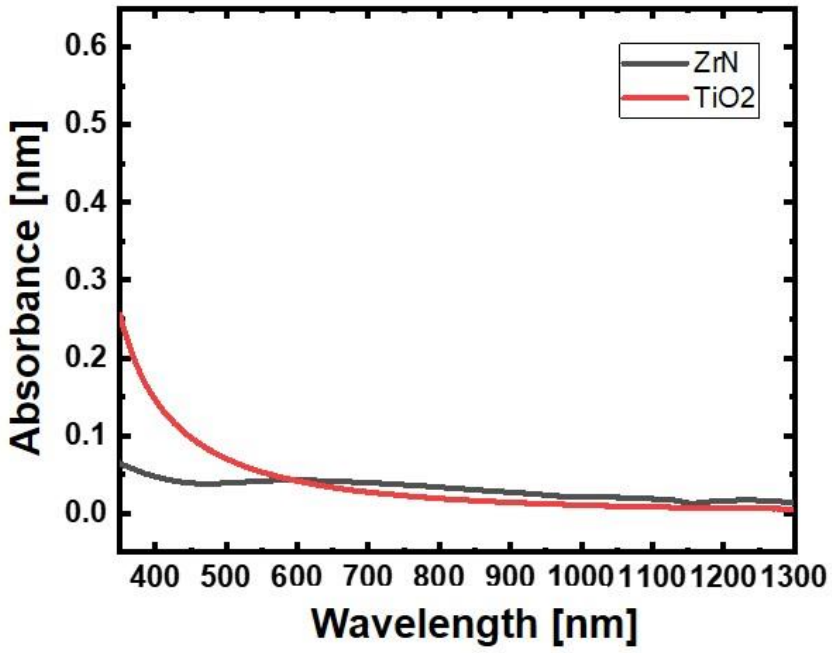


*Figure 2.7. The absorbance of ZrN (Black) and TiO2 (Red) at a concentration of .005 g/L measured with a US-Vis-NIR Cary 5000 spectrometer.*

The absorbance cross section shown in figure1 was obtained by measuring the absorbance of .005 g/L ZrN nanoparticles in a solution of water, contained in a 1 cm length quartz cuvette, using a double beam scanning UV/Vis/NIR spectrophotometer (Varian Carry 500). The absorption efficiency of the synthesized ZrN nanoparticles, defined as the ratio between the light absorption cross section and the physical cross section for a spherical 10 nm particles ($7.85 \times 10^{-13}$ $cm^2$), are determined via Beer Lambert Law. The solution was diluted to .005 g/L to be optically clear, minimizing the contribution of scattering to measure the cross section and the absorption is shown in figure 7.

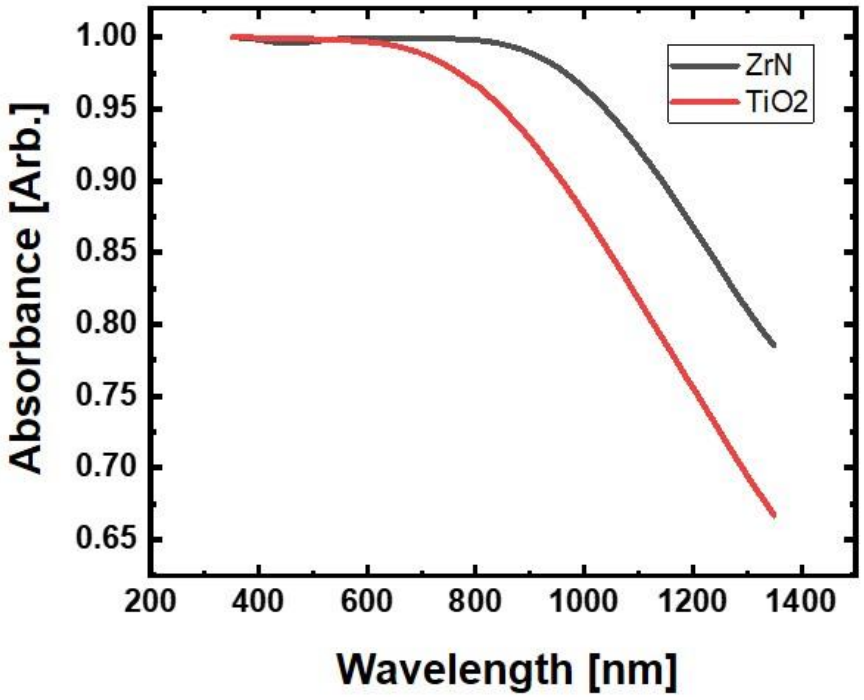


*Figure 2.8. Absorbance of 1 g/L of $TiO_2$ (Red) and ZrN (Black).*

The absorbance cross section was calculated to be on the order of $10^{-14}$ $cm^2$ which agrees well with previously reported values for a 10 nm ZrN nanoparticle.[62] The broad peak in the visible part of the spectrum at 600 nm is induced by the material's plasmonic response, as carefully verified and discussed in our previous contribution.[48] As a comparison, the absorption cross section for a ~21 nm $TiO_2$ particle is about $1.00 \times 10^{-11}$ $cm^2$ in the UV region of the spectrum, with negligible absorbance in the visible because of the wide band gap of the material and peak absorption around 387 nm.[63,64] Furthermore, gold has its peak absorption at 540 nm and is known to have a large absorption cross section in the visible part of the region on the order of $10^{-10}$ $cm^2$.[65]

*2.3.2: Photocatalytic reduction experiments of Cr (VI)*

The Cr (VI) reduction kinetics between ZrN, $TiO_2$ and Au plasmonic nanomaterials is compared to determine both how ZrN is measured against a standard semiconductor photocatalysis ($TiO_2$) as well as a plasmonic photocatalyst (Au). The three nanomaterials are all spherical with sizes of 10 nm, 21 nm and 50 nm for ZrN, $TiO_2$ and Au respectively.

For these measurements, the nanoparticle concentration is 1 g/L for all samples, the light intensity is 120 $W/cm^2$ and the initial Cr (VI) concentration is 0.55 mM. The reduction rate without any particles is also measured as control. At this concentration, the solution is optically thick, meaning all of the light delivered to the samples is absorbed and utilized to drive the photochemical reduction process as shown in figure 8. The variation in Cr (VI) concentration when mixed with ZrN, $TiO_2$ or Au particles, under illumination, is shown in Figure 9a. In summary, 6 aliquots are removed, to calculate the Cr (VI) concentration 3 times (2 aliquots are needed to determine the absorption) and estimate an error, as described above for different light exposure times. The final Cr (VI) concentrations are normalized over the initial Cr (VI) concentration.

A clear decrease in Cr (VI) concentration is observed when in the presence of illuminated $TiO_2$ or ZrN nanoparticles. We find that the rate of reduction is faster for the ZrN solution. After 3 hours, more than 30% of the Cr (VI) ions have been reduced for the case of ZrN compared to roughly 20% for the case of $TiO_2$. Furthermore, after 10 hours, 90%, of the Cr (VI) was reduced with ZrN compared with only 50% of the Cr (VI) with $TiO_2$. Similar results have been reported by Valari et al., where they use the same amount of titania

powders and methanol in the solution to speed the reaction, enabling reduction over 30% of Cr (VI) within two hours.[22] As was mentioned previously, in our experiments we did not include methanol in the solution for any of the photocatalytic experiments, since its toxicity represents a great disadvantage in real-life water treatment processes. In addition, it should be noted that our measurements are performed at a pH of 5, which is expected to lead to a slower reduction rate than the pH of 2.5 used by Valari et al.

In a previous study, Ku et al. 2001 found that the rate of photoreduction can be represented with a pseudo-first-order Langmuir-Hinshelwood kinetics expression:[66]

$$ln\left[\frac{Cr(VI)_0}{Cr(VI)}\right] = k_{red}t \qquad (2.2)$$

Where $k_{red}$ is the photocatalytic reduction rate constant and t is the illumination time in minutes. When applying this expression to our measurements, we find the rate constant to be 0.0032 $min^{-1}$ for ZrN and 0.0013 $min^{-1}$ for $TiO_2$. Ku et al. observed a slightly higher rate constant for $TiO_2$ (.057 $min^{-1}$) for conditions similar to ours but should be noted the pH value was 3.[66]

Overall, these results confirm that both $TiO_2$ and ZrN can drive the photoreduction of Cr (VI) ions to Cr (III). The photoreduction is expected to proceed via the formation of charge carriers in the active material, followed by their reaction with surface-bound Cr (VI) ions. The reduction of Cr (VI) to Cr (III) requires three electrons per Cr (VI) ion:[22]

$$Cr_2O_7^{2-} + 14H^+ + 6e^- \rightarrow 2Cr^{3+} + 7H_2O \qquad (2.3)$$

For the oxidation half-reaction, water is oxidized to balance.[20]

$$2H_2O + 4h^+ \rightarrow O_2 + 4H^+ \qquad (2.4)$$

We should point out that there is a no measurable reduction of Cr (VI) in the control sample nor in the sample of Au nanoparticles. While ZrN and $TiO_2$ were bare particles, we suspect that the inability of Au particles to reduce any Cr (VI) was due to a polymer surfactant in addition to being unstable under the intensity of light, however this is outside the scope of this paper.[67] As we show below (Figure 14), ZrN does not show any signs of degradation or oxidation when irradiated on for the duration of experiments.

Additionally, we performed the same photocatalytic reduction experiment with $TiO_2$ and ZrN to with 500 mg/L of particles in solution to determine the effect of particle load on Cr (VI) reduction shown in Figure 11. The reduction rate was very similar when using 1 g/L of particles, values of .0038 $min^{-1}$ and .0015 $min^{-1}$ were measured for ZrN and $TiO_2$ respectively showing the solution is still optically thick and using the same number of photons to drive the reaction.

We test our hypothesis that the superior reduction rate of ZrN nanoparticles, compared to $TiO_2$ is due to its capability to absorb the visible part of the spectrum. We have performed Cr (VI) reduction experiments with ZrN and $TiO_2$, at a concentration of 500 mg/L using a monochromator to spectrally resolve the radiation from our broadband light source. The solutions are illuminated for 1 hour at selected wavelengths in the visible part of the spectrum to determine why ZrN is performing better than $TiO_2$.

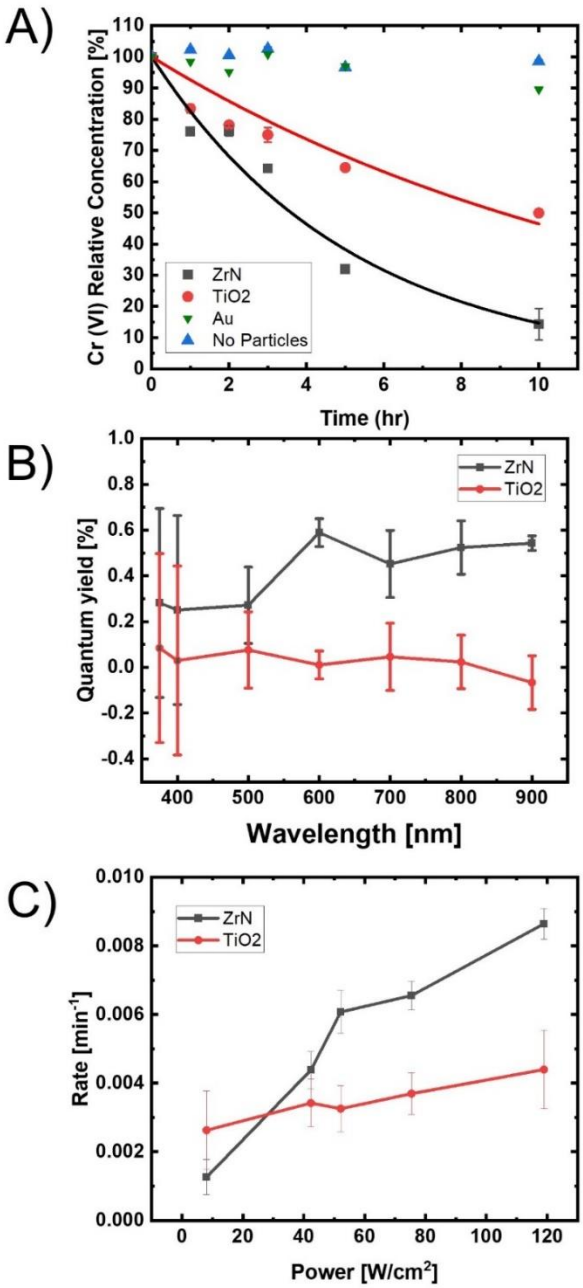


*Figure 2.9. A) Cr (VI) Reduction study illuminated with 119 W/cm$^2$ shows how the Cr (VI) reduction compares with 1 g/L of ZrN (Black Squares), 1 g/L of $TiO_2$ (Red Circles) and No Particles (Blue Triangles). B) Action Plot showing the Quantum Yield for ZrN (Black Squares) and $TiO_2$ (Red Circles) with spectrally selected radiation using a monochromator. Each sample was illuminated for 1 hour at each wavelength with 500 mg/L of nanoparticles in solution. C) The power study shows how the reduction of Cr (VI) increases with increased power density during the first 15 min of illumination with 500 mg/L of particles. ZrN (Black Squares)*

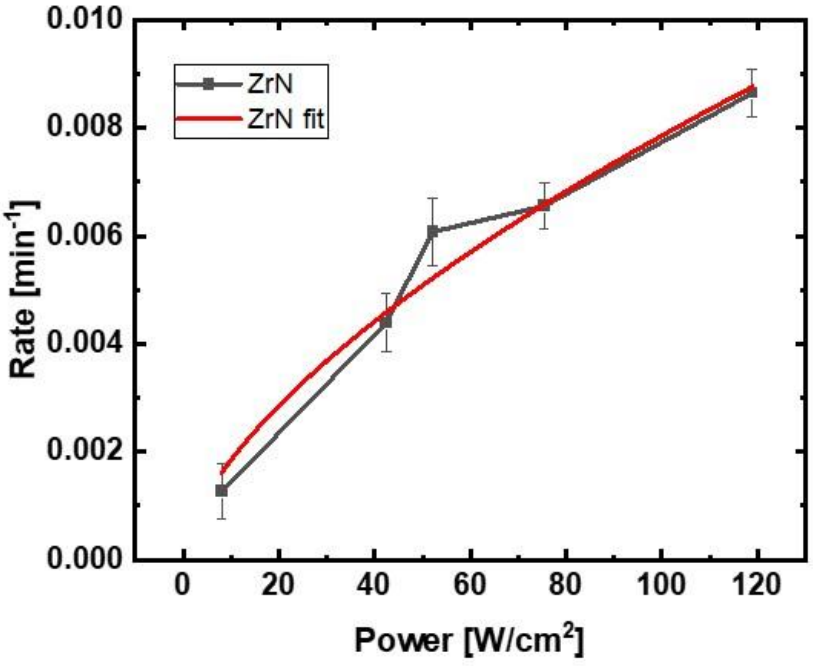


*Figure 2.10. The fit of Cr (VI) reduction as a function nof illumination power with ZrN is fit to the function* $y = Ax^b$ *where* $A = .0004\left[\frac{1}{min}\left(\frac{cm^2}{W}\right)^{.6}\right]$ *and* $b = .6$.

In figure 9b, we plot the quantum yield of the reduction process at selected excitation wavelengths in the visible part of the spectrum. By calculating the quantum yield, we provide a measure of the internal efficiency with which the material utilizes incoming photons of different energies. The quantum yield (QY) is calculated using the measured photon flux as described above and the equation from Li et al:[29]

$$Quantum\ yield = \frac{\#\ ions\ reduced}{\#\ absorbed\ photons} \qquad (2.5)$$

Figure 9b shows the QY as a function of excitation wavelength for ZrN and $TiO_2$. As expected, illumination of $TiO_2$ below its bandgap results in no detectable reduction of Cr

(VI). On the other hand, we observe a reasonably high internal QY for the case of ZrN, peaking at ~.6% at 600 nm where the peak absorption is for ZrN. Most importantly, the QY for ZrN is measurable using visible light confirming that the photoreduction process is initiated by visible radiation which couples into the material via its inherent plasmonic response. Both ZrN and $TiO_2$ increase their QY in the UV part of the spectrum as compared with 400 nm which is expected as the radiation has higher energy.

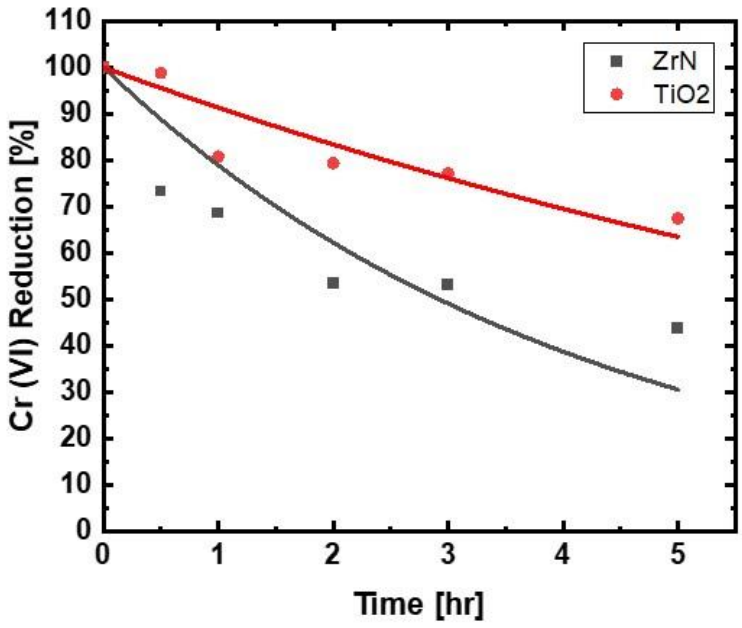


*Figure 2.11. Cr (VI) Reduction study illuminated with 119 W/cm2 shows of the Cr (VI) reduction compares with 500 mg/L of ZrN (Black squares) and TiO2 (Red circles).*

To further investigate the origin of the photoreduction mechanism for these two materials, we have measured the kinetics of photoreduction as a function of input photon flux. The results are shown in Figure 9C, in which we plot the initial reduction rate of Cr (VI)

observed in 15 min of illumination, as a function of optical power density. For these measurements, the particle concentration is 500 mg/L ZrN. As is evident in Figure 9c, the reduction rate for ZrN increased with the power density. The kinetic photoreduction rate constant calculated from Equation 1 increased from .0013 to .0086 $min^{-1}$ for ZrN as the power increased from roughly 8 $W/cm^2$ to 120 $W/cm^2$, more than an order of magnitude while the photoreduction rate constant is independent of temperature for $TiO_2$.

We therefore observe a sublinear dependence of photocatalytic rate on intensity with ZrN (rate $\propto$ $intensity^n$, with $n < 1$), where in our case n = .6 as shown in figure 10. As the photon flux increases, the rise in material excitation competes with an increased rate of recombination of the photo-generated carriers, limiting the gain in photoreduction rate and leading to a sublinear dependence. By fitting the data with a power law rather than a linear fit, we are able to compare our results with a thermally driven chemical reaction that would follow an Arrhenius or exponential distribution as others have shown to be with plasmonic photocatalysts. In this way, A is the temperature independent constant for the chemical reaction that depends on the particular reactants (size, shape, density, energy transfer rates, etc.) and collision theory.

For comparison, we find that the n = .2 for $TiO_2$ but statistically the rate is independent of light at high intensity. This was previously confirmed in the literature by Sakthivel et al. that the reaction rate as a function of light intensity with $TiO_2$ starts off with a linear dependence at low intensity, transitioning to a square root dependence and finally a rate independent of light intensity at higher intensities.[68] In the range of light intensities we are

using (10-120 W/cm$^2$), we expect that the rate would be independent of light intensity for $TiO_2$.

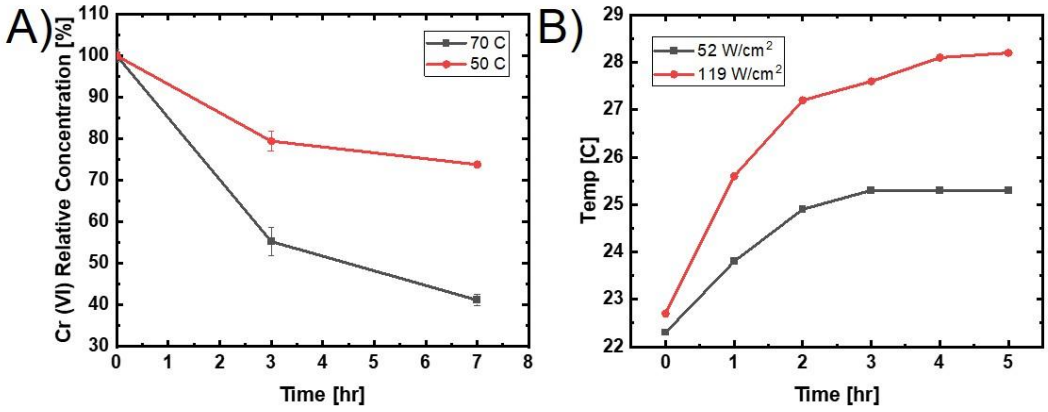


*Figure 2.12. A) Reduction of Cr (VI) in a solution with 500 mg/L of ZrN particles in the dark and placed in a water bath at 70 C (Black squares) and 50 C (Red Circles) B) Increase in temperature measured with a thermocouple in a solution of particles in water illuminated with 119 W/cm2 (Black squares) and 52 W/cm2 (Red circles)*

Nevertheless, linear, or weakly sublinear trend as a function of light intensity with ZrN is consistent with an electronic excitation mechanism, in which the reduction is promoted by charge carriers as opposed to a thermally driven (photothermal) process. An exponential dependence would be expected for the case in which the incoming photons are simply converted to thermal energy, with the increase in particle temperature then driving the reaction.[55] We clearly do not observe this in our experiments. In addition, as was mentioned in the experiment section, a cooling coil is used to keep the bulk temperature constant in the solution reaching a maximum value of 28°C for all the measurements (displayed in figure 12b).

The results presented so far show that ZrN has the capability of reducing Cr (VI) ions under illumination with visible light. Next, we investigate whether this behavior can be attributed to a photothermal effect by determining the temperature that would reduce Cr (VI) at a similar rate.

In this study, we placed a solution of 500 mg/L of ZrN particles into a vial wrapped in aluminum foil to block any light from catalyzing the reaction. Then, we placed the covered vial into a water bath, and the temperature was measured with a thermocouple reaching 50°C and 70°C stabilized on a hot plate. The data shows a rate of reduction to be .002 $min^{-1}$ when the water bath was placed at 70°C, as shown in figure 12A, about 33% less than the rate when illuminated with 119 $W/cm^2$.

However, placing the same solution into a water bath at 50°C, still 20°C more than we measured with a thermocouple during photocatalytic reduction experiments, we observe that 30% of the Cr (VI) was reduced in 7 hours. At much higher temperatures, over 100°C, Cr (VI) has been known to reduce to Cr (III) with heat and leach onto other materials as well.[69,70] To account for any reduction of Cr(VI) due to heating, we performed the same experiment without particles but did not see any reduction. Isolating the effects of temperature, these results indicate that the particles must reach a temperature of 70 ℃ to get similar amount of reduction as with a light intensity of 119 $W/cm^2$.

To determine the role of temperature played in the reduction of Cr (VI), we measured the temperature of the solution with a K-type thermocouple during illumination. Figure 12b compares the increase in temperature due to a moderate illumination intensity of 50 $W/cm^2$

with the highest value 120 W/cm$^2$. As shown, the temperature remains up to 28°C due during the entire experiment, due the water bath and cooling coil set it up for the reaction process.

As stated earlier, the mechanism with which plasmonic nanoparticles photocatalyzed reaction is still debated among the community. Dubi et al. use a theory of illumination induced heating to replot data from important papers in the field showing that different reactions could be explained with photothermal effects for example: $H_2$ disassociation with Au nanoparticles imbedded in $TiO_2$ and $SiO_2$, $O_2$ dissociation in ethylene epoxidation, and $H_2$ production.[55] In addition to the group mentioned above, Baffou et al. also describe experimental procedures and common mistakes in trying to disentangle the photothermal and photoelectric effects.[56,71]

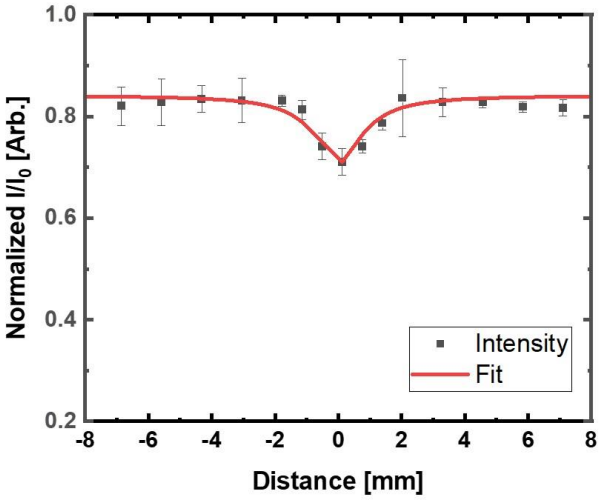


| Material | Non-Linear Coefficient [mm/W] |
|---|---|
| Au | $3.5 \times 10^{-7}$ |
| TiN | $2.2 \times 10^{-6}$ |
| ZrN | $7.5 \times 10^{-7}$ |

*Figure 2.13. Z-scan measurement and table of nonlinear Coefficients for ZrN compared with Au and TiO2 from Z-scan shown. Measurements were taken with a laser at 1,064 nm (A12-10-1,064-CTAB-DIH-Bulk) laser. The table displays the non-linear coefficient [mm/W].*

We performed Z-scan measurements to quantify potential non-linear effects in the optical response of ZrN that would result in particle heating. Nonlinear absorption of plasmonic materials explain the small amount of particle heating and higher water temperature.[72]

The nonlinear absorption properties of nanoparticles are investigated using the Z-scan method using a 1064 nm 6 ns Nd:YAG (Surelite, Amplitude, Germany) pulsed laser and compared with previous work from our group.[73] As a cuvette containing particles in water solution is moved across a Z-micrometer stage in the longitudinal direction of the laser. The cuvette starts out of the laser focal point but is moved into the focal point at distance 0. The transmission of light through the cuvette is measured as a function of the cuvette position in relation to the focal point. The beam intensity is measured simultaneously by two identical photodiodes attached to an integrating sphere connected to an oscilloscope taking samples at 2.5 GHz.

The normalized transmittance is used to calculate the Absorption coefficient $\alpha(I)$:[74]

$$\frac{I}{I_0} = \sum_{m=0}^{\infty} \frac{\left(\frac{\alpha L_{eff} I_0}{1+\frac{i^2}{{i_0}^2}}\right)^m}{m+1} \qquad (2.6)$$

Where $L_{eff} = \frac{(1-e^{-\alpha_0 L})}{\alpha_0}$ is the effective length, L is the length of the sample, $I_0$ is the peak intensity at the focal point, z is the longitudinal displacement, $Z_0$ is the Rayleigh range and $\alpha_0$ is the linear absorption coefficient of the solution. The values shown in the table above were calculated using this question.

The nonlinear coefficient was the same order of magnitude to that of gold but one order of magnitude lower than TiN and shown in the Table in figure 13.[73] The measured non-linear absorption coefficient is smaller than previously reported values or TiN, although we should note that it may be higher when probed with a laser excitation that overlaps with the plasmonic response of the material. Nevertheless, non-linear effects are not expected to play a role in the photoreduction process at the photon fluxes utilized here.

Furthermore, we used a modified equation 7 from Un et al.[75] where we use the interfacial heat transfer coefficient between water and a nanoparticle and the surface area of that particle:

$$T_{NP} = T_W + \frac{C_{abs} I_{inc}}{4\pi k_w A} \qquad (2.7)$$

Where $T_{NP}$ is the nanoparticles temperature, $T_W$ is the ambient temperature of the water, $C_{abs}$ is the absorption cross-section, $K_w$ is the interfacial heat transfer coefficient between water and a nanoparticle ($100 \frac{MW}{m^2 \cdot K}$)[76] and A is the surface area of the particle to calculate potential increase in particle temperature at the intensities used in the photocatalytic experiments. We determine that the temperature of the particle to be .000003 Kelvin above the temperature of the water, essentially at thermal equilibrium. This result is expected due to the continuous wave illumination and fast heat transfer to the surroundings supporting the argument and providing additional evidence that the particles are not heating to a temperature, 70℃ that would be needed to drive the chemistry at a similar rate as illumination. Both measuring and calculating the particles to be at thermal equilibrium with the water rules out any major contributions from temperature to the reduction of Cr (VI).

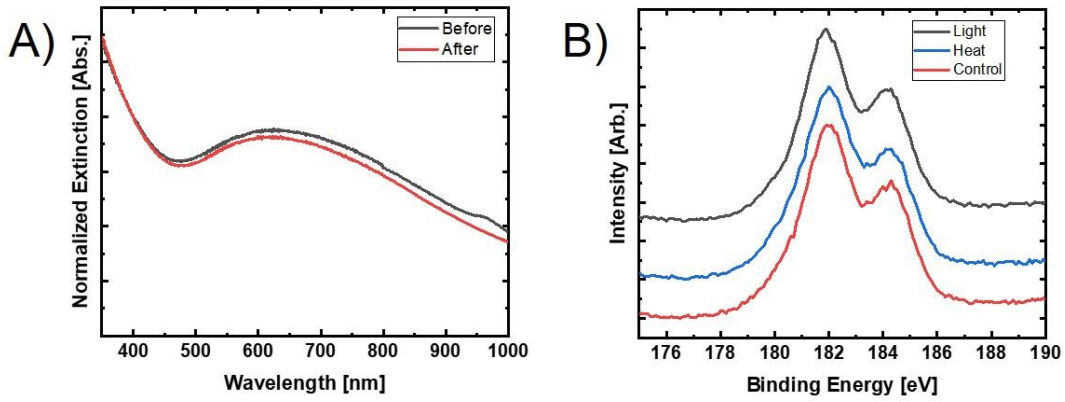


*Figure 2.14. A) The Normalized Extinction of ZrN nanoparticles before and after getting illuminated with 50 W/cm$^2$ in water for 5 hours. B) XPS data showing the 3d binding energy for ZrN in a solution with Cr (VI) when exposed to light (black), Heat with in a 50 ℃ water bath (blue) 5 hours and ZrN particles in*

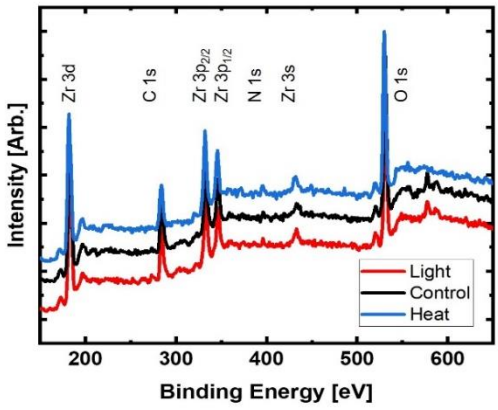


| Surface Atomic Composition (at. %) | | | | | |
|---|---|---|---|---|---|
| | Cr | O | N | Zr | Total |
| Light | 4 | 67 | 6 | 22 | 100 |
| Control | 5 | 67 | 5 | 24 | 100 |
| Heat | 5 | 67 | 5 | 23 | 100 |

*Figure 2.15. Full XPS Spectrum for ZrN as a function of binding energy when in solution with Cr (VI) and exposed to light (Black), Dark (Red) and Dark + Heat placed in a 50 °C water bath (Blue). Table of Surface atomic composition percentages for ZrN after exposed to light for 5 hours in solution with Cr (VI) exposed to Light, Dark and Dark + Heat in 50°C water bath.*

To determine whether ZrN was getting oxidized or degrading due to the illumination, we measured the extinction spectra before and after irradiating the particles in solution with an intensity of 50 W/cm$^2$ during 5 hours. As shown above in figure 14a, the extinction

spectra did not change. If it were the case that the particles were oxidizing, we would expect the extinction peak to broaden and red shift as literature suggests would happen when plasmonic particles oxidize.[48] Similar results were obtained at higher power, 120 W/cm$^2$ with virtually no change in the extinction spectra.

Full X-ray photoelectron spectroscopy (XPS) spectrum is shown in figure 15 in addition to table showing the atomic percentage of Zr, O, N and Cr which show that ZrN was unchanged during the photocatalytic experiments. The large amount of oxygen content, roughly 66% for all samples, comes from the XPS focus on surface contents and consistent with the oxygen shell of our ZrN nanoparticles.

Furthermore, XPS was performed on ZrN particle to further determine whether or not ZrN was participating in the reaction to reduce Cr (VI). Figure 14b displays the peaks from ZrN featuring the 3d 3/2 and 5/2 respectively at 182 eV and 185 eV consistent with previous literature.[77] As you can see, there is virtually no difference on the surface of ZrN particles whether they are exposed to light or heat. The same experiments were performed with and without Cr (VI) but showed no change. This shows a remarkable stability for ZrN during photocatalysis and the potential to efficiently use light.[78]

Those two peaks at 182 and 185 are convoluted between ZrO and ZrN 3d 3/2 and 5/2 bonds. In figure 15, fittings of the 3d 5/2 and 3/2 binding energies for the Zr-O and Zr-N respectively performed after subtracting the baseline using the Tougaard's method. The surface oxidation is displayed with the higher intensity of the Zr-O fittings. The Zr-N binding energies are at 180.3 and 182.7 for the 3d 5/2 and 3/2 respectively with a standard

distance of 2.4 eV apart similarly with the Zr-O peaks at 182 and 184.4 eV.[77] There was no difference in the samples between Control, Light and Heat and the XPS spectra is consistent with our previous report on ZrN.[48]

The important analysis is that the particles do not show any change in surface composition regardless of the catalytic conditions supporting the conclusion that the photocatalytic reduction of Cr (VI) with ZrN is using an electronic mechanism and not oxidizing to participate in the reaction.

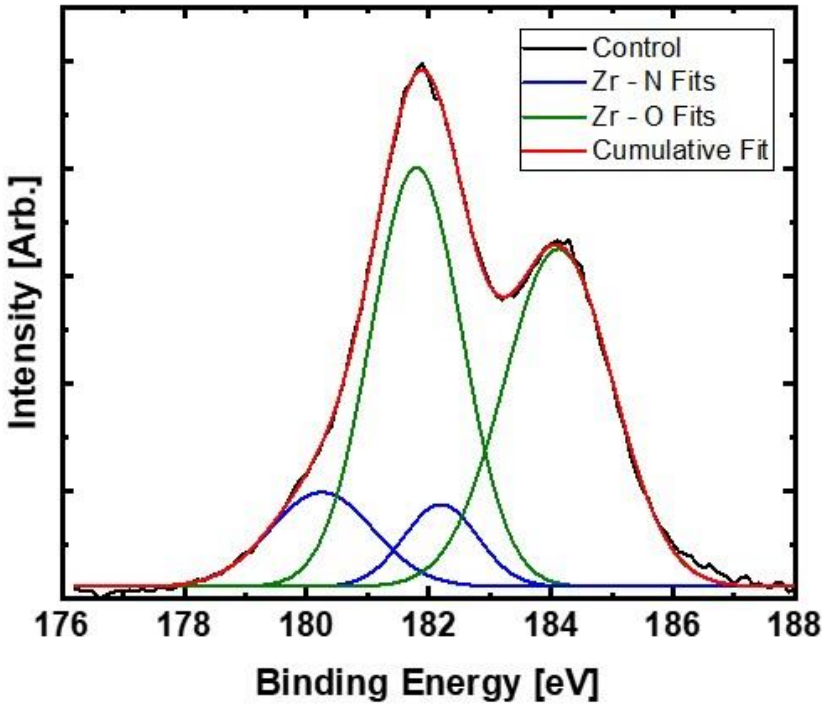


*Figure 2.16. XPS data of ZrN particle control (black) showing the 3d binding energies with the Zr-N (blue) and Zr-O (green) for the 3d 5/2 and 3/2 bonds. The cumulative fit shown in red.*

## 2.4: Conclusions

We have demonstrated that plasmonic ZrN nanoparticles can effectively reduce Cr (VI) ions by utilizing visible light. Compared to $TiO_2$ nanoparticles, ZrN achieved faster reduction kinetics and a reasonable internal quantum yield even in the visible part of the spectrum. ZrN is abundant and low-cost, especially when compared to other plasmonic materials such as gold and silver. ZrN nanoparticles of high quality can be produced using a low-temperature plasma approach, i.e., an easy-to-use system. We have also found a sub-linear dependence on the reduction kinetics with the illumination power, which is not consistent with a photo-thermal effect but rather with the photo-generation of charge carriers. Additionally, material characterization before and after reactions shows that ZrN is not participating in the reaction but just introducing charge carriers.

To further rule out any major photothermal contributions to the chemistry, we determined that the particles must reach a temperature of 70℃ to have a similar reduction rate as with illumination. This is consistent with literature that under continuous wave illumination, nanoparticles will quickly reach thermal equilibrium with the surrounding solution. Overall, these results provide additional convincing evidence of the great potential of alternative plasmonic materials for applications in photochemistry. In particular, their abundance and ability to use the solar spectrum make them an attractive platform for water treatment applications.

## 2.5: References


(1) Antibachi, D.; Kelepertzis, E.; Kelepertsis, A. Heavy Metals in Agricultural Soils of the Mouriki-Thiva Area (Central Greece) and Environmental Impact Implications. *Soil Sediment Contam.* **2012**, *21* (4), 434–450. https://doi.org/10.1080/15320383.2012.672493.

(2) Blowes, D. Tracking Hexavalent Cr in Groundwater. *Science (80-. ).* **2002**, *295* (5562), 2024–2025. https://doi.org/10.1126/science.1070031.

(3) Gil, R. A.; Cerutti, S.; Gásquez, J. A.; Olsina, R. A.; Martinez, L. D. Preconcentration and Speciation of Chromium in Drinking Water Samples by Coupling of On-Line Sorption on Activated Carbon to ETAAS Determination. *Talanta* **2006**, *68* (4), 1065–1070. https://doi.org/10.1016/j.talanta.2005.06.069.

(4) National Toxicology Program. NTP Technical Report on the Toxicology and Carcinogenesis Studies of Sodium Dichromate Dihydrate. **2008**, *1* (125), 200.

(5) Kotaś, J.; Stasicka, Z. Chromium Occurrence in the Environment and Methods of Its Speciation. *Environ. Pollut.* **2000**, *107* (3), 263–283. https://doi.org/10.1016/S0269-7491(99)00168-2.

(6) World Health Organization. *Environ. Heal. Criteria 61* **1988**.

(7) Gibb, H. J.; Lees, P. S. J.; Pinsky, P. F.; Rooney, B. C. Lung Cancer among Workers in Chromium Chemical Production. *Am. J. Ind. Med.* **2000**, *38* (2), 115–126. https://doi.org/10.1002/1097-0274(200008)38:2<115::AID-AJIM1>3.0.CO;2-Y.

(8) Barnowski, C.; Jakubowski, N.; Stuewer, D.; Broekaert, J. A. C. Speciation of Chromium by Direct Coupling of Ion Exchange Chromatography with Inductively Coupled Plasma Mass Spectrometry. *J. Anal. At. Spectrom.* **1997**, *12* (10), 1155–1161. https://doi.org/10.1039/a702120h.

(9) Lee, K. P.; Ulrich, C. E.; Geil, R. G.; Trochimowicz, H. J. Inhalation Toxicity of Chromium Dioxide Dust to Rats after Two Years Exposure. *Sci. Total Environ.* **1989**, *86* (1–2), 83–108. https://doi.org/10.1016/0048-9697(89)90197-6.

(10) Gad, S. C. Acute and Chronic Systematic Chromium Toxcity. **1989**, *86*, 149–157.

(11) Anderson, R. A. Essentiality of Chromium in Humans. *Sci. Total Environ.* **1989**, *86* (1–2), 75–81. https://doi.org/10.1016/0048-9697(89)90196-4.

(12) Kimbrough, D. E.; Cohen, Y.; Winer, A. M.; Creelman, L.; Mabuni, C. A Critical Assessment of Chromium in the Environment. *Crit. Rev. Environ. Sci. Technol.* **1999**, *29* (1), 1–46. https://doi.org/10.1080/10643389991259164.

(13) Muthukrishnan, M.; Guha, B. K. Effect of PH on Rejection of Hexavalent Chromium by Nanofiltration. *Desalination* **2008**, *219* (1–3), 171–178. https://doi.org/10.1016/j.desal.2007.04.054.

(14) Lee, G.; Hering, J. G. Removal of Chromium(VI) from Drinking Water by Redox-Assisted Coagulation with Iron(II). *J. Water Supply Res. Technol. - AQUA* **2003**, *52* (5), 319–332. https://doi.org/10.2166/aqua.2003.0030.

(15) Mohan, D.; Pittman, C. U. Activated Carbons and Low Cost Adsorbents for Remediation of Tri- and Hexavalent Chromium from Water. *J. Hazard. Mater.* **2006**, *137* (2), 762–811. https://doi.org/10.1016/j.jhazmat.2006.06.060.

(16) Dakiky, M.; Khamis, M.; Manassra, A.; Mer'eb, M. Selective Adsorption of Chromium(VI) in Industrial Wastewater Using Low-Cost Abundantly Available Adsorbents. *Adv. Environ. Res.* **2002**, *6* (4), 533–540. https://doi.org/10.1016/S1093-0191(01)00079-X.

(17) Lin, S. H.; Kiang, C. D. Chromic Acid Recovery from Waste Acid Solution by an Ion Exchange Process: Equilibrium and Column Ion Exchange Modeling. *Chem. Eng. J.* **2003**, *92* (1–3), 193–199. https://doi.org/10.1016/S1385-8947(02)00140-7.

(18) Sharma, S. K.; Petrusevski, B.; Amy, G. Chromium Removal from Water: A Review. *J. Water Supply Res. Technol. - AQUA* **2008**, *57* (8), 541–553. https://doi.org/10.2166/aqua.2008.080.

(19) Owlad, M.; Aroua, M. K.; Daud, W. A. W.; Baroutian, S. Removal of Hexavalent Chromium-Contaminated Water and Wastewater: A Review. *Water. Air. Soil Pollut.* **2009**, *200* (1–4), 59–77. https://doi.org/10.1007/s11270-008-9893-7.

(20) Chen, D.; Ray, A. K. Removal of Toxic Metal Ions from Wastewater by Semiconductor Photocatalysis. *Chem. Eng. Sci.* **2001**, *56* (4), 1561–1570. https://doi.org/10.1016/S0009-2509(00)00383-3.

(21) Trillas, M.; Barber, R.; Munoz, J.; Peral, J.; Domenech, X. Photoreduction of Cr(VI) over CdS Supported on a Glass Matrix. *Hazard. Waste Hazard. Mater.* **1991**, *8* (2), 151–159. https://doi.org/10.1089/hwm.1991.8.151.

(22) Valari, M.; Antoniadis, A.; Mantzavinos, D.; Poulios, I. Photocatalytic Reduction of Cr(VI) over Titania Suspensions. *Catal. Today* **2015**, *252*, 190–194. https://doi.org/10.1016/j.cattod.2014.10.014.

(23) Yao, Z.; Jia, F.; Jiang, Y.; Li, C. X.; Jiang, Z.; Bai, X. Photocatalytic Reduction of Potassium Chromate by Zn-Doped TiO 2 /Ti Film Catalyst. *Appl. Surf. Sci.* **2010**, *256* (6), 1793–1797. https://doi.org/10.1016/j.apsusc.2009.10.005.

(24) Navío, J. A.; Colón, G.; Trillas, M.; Peral, J.; Domènech, X.; Testa, J. J.; Padrón, J.; Rodŕguez, D.; Litter, M. I. Heterogeneous Photocatalytic Reactions of Nitrite Oxidation and Cr(VI) Reduction on Iron-Doped Titania Prepared by the Wet Impregnation Method. *Appl. Catal. B Environ.* **1998**, *16* (2), 187–196. https://doi.org/10.1016/S0926-3373(97)00073-8.

(25) Chakrabarti, S.; Dutta, B. K. Photocatalytic Degradation of Model Textile Dyes in Wastewater Using ZnO as Semiconductor Catalyst. *J. Hazard. Mater.* **2004**, *112* (3), 269–278. https://doi.org/10.1016/j.jhazmat.2004.05.013.

(26) Munir, S.; Dionysiou, D. D.; Khan, S. B.; Shah, S. M.; Adhikari, B.; Shah, A. Development of Photocatalysts for Selective and Efficient Organic Transformations. *J. Photochem. Photobiol. B Biol.* **2015**, *148*, 209–222. https://doi.org/10.1016/j.jphotobiol.2015.04.020.

(27) Sernelius, B. E.; Berggren, K. F.; Jin, Z. C.; Hamber, I.; Granqvist, C. G. Band-Gap Tailoring of ZnO by Means of Heavy AL Doping. *Phys. Rev. B* **1988**, *37* (17), 244–248.

(28) Brongersma, M. L.; Halas, N. J.; Nordlander, P. Plasmon-Induced Hot Carrier Science and Technology. *Nat. Nanotechnol.* **2015**, *10* (1), 25–34. https://doi.org/10.1038/nnano.2014.311.

(29) Li, K.; Hogan, N. J.; Kale, M. J.; Halas, N. J.; Nordlander, P.; Christopher, P. Balancing Near-Field Enhancement, Absorption, and Scattering for Effective Antenna-Reactor Plasmonic Photocatalysis. *Nano Lett.* **2017**, *17* (6), 3710–3717. https://doi.org/10.1021/acs.nanolett.7b00992.

(30) Magdi, S.; Swillam, M. A. Investigating Several ZrN Plasmonic Nanostructures and Their Effect on the Absorption of Organic Solar Cells. *J. Phys. D. Appl. Phys.* **2017**, *50* (38). https://doi.org/10.1088/1361-6463/aa80d4.

(31) Aizpurua, J.; Baletto, F.; Baumberg, J.; Christopher, P.; Nijs, B. de; Deshpande, P.; Diaz Fernandez, Y.; Fabris, L.; Freakley, S.; Gawinkowski, S.; Govorov, A.; Halas, N.; Hernandez, R.; Jankiewicz, B.; Khurgin, J.; Kuisma, M.; Kumar, P. V.; Lischner, J.; Liu, J.; Marini, A.; Maurer, R. J.; Mueller, N. S.; Parente, M.; Park, J. Y.; Reich, S.; Sivan, Y.; Tagliabue, G.; Torrente-Murciano, L.; Thangamuthu, M.; Xiao, X.; Zayats, A. Theory of Hot Electrons: General Discussion. *Faraday Discuss.* **2019**, 245–281. https://doi.org/10.1039/C9FD90012H.

(32) Zhang, Y.; Nelson, T.; Tretiak, S.; Guo, H.; Schatz, G. C. Plasmonic Hot-Carrier-Mediated Tunable Photochemical Reactions. *ACS Nano* **2018**, *12* (8), 8415–8422. https://doi.org/10.1021/acsnano.8b03830.

(33) Aslam, U.; Rao, V. G.; Chavez, S.; Linic, S. Catalytic Conversion of Solar to

Chemical Energy on Plasmonic Metal Nanostructures. *Nat. Catal.* **2018**, *1*, 656–665.

(34) Linic, S.; Christopher, P.; Ingram, D. B. Plasmonic-Metal Nanostructures for Efficient Conversion of Solar to Chemical Energy. **2011**, *10* (November). https://doi.org/10.1038/NMAT3151.

(35) Atwater, H. A.; Polman, A. Plasmonics for Improved Photovoltaic Devices. *Mater. Sustain. Energy A Collect. Peer-Reviewed Res. Rev. Artic. from Nat. Publ. Gr.* **2010**, *9* (March 2010), 3–11. https://doi.org/10.1142/9789814317665_0001.

(36) Kawamura, G.; Matsuda, A. Synthesis of Plasmonic Photocatalysts for Water Splitting. *Catalysts* **2019**, *9* (12). https://doi.org/10.3390/catal9120982.

(37) Linic, S.; Aslam, U.; Boerigter, C.; Morabito, M. Photochemical Transformations on Plasmonic Metal Nanoparticles. *Nat. Mater.* **2015**, *14* (6), 567–576. https://doi.org/10.1038/nmat4281.

(38) Barragan, A. A.; Hanukovich, S.; Bozhilov, K.; Yamijala, S. S. R. K. C.; Wong, B. M.; Christopher, P.; Mangolini, L. Photochemistry of Plasmonic Titanium Nitride Nanocrystals. *J. Phys. Chem. C* **2019**, *123* (35), 21796–21804. https://doi.org/10.1021/acs.jpcc.9b06257.

(39) Stiles, P. L.; Dieringer, J. A.; Shah, N. C.; Van Duyne, R. P. Surface-Enhanced Raman Spectroscopy. *Annu. Rev. Anal. Chem.* **2008**, *1* (1), 601–626. https://doi.org/10.1146/annurev.anchem.1.031207.112814.

(40) Willets, K. A.; Van Duyne, R. P. Localized Surface Plasmon Resonance Spectroscopy and Sensing. *Annu. Rev. Phys. Chem.* **2007**, *58*, 267–297. https://doi.org/10.1146/annurev.physchem.58.032806.104607.

(41) Li, M.; Guler, U.; Li, Y.; Rea, A.; Tanyi, E. K.; Kim, Y.; Noginov, M. A.; Song, Y.; Boltasseva, A.; Shalaev, V. M.; Kotov, N. A. Plasmonic Biomimetic Nanocomposite with Spontaneous Subwavelength Structuring as Broadband Absorbers. *ACS Energy Lett.* **2018**, *3* (7), 1578–1583. https://doi.org/10.1021/acsenergylett.8b00583.

(42) Boltasseva, A.; Atwater, H. A. Low-Loss Plasmonic Metamaterials. *AAAS* **2011**, *331* (January), 290–292.

(43) Guler, U.; Naik, G. V.; Boltasseva, A.; Shalaev, V. M.; Kildishev, A. V. Performance Analysis of Nitride Alternative Plasmonic Materials for Localized Surface Plasmon Applications. *Appl. Phys. B Lasers Opt.* **2012**, *107* (2), 285–291. https://doi.org/10.1007/s00340-012-4955-3.

(44) Guler, U.; Kildishev, A. V; Shalaev, V. M. Plasmonics on the Slope of Enlightenment : The Role of Transition Metal Nitrides. **2015**, 71–86. https://doi.org/10.1039/c4fd00208c.

(45) Ishii, S.; Sugavaneshwar, R. P.; Nagao, T. Titanium Nitride Nanoparticles as Plasmonic Solar Heat Transducers. *J. Phys. Chem. C* **2016**, *120* (4), 2343–2348. https://doi.org/10.1021/acs.jpcc.5b09604.

(46) Guler, U.; Ndukaife, J. C.; Naik, G. V.; Nnanna, A. G. A.; Kildishev, A. V.; Shalaev, V. M.; Boltasseva, A. Local Heating with Titanium Nitride Nanoparticles. *2013 Conf. Lasers Electro-Optics, CLEO 2013* **2013**. https://doi.org/10.1364/cleo_qels.2013.qtu1a.2.

(47) Alvarez Barragan, A.; Hanukovich, S.; Bozhilov, K. N.; Yamijala, S. S. R. K. C.; Wong, B. M.; Christopher, P.; Mangolini, L. Photochemistry of Plasmonic Titanium Nitride Nanocrystals. *J. Phys. Chem. C* **2019**, acs.jpcc.9b06257. https://doi.org/10.1021/acs.jpcc.9b06257.

(48) Exarhos, S.; Alvarez-Barragan, A.; Aytan, E.; Balandin, A. A.; Mangolini, L. Plasmonic Core-Shell Zirconium Nitride-Silicon Oxynitride Nanoparticles. *ACS Energy Lett.* **2018**, *3* (10), 2349–2356. https://doi.org/10.1021/acsenergylett.8b01478.

(49) Luther, J. M.; Jain, P. K.; Ewers, T.; Alivisatos, A. P. Localized Surface Plasmon Resonances Arising from Free Carriers in Doped Quantum Dots. *Nat. Mater.* **2011**, *10* (5), 361–366. https://doi.org/10.1038/nmat3004.

(50) Mukherjee, S.; Libisch, F.; Large, N.; Neumann, O.; Brown, L. V; Cheng, J.; Lassiter, J. B.; Carter, E. A.; Nordlander, P.; Halas, N. J. Hot Electrons Do the Impossible: Plasmon-Induced Dissociation of H2 on Au. **2013**.

(51) Schlather, A. E.; Manjavacas, A.; Lauchner, A.; Marangoni, V. S.; DeSantis, C. J.; Nordlander, P.; Halas, N. J. Hot Hole Photoelectrochemistry on Au@SiO2@Au Nanoparticles. *J. Phys. Chem. Lett.* **2017**, *8* (9), 2060–2067. https://doi.org/10.1021/acs.jpclett.7b00563.

(52) Zhang, Y.; He, S.; Guo, W.; Hu, Y.; Huang, J.; Mulcahy, J. R.; Wei, W. D. Surface-Plasmon-Driven Hot Electron Photochemistry. *Chem. Rev.* **2018**, *118* (6), 2927–2954. https://doi.org/10.1021/acs.chemrev.7b00430.

(53) Boerigter, C.; Campana, R.; Morabito, M.; Linic, S. Evidence and Implications of Direct Charge Excitation as the Dominant Mechanism in Plasmon-Mediated Photocatalysis. *Nat. Commun.* **2016**, *7*. https://doi.org/10.1038/ncomms10545.

(54) Dubi, Y.; Sivan, Y. “Hot” Electrons in Metallic Nanostructures—Non-Thermal

Carriers or Heating? *Light Sci. Appl.* **2019**, *8* (1). https://doi.org/10.1038/s41377-019-0199-x.

(55) Dubi, Y.; Un, I. W.; Sivan, Y. Thermal Effects - an Alternative Mechanism for Plasmon-Assisted Photocatalysis. *Chem. Sci.* **2020**, *11* (19), 5017–5027. https://doi.org/10.1039/c9sc06480j.

(56) Sivan, Y.; Baraban, J. H.; Dubi, Y. Experimental Practices Required to Isolate Thermal Effects in Plasmonic Photo-Catalysis: Lessons from Recent Experiments. *OSA Contin.* **2020**, *3* (3), 483. https://doi.org/10.1364/osac.376809.

(57) You, K. H.; Kim, J. H.; You, S. J.; Lee, H. C.; Ruh, H.; Seong, D. J. Gallium Nitride Nanoparticle Synthesis Using Nonthermal Plasma with Gallium Vapor. *Curr. Appl. Phys.* **2018**, *18* (12), 1553–1557. https://doi.org/10.1016/j.cap.2018.10.001.

(58) Alvarez Barragan, A.; Ilawe, N. V.; Zhong, L.; Wong, B. M.; Mangolini, L. A Non-Thermal Plasma Route to Plasmonic TiN Nanoparticles. *J. Phys. Chem. C* **2017**, *121* (4), 2316–2322. https://doi.org/10.1021/acs.jpcc.6b08910.

(59) Uner, N. B.; Thimsen, E. Nonequilibrium Plasma Aerotaxy of Size Controlled GaN Nanocrystals. **2019**.

(60) Lace, A.; Ryan, D.; Bowkett, M.; Cleary, J. Chromium Monitoring in Water by Colorimetry Using Optimised 1,5-Diphenylcarbazide Method. *Int. J. Environ. Res. Public Health* **2019**, *16* (10). https://doi.org/10.3390/ijerph16101803.

(61) Rizzo, A.; Signore, M. A.; Mirenghi, L.; Piscopiello, E.; Tapfer, L. Physical Properties Evolution of Sputtered Zirconium Oxynitride Films: Effects of the Growth Temperature. *J. Phys. D. Appl. Phys.* **2009**, *42* (23). https://doi.org/10.1088/0022-3727/42/23/235401.

(62) Monfared, Y. E.; Dasog, M. Computational Investigation of the Plasmonic Properties of TiN, ZrN, and HfN Nanoparticles: The Role of Particle Size, Medium, and Surface Oxidation. *Can. J. Chem.* **2020**, 1–28. https://doi.org/10.1139/cjc-2020-0335.

(63) Du, S.; Li, Z. Enhanced Light Absorption of TiO 2 in the Near-Ultraviolet Band by Au Nanoparticles. *Opt. Soc. Am.* **2010**, *35* (20), 3402–3404.

(64) Zhong, X. L.; Li, Z. Y. Giant Enhancement of Near-Ultraviolet Light Absorption by TiO 2 via a Three-Dimensional Aluminum Plasmonic Nano Funnel-Antenna. *J. Phys. Chem. C* **2012**, *116* (40), 21547–21555. https://doi.org/10.1021/jp306562u.

(65) Xu, J. X.; Siriwardana, K.; Zhou, Y.; Zou, S.; Zhang, D. Quantification of Gold Nanoparticle Ultraviolet-Visible Extinction, Absorption, and Scattering Cross-

Section Spectra and Scattering Depolarization Spectra: The Effects of Nanoparticle Geometry, Solvent Composition, Ligand Functionalization, and Nanopartic. *Anal. Chem.* **2018**, *90* (1), 785–793. https://doi.org/10.1021/acs.analchem.7b03227.

(66) Ku, Y.; Jung, I. L. Photocatalytic Reduction of Cr(VI) in Aqueous Solutions by UV Irradiation with the Presence of Titanium Dioxide. *Water Res.* **2001**, *35* (1), 135–142. https://doi.org/10.1016/S0043-1354(00)00098-1.

(67) Dozzi, M. V.; Prati, L.; Canton, P.; Selli, E. Effects of Gold Nanoparticles Deposition on the Photocatalytic Activity of Titanium Dioxide under Visible Light. *Phys. Chem. Chem. Phys.* **2009**, *11* (33), 7171–7180. https://doi.org/10.1039/b907317e.

(68) Sakthivel, S.; Neppolian, B.; Shankar, M. V.; Arabindoo, B.; Palanichamy, M.; Murugesan, V. Solar Photocatalytic Degradation of Azo Dye: Comparison of Photocatalytic Efficiency of ZnO and TiO2. *Sol. Energy Mater. Sol. Cells* **2003**, *77* (1), 65–82. https://doi.org/10.1016/S0927-0248(02)00255-6.

(69) Mao, L.; Gao, B.; Deng, N.; Zhai, J.; Zhao, Y.; Li, Q.; Cui, H. The Role of Temperature on Cr(VI) Formation and Reduction during Heating of Chromium-Containing Sludge in the Presence of CaO. *Chemosphere*. 2015, pp 197–204. https://doi.org/10.1016/j.chemosphere.2015.05.097.

(70) Wei, Y. L.; Chiu, S. Y.; Tsai, H. N.; Yang, Y. W.; Lee, J. F. Thermal Stabilization of Chromium(VI) in Kaolin. *Environ. Sci. Technol.* **2002**, *36* (21), 4633–4641. https://doi.org/10.1021/es0114761.

(71) Baffou, G.; Bordacchini, I.; Baldi, A.; Quidant, R. Simple Experimental Procedures to Distinguish Photothermal from Hot-Carrier Processes in Plasmonics. *Light Sci. Appl.* **2020**, *9* (1). https://doi.org/10.1038/s41377-020-00345-0.

(72) Alvarez, C.; Berrospe-Rodriguez, C.; Wu, C.; Pasek-Allen, J.; Khosla, K.; Bischof, J.; Mangolini, L.; Aguilar, G. Photothermal Heating of Titanium Nitride Nanomaterials for Fast and Uniform Laser Warming of Cryopreserved Biomaterials. *Front. Bioeng. Biotechnol.* **2022**, *10* (August), 1–14. https://doi.org/10.3389/fbioe.2022.957481.

(73) Sabzeghabae, A. N.; Berrospe-Rodriguez, C.; Mangolini, L.; Aguilar, G. Laser-Induced Cavitation in Plasmonic Nanoparticle Solutions: A Comparative Study between Gold and Titanium Nitride. *J. Biomed. Mater. Res. - Part A* **2021**, *109* (12), 2483–2492. https://doi.org/10.1002/jbm.a.37242.

(74) Gao, Y.; Zhang, X.; Li, Y.; Liu, H.; Wang, Y.; Chang, Q.; Jiao, W.; Song, Y. Saturable Absorption and Reverse Saturable Absorption in Platinum Nanoparticles. *Opt. Commun.* **2005**, *251* (4–6), 429–433.

https://doi.org/10.1016/j.optcom.2005.03.003.

(75) Un, I. W.; Sivan, Y. Thermo-Optic Nonlinearity of Single Metal Nanoparticles under Intense Continuous Wave Illumination. *Phys. Rev. Mater.* **2020**, *4* (10), 1–15. https://doi.org/10.1103/PhysRevMaterials.4.105201.

(76) Ge, Z.; Cahill, D. G.; Braun, P. V. AuPd Metal Nanoparticles as Probes of Nanoscale Thermal Transport in Aqueous Solution. *J. Phys. Chem. B* **2004**, *108* (49), 18870–18875. https://doi.org/10.1021/jp048375k.

(77) Wiame, H.; Centeno, M.-A.; Picard, S.; Bastians, P.; Grange, P. Thermal Oxidation Under Oxygen of Zirconium Nitride Studied by XPS, DRIFTS, TG-MS. Journal of the European Ceramic Society 1998, pp 1293–1299.

(78) Repoux, M. Comparison of Background Removal Methods for XPS. *Surf. Interface Anal.* **1992**, *18* (7), 567–570. https://doi.org/10.1002/sia.740180719.

# Chapter 3: Plasmonic Nanoparticle Photochemistry with Methanol

## 3.1: Introduction

In addition to contributing to public health by reducing carcinogens out of water, plasmonic particles have the potential to efficiently photocatalyzed other necessary chemical reactions as well. It is not only energy production that relies heavily relies on fossil fuels but also producing chemicals for moder life such as ammonia, chlorine, among others requires inputting energy to overcome the activation energies. The energy required to produce nitrogen and hydrogen is in addition to the fact that ammonia production accounts for 1-2% of global energy consumption, 3% of global carbon emissions and 3-5% of natural gas consumption.[1]

The world population has been able to increase as much as it has is due to the production of ammonia which is a critical fertilizer for growing crops providing nitrogen to the soil. The current production method is the Haber-Bosch which creates ammonia from Nitrogen and Hydrogen but since the reaction is decreasing in entropy or the number of molecules, even though the process is exothermic it is not easy to facilitate. The process is so energy intensive that the catalyst is of utmost importance because the whole.

Plasmonic materials are able to convert visible radiation to chemical energy to potentially reduce the energy to produce nitrogen, hydrogen and then ammonia. Plasmonic nanoparticles use LSPR relaxation through Landau damping that happens during the first 100 fs and produces an electric field to the localized medium providing a direct charge

transfer under the right conditions.[2] After around 100 fs, the plasmonic nanoparticle provides thermal energy to its surroundings.

Experimental researcher to deconvolve the photocatalyctic mechanisms of plasmonic particles between the thermal and electric mechanisms is ongoing in the field. Recently, a theory considering only photothermal processes described the increased catalytic performance with plasmonic nanoparticles.[3] The group argued that experimental errors resulted in the underestimation of the photothermal effects in some cases and in others the increased photocatalyctic activity when comparing light and dark conditions did not agree with the increase in hot electrons.[4,5] A number of papers have also shown that the effect of the thermal gradient surrounding the particles complicates the ability to measure the particle temperature (with thermocouples), while the reaction is taking place and could play a crucial part in the catalytic process. [6–8]

The purely photothermal theory provided is in better agreement with the original data published with a minimum number of fit parameters.[3] Thermal chemical reactions are catalyzed by temperature according to Arrhenius law:

$$R = R_0 \, exp\left(-\frac{\varepsilon_a}{k_B T}\right) \qquad (3.1)$$

Where $k_b$ is the Boltzmann constant, $\varepsilon_a$ is the reaction activation energy, T is the temperature of the reactor and $R_0$ is a constant that depends on the details of the reactants. The Arrhenius' law applies with bulk solution reactions and is a measure of the average temperature but at the nanoscale surrounding the particles in plasmonic photocatalytic reactions, there could be large gradients surrounding the particle due to its LSPR response.

To account for a possible thermal gradient in the near field of the nanoparticles, Dubi argue that the temperature dependence of the rate of reaction using Arrhenius' law, the temperature must be shifted like:[3]

$$T(I_{inc}) = T_{dark} + \alpha I_{inc} \qquad (3.2)$$

Where $T_{dark}$ is the temperature in the dark with no illumination, $\alpha$ is the photothermal conversion coefficient and $I_{inc}$ is the intensity of illumination.

Refitting the previously published data, the increased catalectic performance, originally explained due to increased light intensity, could be accounted for by an increase in temperature to drive the reaction.[3] This result highlights how the photothermal effect among others of plasmonic nanoparticles should be investigated. Direct electron transfer or hot electron energy transfer could be a driving mechanism for plasmonic catalysts in some reactions, for instance research suggests in oxidation-reduction reactions charge transfer is the specific pathway.[9] The experimental problem lies in trying to measure the temperature of the particle during a light-matter interaction.

The surface area to volume ratio is another property of plasmonic materials that can be leveraged as a photocatalyst. The LSPR field lines are located on the surface of the particle and chemical reactions progress on the surface of the particles as well. The larger surface area provides more opportunities for chemistry to proceed making the overall process more efficient as well as providing a larger area for biomedical applications like drug delivery and biosensing.

The work here provides a foundation for using an alternative plasmonic material like ZrN for photochemical applications. First, I show that both ZrN and TiN are viable candidates

as for photocatalytic applications with ZrN being more efficient at reducing platinum 4+ to platinum. Then photocatalytic experiments are done to compare the photocatalytic efficiencies between ZrN and TiO2 to reduce the carcinogen chromium (VI) to chromium (III). As semiconductors are also able to use radiation with energies higher than the material's bandgap to create chemical energy, I show that ZrN is able to use both UV radiation as well as visible light more efficient $TiO_2$.

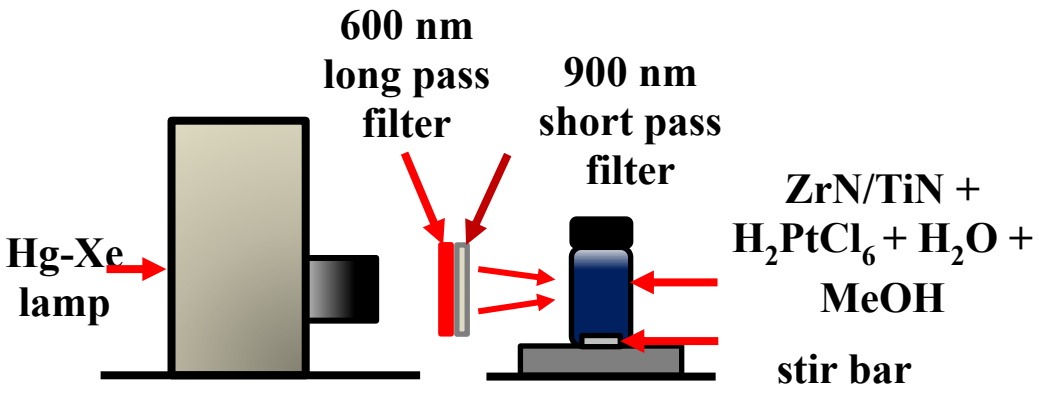


*Figure 3.1. The experimental setup for Pt deposition experiments. Light from a 500 W Hg-Xe Newport 67005 arc Lamp was filtered to only include the visible spectrum (600-900 nm) to illuminate a reaction vial containing a 90:10 volume ratio of Water to methanol, ZrN or TiN nanoparticles, and 70 μM of $H_2PtCl_6$.*

### 3.2: Platinum Experimental Methods

Platinum photo deposition experiments were performed using a 500 W Hg-Xe Newport 67005 arc lamp to illuminate the samples. The spectrum of light coming from the arc lamp is the same as shown in figure 3 in chapter 2. A solution of alternative plasmonic nanoparticles (TiN or ZrN), water, methanol and $H_2PtCl_6$ is placed in a reaction vial. As displayed in figure 1 above, the lamp was placed 23 cm away from the reaction vial and

full spectrum of light was filtered with two optical filters (600 nm long pass filter and a 900 nm short pass filter from Edmund Optics) to isolate visible part of the spectrum from 600 nm to 900 nm. In another experiment with a similar setup, we spectrally resolved the incoming light to isolate specific wavelengths within the visible part of the spectrum using a Monochromator (Horiba Scientific) to determine the photodeposition rate as a function of wavelength.

The reaction vial was 20 ml in total containing 90% by volume $H_20$, 10% by methanol. 160 μM of particles is added to the solution. After sonicating the vial for 10 min to ensure a homogonous mixture, $H_2PtCl_6$ was added at a concentration of 70 μM. Control samples were immediately wrapped in aluminum foil to prevent any illumination. The maximum temperature achieved during illumination was 40°C. Control samples were covered in aluminum were placed on a hot plate at 40°C to determine whether temperature played a significant role in the deposition of Pt onto the particles. Different samples were illuminated for 0, 30, 60, 120 and 240 minutes The pH was 4.0 for all the experiments.

After illumination, the solution in the vial was transferred to a centrifuge tube. The sample was washed in the centrifuge 3 times using distilled $H_2O$ to remove and leftover remains from the reaction and leave only the Pt deposited on to the particles. TEM samples were prepared by drop casting the centrifuge rinsed particles onto a lacey carbon copper grid. The high-resolution TEM images were obtained with an FEI Titan Themis 300 instrument with energy dispersive X-ray spectroscopy (EDX) capabilities for elemental mapping. EDX characterization was performed with an FEI Nova Nano-SEM450 system with an Oxford Instruments Aztec Synergy software and an X-max 50 $mm^2$ detector with

resolution of 127 nm at Mn Kα. The working distance and accelerating voltage were kept at 5 mm and 20 kV respectively.

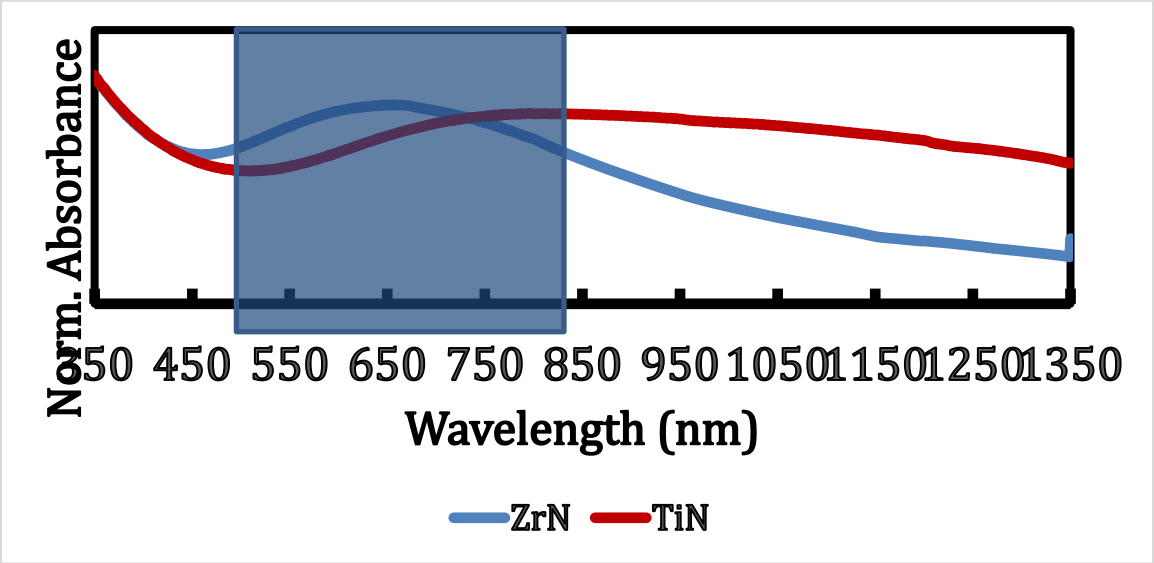


*Figure 3.2. The absorbance spectrum of ZrN (blue) and TiN (red) measured with a UV-Vis spectrometer. The grey area illustrates the wavelengths that entered into the solution for the pt deposition experiments*

### 3.3: Platinum Results and Discussion

Figure 2 shows a comparison of the extinction spectra for house made ZrN and TiN nanoparticles. As shown in the figure, the ZrN nanoparticles have a more intense extinction peak centered around 600 nm. TiN has a red-shifted peak centered around 800 nm extinction spectra that is broader than ZrN. The absorption spreads into the NIR window where light is able to pass through skin and tissues without damaging.[10] This property shows the potential for TiN to be a good material for bio applications using wavelengths in the N. The shaded region shows the part of the spectrum that will reach the particles due to the filters.

Only the wavelengths from 600-900 nm will reach the reaction vial due to the filters. This is so that the visible part of the spectrum could be isolated to measure the photochemistry potential without using light energetic enough, below 600 nm, to support interband transitions in the material.[11]

Inside the reaction vial, the Pt ion in $H_2PtCl_6$ is missing four electrons that must be acquired to reduce Pt to its metallic state. Methanol is used as a sacrificial electron doner to enhance the speed of the reaction rather than requiring the oxidation of water.[12,13] The light-matter interaction with the plasmonic nanoparticles facilitates the reduction of Pt in the following reaction:

$$PtCl_6^{2-} + 4e^- \rightarrow Pt^0 + 6Cl^- \qquad (3)$$

While the other half reaction oxidizing methanol goes as:

$$CH_3OH + H_2O + 6h^+ \rightarrow CO_2 + 6H^+ \qquad (4)$$

The oxidation of methanol is well characterized and studied using $TiO_2$ that was platinized[14] as well as using $TiO_2$ supported ZrN and TiN.[15] We suspect that the 6 protons in reaction 2 combine with the $Cl^-$ in reaction 1 to form HCL in the solution.

Figure 3 displays the high-resolution TEM images of ZrN nanoparticle before 0 min and after 240 minutes of the postdeposition experiment. The 20 ml vials contained deionized water, 2 ml of methanol (10% by volume), 70 μM of $H_2PtCl_6$ and 160 μM of ZrN particles was exposed to light to photo deposit the Pt for the duration of 240 minutes. After illumination, the samples were carefully washed with deionized water and centrifuged three times to remove any contaminants.

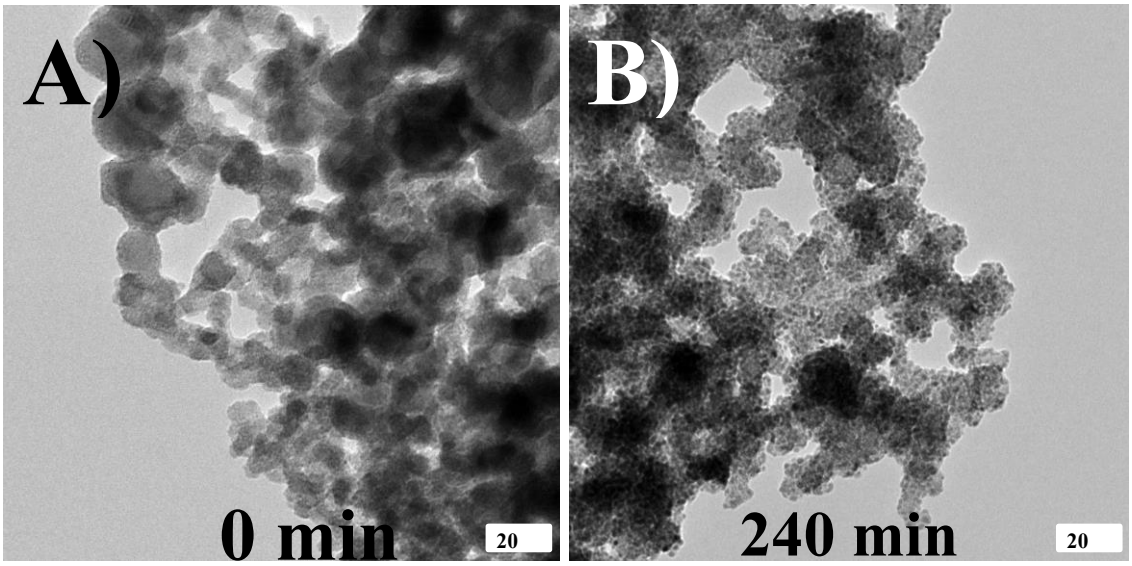


*Figure 3.3. TEM Images of ZrN nanoparticles centrifuged and washed after getting illuminated with visible light for A) 0 min and B) 240 min. The small black specs in B) are Pt deposited on to the ZrN nanoparticles.*

As shown from the images, small black Pt clusters are not on the particles at 0 min but after 240 min they cover the particles. The reduction of $Pt^{4+}$ to Pt removes the ions from solution onto the ZrN particles. The illumination is only using wavelengths between 600 and 900 nm highlighting the ability of ZrN to perform photochemistry with visible wavelengths that cannot induce interband transitions.

To see how much the Pt deposition increased in time we compare the atomic ration of photodeposition of Pt to TiN/ZrN particles. Figure 4 shows how the photodeposition ratio increases after the solutions were illuminated for 30, 60, 120 and 240 minutes. Once again, the reaction vial is illuminated with only visible wavelengths (600-900 nm). The 240 min sample is the same sample for ZrN in figure 4 is shown with TEM in figure 3.

After illumination of the samples was complete, the vials were again centrifuged and washed with water three times to remove any potential contaminants and leave only the photo deposited Pt and TiN nanoparticle to perform EDX measurements to determine the atomic ratio between Pt and Ti/Zr such that the photo deposition rates could be compared. It is clear that the ZrN is much more efficient in the reduction of platinum over time.

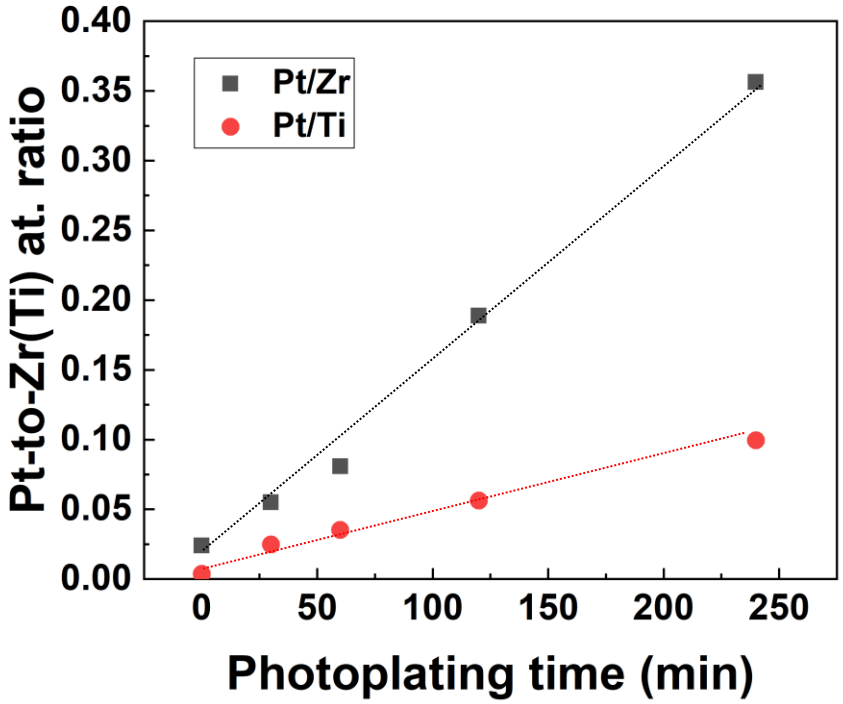


*Figure 3.4. Displays the Pt-Zr (Ti) atomic ratio as a function of photo plating time from photons with wavelengths between 600-900 nm. As the time of illumination is increased the amount of Pt deposited onto the particles also increases. The figure shows ZrN particles reduce Pt more efficiently than TiN.*

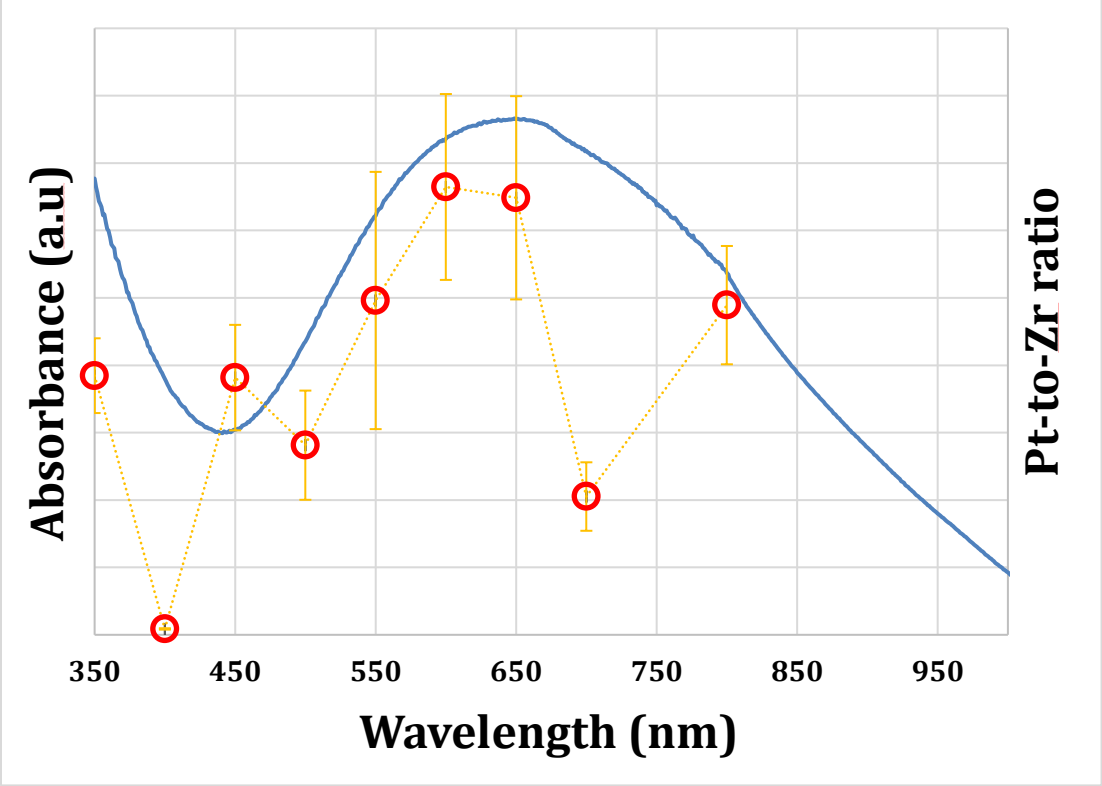


*Figure 3.5. Absorption of ZrN nanoparticles plotted on top of an action plot showing the Pt-Zr ratio (Red circles) for with spectrally selected radiation using a monochromator. The absorption spectrum closely follows the Pt-Zr ratio providing evidence for plasmonic driven photochemistry. Each sample was illuminated for 1 hour at each wavelength.*

Finally, in figure 5, we use a monochromator to spectrally select wavelengths from 350-900 nm to see how the plasmonic response of ZrN would affect the photo deposition rate. Each sample was illuminated for 1 hour at each wavelength using the same procedure as before. The 20 ml vials contained 10% volume of methanol, 70 μM of chloroplatinic acid, and a ZrN particle concentration of 160 μM. The absorbance spectrum is shown on the left axis while the Pt-Zr ratio is on the right. As shown in the figure, the absorbance spectrum of ZrN closely correlates with the Pt-Zr ratio providing significant evidence for ZrN as a plasmon driven photocatalyst.

### 3.4: Cr (VI) Experimental Methods

The experimental setup for these experiments was exactly the same as the one described in chapter 2. Figure 2 of chapter 2 shows the setup for the experiment with the only difference being that the solution also contained 5% methanol by volume to facilitate the reaction. As the previous experiments, the concentration of chromium (VI) was determined with the diphenyl carbazide method.

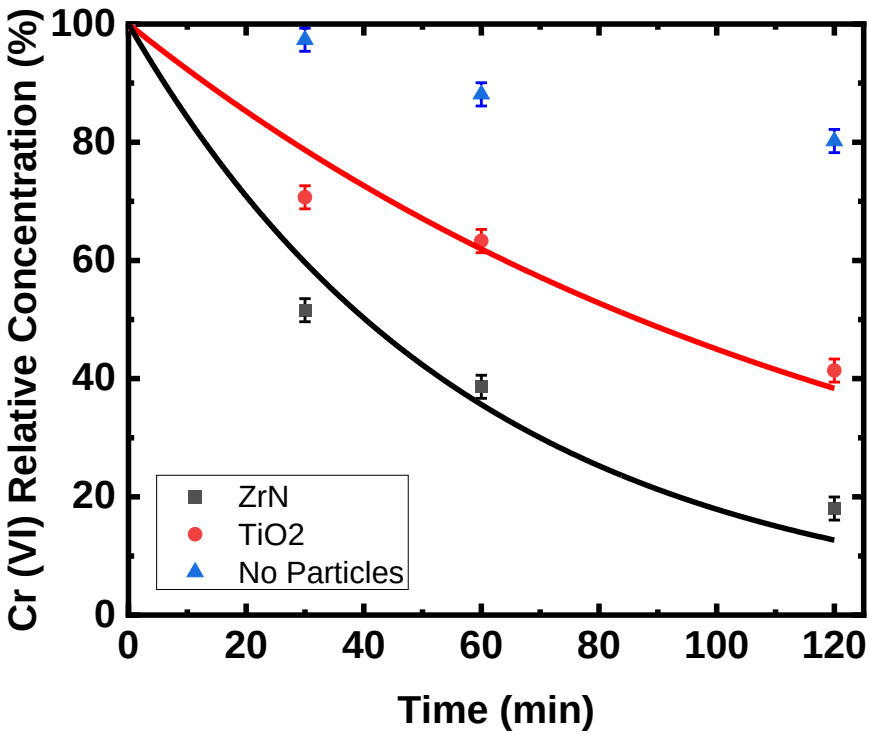


*Figure 3.6. Cr (VI) Reduction Time Study. Solution of Particles, Methanol and Cr (VI) was illuminated with 3 W/cm$^2$ to compare the reduction speed with No particles (Blue Triangles), 1 g/L of $TiO_2$ nanoparticles (Red Circles), and 1 g/L ZrN (Black Squares). The photoreduction was fitted with an exponential decay function for ZrN (Black line) and $TiO_2$ (Red line).*

### 3.5: Cr (VI) Reduction Results and Discussion

First, we compared the Cr (VI) reduction kinetics between ZrN and $TiO_2$. The results of this experiment are shown in Figure 6. The nanoparticle concentration is 1 g/L for both samples. The solutions are optically thick as in the previous experiment meaning no light is passing through the solution. Figure 6 shows the change in the Cr (VI) concentration during light exposure measured using the colorimetric method described earlier. The initial Cr (VI) concentration for all these measurements is 0.55 mM. The measurements shown in Figure 6 are normalized to the initial Cr (VI) concentration.

Absorption of photons by either ZrN or $TiO_2$ nanoparticles provides the energy to create electron hole pairs, while the presence of methanol, acting as a hole scavenger, reduces the energy barrier of the oxidation reaction and decreases the rate of charge recombination in the material.[13,17,18] The concentration of Cr (VI) is measured by the diphenyl carbazide method[16], before and after illumination for different light exposure times. A clear decrease in Cr (VI) concentration is observed when $TiO_2$ or ZrN nanoparticles are illuminated. We find that the rate of reduction is faster for the ZrN solution. After 3 hours, more than 80% of the Cr (VI) ions have been reduced for the case of ZrN compared to roughly 60% for the case of $TiO_2$. Similar results have been reported by Valari et al., where they use the same amount of titania powders but less methanol in the solution, showing a reduction to 30% of Cr (VI) within two hours.[17] It should be noted that our measurements are performed at a pH of 5, which is expected to lead to a slower reduction rate than the pH of 2.5 used by Valari et al.

Ku et al. 2001 found that the rate of photoreduction can be fit properly with a pseudo-first-order Langmuir-Hinshelwood kinetics expression:[19]

$$ln\left[\frac{Cr(VI)_0}{Cr(VI)}\right] = k_{red}t \qquad (3.5)$$

Where $k_{red}$ is the photocatalytic reduction rate constant and t is the illumination time in minutes. When applying this expression to our measurements, we find the initial rate to be 0.022 $min^{-1}$ for ZrN and 0.012 $min^{-1}$ for $TiO_2$. In close conditions, Ku et al. found that the rate constant was similar to ours for $TiO_2$.[19] The rate slowed to .015 and .007 $min^{-1}$ for ZrN and $TiO_2$ respectively in the last 90 minutes of illumination, with ZrN continuing to have twice the rate constant of $TiO_2$. The rate constant for the control remained at about 0.002 $min^{-1}$ for the duration of the exposure time.

Overall, these results confirm that both $TiO_2$ and ZrN can drive the photoreduction of Cr (VI) ions to Cr (III). The photoreduction is expected to proceed via the formation of charge carriers in the active material, followed by their reaction with surface-bound Cr (VI) ions. The reduction of Cr (VI) to Cr (III) requires three electrons per Cr (VI) ion:[17]

$$Cr_2O_7^{2-} + 14H^+ + 6e^- \rightarrow 2Cr^{3+} + 7H_2 \qquad (3.6)$$

For the oxidation half-reaction, methanol acts as a sacrificial hole scavenger:[20]

$$CH_3OH + H_2O + 6h^+ \rightarrow CO_2 + 6H^+ \qquad (3.7)$$

The addition of methanol lowers the energy barrier to the oxidation half reaction, significantly enhancing the overall rate of reaction.

We should point out that there is a measurable reduction in Cr (VI) concentration (20% over the course of 2 hours) even without any particles added to the solution. This is likely

caused by methanol itself. It has been reported that methanol can be oxidize to form formaldehyde when exposed to UV radiation and even reduce hexachloroplatinate (IV) to metal.[21] In addition, no photoreduction is observed in the control sample without methanol.

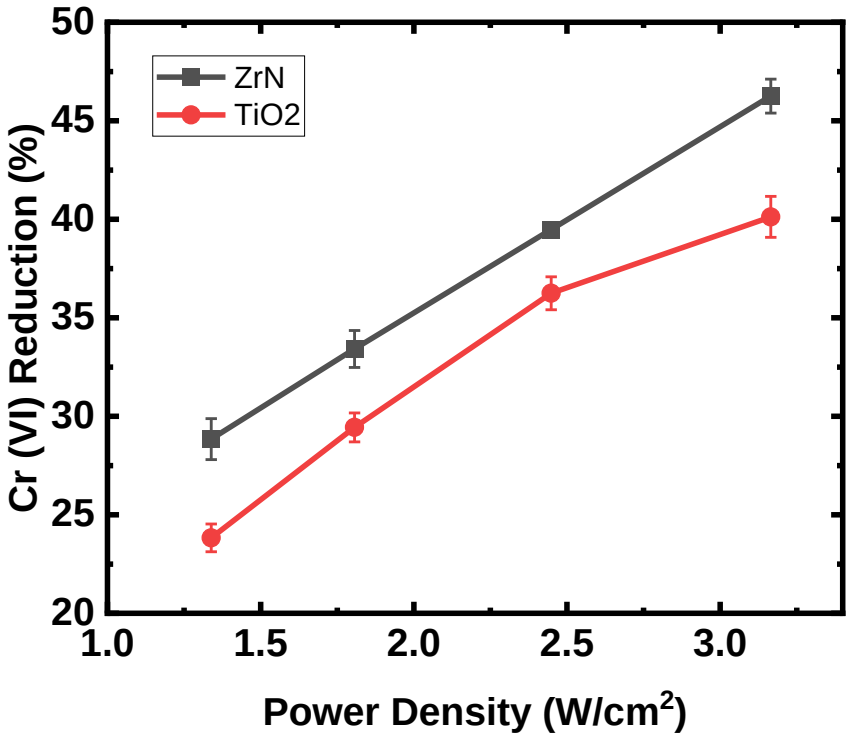


*Figure 3.7. The power study shows how the reduction of Cr (VI) increases with increased power density after 3 hours of illumination. All experiments were performed with 500 mg/L of particles and 5% by volume of Methane, 1 ml. ZrN (Black Squares) reduces more than $TiO_2$ (Red circles) at every power density.*

To further investigate the origin of the photoreduction mechanism for these two materials, we have measured the kinetics of photoreduction as a function of input photon flux. The results are shown in Figure 7, in which we plot the fraction of Cr (VI) reduction observed after a 3 hours illumination, as a function of optical power density. For these measurements,

the particle concentration is 500 mg/L for both $TiO_2$ and ZrN. As for the previous experiment, 5% volume of methanol is added to facilitate the reaction. As is evident in Figure 7, the reduction rate for both ZrN and $TiO_2$ increased with the power density. The rate of reaction is always larger for ZrN than $TiO_2$, consistent with the results shown in Figure 6. The kinetic photoreduction rate constant calculated from Equation 1 increased from .0019 to .0034 $min^{-1}$ for ZrN and .0015 to .0028 $min^{-1}$ for $TiO_2$ as the power increased from 1.3 $W/cm^2$ to 3.2 $W/cm^2$.

We therefore observe a sublinear dependence of photocatalytic rate on intensity (rate $\propto$ $intensity^n$, with $n < 1$). As the photon flux increases, the rise in material excitation competes with an increased rate of recombination of the photo-generated carriers, limiting the gain in photoreduction rate and leading to a sublinear dependence. Similar results have been reported by Xing et al. They find that the reaction rate for $Au/TiO_2$ has a super-linear law dependence on the light intensity ($n > 1$) between 0 – 0.7 $W/cm^2$. However, from 0.7 to 0.9 $W/cm^2$, the dependency becomes sub-linear ($n < 1$). This means that the increment of the photocatalytic rate is smaller when the light intensity exceeds – 0.7 $W/cm^2$. [22] As the intensity of our experiments was higher than .7 $W/cm^2$, it makes sense that our n-value would be less than 1. Nevertheless, linear or weakly sublinear trend is consistent with an electronic excitation mechanism, in which the reduction is promoted by charge carriers as opposed to a thermally driven (photothermal) process. An exponential dependence would be expected for the case in which the incoming photons are simply converted to thermal energy, with the increase in particle temperature then driving the reaction.[3] We clearly do

not observe this in our experiments. In addition, a cooling coil is used to keep the temperature constant in the solution and equal to 27°C for all the measurements.

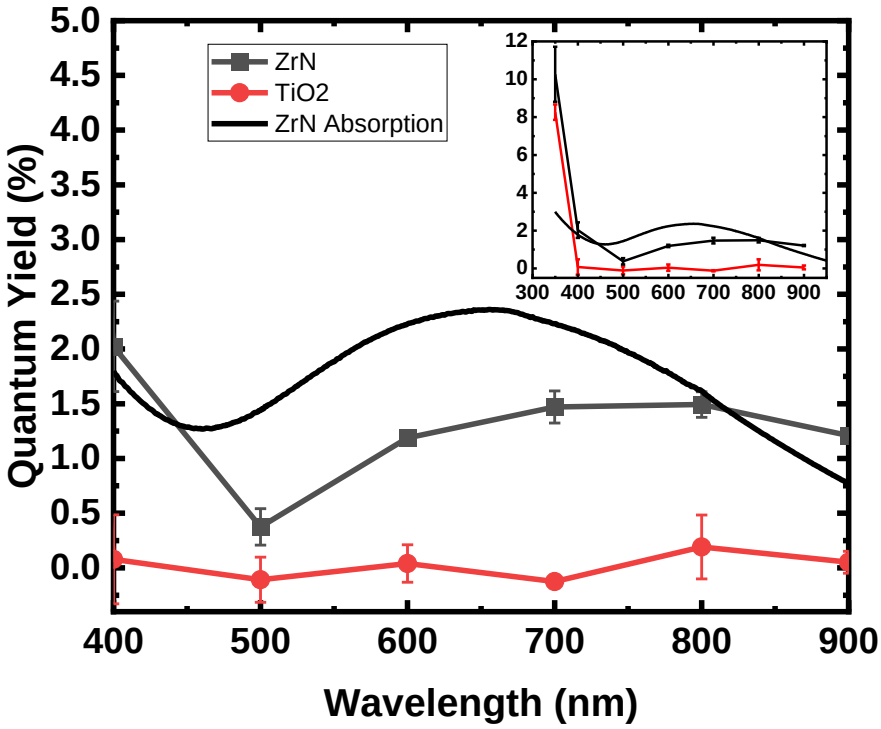


*Figure 3.8. Action Plot showing the Quantum Yield for ZrN (Black Squares) and $TiO_2$ (Red Circles) with spectrally selected radiation using a monochromator. Each sample was illuminated for 3 hours at each wavelength with 1 g/L of nanoparticles in solution. The normalized absorption of ZrN is overlayed on the plot for comparison with the quantum yield of ZrN. The inlay expands the plot to include the QY at 350 nm which is also more efficient for ZrN than $TiO_2$.*

Next, we test our hypothesis that the increased reduction in previous experiments is due to the capability of ZrN to utilize the visible part of the spectrum. To do that, we have performed Cr (VI) reduction experiments with ZrN and $TiO_2$, at a concentration of 1 g/L of particles, with 1 ml of methanol in solution. A monochromator has been used to

spectrally resolve the radiation from our broadband light source. The solutions are illuminated for 3 hours at selected wavelength. The quantum yield (QY) is calculated using the measured photon flux and the equation from Li et al:[23]

$$Quantum\ yield = \frac{\#\ ions\ reduced}{\#\ absorbed\ photons} \qquad (3.8)$$

Figure 8 shows the QY as a function of excitation wavelength for ZrN and $TiO_2$. As a reference, we also plot the absorption spectrum for the ZrN particles. As expected, the QY for $TiO_2$ in the visible is zero, meaning no reduction is observed as visible illumination is below the optical bandgap of the material. On the other hand, we observe a reasonably high internal QY for the case of ZrN, peaking at ~1.3% at 700 nm. Most importantly, the QY dependence for ZrN closely resembles the absorption spectrum of the material, confirming that the photoreduction process is initiate by radiation which couples into the material via its inherent plasmonic response. Interestingly both ZrN and $TiO_2$ have reasonably high QY in the UV part of the spectrum with ZrN outperforming $TiO_2$ (8% for $TiO_2$ and slightly above 8% for ZrN).

### 3.6: Conclusions

We have demonstrated that plasmonic ZrN nanoparticles can effectively reduce heavy metal ions and oxidize methanol with not only UV light but by utilizing visible light as well. Compared to TiN nanoparticles, ZrN achieve a faster reduction kinetics reducing platinum. ZrN achieved a reasonable internal quantum yield even in the visible part of the spectrum for the reduction of both platinum and Cr (VI). The strong correlation between the absorption spectrum and the internal quantum yield demonstrates the plasmon driven

photochemistry. We have also found a sub-linear dependence on the reduction kinetics with the illumination power, which is not consistent with a photo-thermal effect but rather with the photo-generation of charge carriers. Overall, these results provide additional convincing evidence of the great potential of alternative plasmonic materials for applications in photochemistry. In particular, their abundance and ability to use the solar spectrum make them an attractive platform for water treatment applications.

### 3.7: References


(1) Song, Y.; Johnson, D.; Peng, R.; Hensley, D. K.; Bonnesen, P. V.; Liang, L.; Huang, J.; Yang, F.; Zhang, F.; Qiao, R.; Baddorf, A. P.; Tschaplinski, T. J.; Engle, N. L.; Hatzell, M. C.; Wu, Z.; Cullen, D. A.; Meyer, H. M.; Sumpter, B. G.; Rondinone, A. J. A Physical Catalyst for the Electrolysis of Nitrogen to Ammonia. *Sci. Adv.* **2018**, *4* (4), 1–8. https://doi.org/10.1126/sciadv.1700336.

(2) Brongersma, M. L.; Halas, N. J.; Nordlander, P. Plasmon-Induced Hot Carrier Science and Technology. *Nat. Nanotechnol.* **2015**, *10* (1), 25–34. https://doi.org/10.1038/nnano.2014.311.

(3) Dubi, Y.; Un, I. W.; Sivan, Y. Thermal Effects - an Alternative Mechanism for Plasmon-Assisted Photocatalysis. *Chem. Sci.* **2020**, *11* (19), 5017–5027. https://doi.org/10.1039/c9sc06480j.

(4) Sivan, Y.; Baraban, J. H.; Dubi, Y. Experimental Practices Required to Isolate Thermal Effects in Plasmonic Photo-Catalysis: Lessons from Recent Experiments. *OSA Contin.* **2020**, *3* (3), 483. https://doi.org/10.1364/osac.376809.

(5) Dubi, Y.; Sivan, Y. "Hot" Electrons in Metallic Nanostructures—Non-Thermal Carriers or Heating? *Light Sci. Appl.* **2019**, *8* (1). https://doi.org/10.1038/s41377-019-0199-x.

(6) Li, H.; Rivallan, M.; Thibault-Starzyk, F.; Travert, A.; Meunier, F. C. Effective Bulk and Surface Temperatures of the Catalyst Bed of FT-IR Cells Used for in Situ and Operando Studies. *Phys. Chem. Chem. Phys.* **2013**, *15* (19), 7321–7327. https://doi.org/10.1039/c3cp50442e.

(7) Li, X.; Zhang, X.; Everitt, H. O.; Liu, J. Light-Induced Thermal Gradients in Ruthenium Catalysts Significantly Enhance Ammonia Production. *Nano Lett.* **2019**, *19* (3), 1706–1711. https://doi.org/10.1021/acs.nanolett.8b04706.

(8) Zhang, X.; Li, X.; Reish, M. E.; Zhang, D.; Su, N. Q.; Gutiérrez, Y.; Moreno, F.; Yang, W.; Everitt, H. O.; Liu, J. Plasmon-Enhanced Catalysis: Distinguishing Thermal and Nonthermal Effects. *Nano Lett.* **2018**, *18* (3), 1714–1723. https://doi.org/10.1021/acs.nanolett.7b04776.

(9) Sarina, S.; Jaatinen, E.; Xiao, Q.; Huang, Y. M.; Christopher, P.; Zhao, J. C.; Zhu, H. Y. Photon Energy Threshold in Direct Photocatalysis with Metal Nanoparticles: Key Evidence from the Action Spectrum of the Reaction. *J. Phys. Chem. Lett.* **2017**, *8* (11), 2526–2534. https://doi.org/10.1021/acs.jpclett.7b00941.

(10) Xue, D.; Wang, Y.; Zhang, H. Advances of NIR Light Responsive Materials for Diagnosis and Treatment of Brain Diseases. *Adv. Opt. Mater.* **2023**, *2202888*,

2202888. https://doi.org/10.1002/adom.202202888.

(11) Naldoni, A.; Guler, U.; Wang, Z.; Marelli, M.; Malara, F.; Meng, X.; Besteiro, L. V.; Govorov, A. O.; Kildishev, A. V.; Boltasseva, A.; Shalaev, V. M. Broadband Hot-Electron Collection for Solar Water Splitting with Plasmonic Titanium Nitride. *Adv. Opt. Mater.* **2017**, *5* (15), 1–11. https://doi.org/10.1002/adom.201601031.

(12) Ni, M.; Leung, M. K. H.; Leung, D. Y. C.; Sumathy, K. A Review and Recent Developments in Photocatalytic Water-Splitting Using TiO2 for Hydrogen Production. *Renew. Sustain. Energy Rev.* **2007**, *11* (3), 401–425. https://doi.org/10.1016/j.rser.2005.01.009.

(13) Schneider, J.; Bahnemann, D. W. Undesired Role of Sacri Fi Cial Reagents in Photocatalysis. **2013**, 3479–3483.

(14) Kandiel, T. A.; Dillert, R.; Robben, L.; Bahnemann, D. W. Photonic Efficiency and Mechanism of Photocatalytic Molecular Hydrogen Production over Platinized Titanium Dioxide from Aqueous Methanol Solutions. *Catal. Today* **2011**, *161* (1), 196–201. https://doi.org/10.1016/j.cattod.2010.08.012.

(15) Baturina, O. A.; Epshteyn, A.; Leff, A. C.; Purdy, A. P.; Brintlinger, T.; Simpkins, B. S.; Santiago, E. Y.; Govorov, A. O. Photoelectrochemical Methanol Oxidation Under Visible and UV Excitation of TiO 2 -Supported TiN and ZrN Plasmonic Nanoparticles . *J. Electrochem. Soc.* **2021**, *168* (1), 016503. https://doi.org/10.1149/1945-7111/abd605.

(16) Lace, A.; Ryan, D.; Bowkett, M.; Cleary, J. Chromium Monitoring in Water by Colorimetry Using Optimised 1,5-Diphenylcarbazide Method. *Int. J. Environ. Res. Public Health* **2019**, *16* (10). https://doi.org/10.3390/ijerph16101803.

(17) Valari, M.; Antoniadis, A.; Mantzavinos, D.; Poulios, I. Photocatalytic Reduction of Cr(VI) over Titania Suspensions. *Catal. Today* **2015**, *252*, 190–194. https://doi.org/10.1016/j.cattod.2014.10.014.

(18) Shifu, C.; Gengyu, C. Study on the Photocatalytic Reduction of Dichromate and Photocatalytic Oxidation of Dichlorvos. *Chemosphere* **2005**, *60* (9), 1308–1315. https://doi.org/10.1016/j.chemosphere.2005.01.056.

(19) Ku, Y.; Jung, I. L. Photocatalytic Reduction of Cr(VI) in Aqueous Solutions by UV Irradiation with the Presence of Titanium Dioxide. *Water Res.* **2001**, *35* (1), 135–142. https://doi.org/10.1016/S0043-1354(00)00098-1.

(20) Schneider, J.; Bahnemann, D. W. Undesired Role of Sacrificial Reagents in Photocatalysis. *Journal of Physical Chemistry Letters*. 2013, pp 3479–3483. https://doi.org/10.1021/jz4018199.

(21) Wojnicki, M.; Kwolek, P. Reduction of Hexachloroplatinate(IV) Ions with Methanol under UV Radiation. *J. Photochem. Photobiol. A Chem.* **2016**, *314*, 133–142.

(22) Xing, X.; Tang, S.; Hong, H.; Jin, H. Concentrated Solar Photocatalysis for Hydrogen Generation from Water by Titania-Containing Gold Nanoparticles. *Int. J. Hydrogen Energy* **2020**, *45* (16), 9612–9623. https://doi.org/10.1016/j.ijhydene.2020.01.197.

(23) Li, K.; Hogan, N. J.; Kale, M. J.; Halas, N. J.; Nordlander, P.; Christopher, P. Balancing Near-Field Enhancement, Absorption, and Scattering for Effective Antenna-Reactor Plasmonic Photocatalysis. *Nano Lett.* **2017**, *17* (6), 3710–3717. https://doi.org/10.1021/acs.nanolett.7b00992.

# Chapter 4: Spray Pyrolysis of Yttria-Stabilized Zirconia Nanoparticles and Their Densification into Bulk Transparent Windows

## 4.1: Introduction

The potential for high strength, high toughness, temperature resistance and optical transparency makes Yttria-Stabilized Zirconia (YSZ) an extremely versatile material for a broad and diversified variety of applications such as bio-implants,[1,2] thermal barrier coatings[3] and solid oxide electrolytes.[4] Zirconia is a hard and tough ceramic material with multiple allotropes similar to steel.[5] Due to the strong covalent nature of zirconia, at room temperature the material tends to stabilize in the monoclinic phase.[6] By increasing temperature above 1200ºC, it is possible to achieve the transformation of the crystalline structure from monoclinic to tetragonal and eventually cubic structure.[6,7] Upon cooling, the transformation between the tetragonal and the monoclinic phases and the associated 4-5% volume change can produce cracks and sample fracturing. Partially stabilized zirconia (PSZ) uses dopants to stabilize the material in the tetragonal phase. The addition of oversized ($Y^{3+}$ and $Gd^{3+}$) or undersized ($Fe^{3+}$ and $Ga^{3+}$) atoms can be used as an effective strategy to stabilize the material in the tetragonal or cubic phase even at room temperature. The larger ions favor an eightfold coordination number pulling oxygen away from the $Zr^{4+}$ ions creating vacancies.[8] The smaller ions favor a six-fold coordination number and compete for oxygen with the $Zr^{4+}$ ions.[8]

In addition, the mechanical stress induced by a propagating crack can provide the activation energy for the material to transform to the monoclinic phase, leading to a local volume

expansion and stopping crack propagation.[6,9–11] The transformation toughening phenomenon is a key property in improving the mechanical properties of partially stabilized zirconia. For many applications, it is highly desirable to combine the high toughness of PSZ with the optical transparency that is expected from an insulating material such as zirconia. However, synthesizing optically transparent zirconia is far from trivial. Light scattering can be induced when the dimensions of the grain sizes or pores are in the same order of the visible wavelength. To address this technical hurdle, the material must be produced with high density and small grain sizes.[12–16] Additionally, the presence of inhomogeneous crystal structures, such as a birefringent tetragonal phase in PSZ, introduces an additional source of scattering.[13,17] Finally, oxygen vacancies can be produced during the densification process. These vacancies absorb light at the blue end of the spectrum contributing to the lack of transparency.[18]

Commercially-produced YSZ nanopowders are available with either 3% molar (3YSZ) or 8% molar (8YSZ) Yttria ($Y_2O_3$) content and a particle size of around 50 nm. 7YSZ and 10YSZ are also available commercially but only tens of micron sized particles. A range of sub 50 nm particles have been synthesized using with between 1 and 4.5 percent yttria content as well as 8% yttria.[19] 10YSZ and 12YSZ were also synthesized using a precipitation method and were investigated to show that excess energy in the grain boundaries leads to a lower toughness.[20] However, due to the lack of optical characterization, in investigating higher yttria contents we would not have a comparison to make and out of the scope of this manuscript. 3YSZ is stabilized in the tetragonal phase with high hardness and toughness exhibiting the desired mechanical properties of zirconia

ceramics, but it lacks optical transparency. Fully-stabilized Zirconia can be produced at or above 8% $Y_2O_3$ (8YSZ). 8YSZ is stabilized in the cubic phase at room temperature and displays an isotropic structure that makes it ideal for optical transparency applications. However, 8YSZ has much lower strength and high brittleness compared with 3YSZ. Prior works have mainly investigated the mechanical and optical properties of commercial YSZ powders densified via spark plasma sintering (SPS) and have been limited to 3YSZ and 8YSZ, the only compositions available for off-the-shelf nanoparticles.[12,21,22]

In this study, we describe an aerosol spray pyrolysis technique that enables us to reproducibly synthesize YSZ nanoparticles with controlled compositions; we focus on the compositions between 3 and 8 percent $Y_2O_3$. With these material compositions and sizes – not available for commercial purchase – we investigate both the optical and mechanical properties of samples densified via SPS. Our ultimate goal is to identify the composition that gives an optimal balance between optical and mechanical properties with the hope of using yttria-stabilized zirconia for calvarium prothesis.[1] This type of implant could provide the mechanical support and also optical properties to image brain blood flow[23] or be used in therapeutic ultrasound treatments for brain diseases.[24]

## 4.2: Experimental Methods

### *4.2.1: YSZ Nanopowder Synthesis*

For the synthesis of YSZ, we employ aerosol spray pyrolysis, which is a common technique used to produce metal oxide nanoparticles.[25] Our application of this process functions at atmospheric pressure, making it advantageous for scalability. A schematic of the spray

pyrolysis system used in this work is shown in Figure 1. Approximately 85 g/mL solution of $ZrCl_4$ (Alfa Aesar) with $YCl_3$+$6H_2O$ (Sigma-Aldrich) is dissolved in deionized water in the desired compositions. 7000 SCCM of argon carrier gas is flown through a six-nozzle Collison-type nebulizer (BGI, Inc.) to generate an aerosol, which is then carried through a tube furnace. The powder production rate from this apparatus is approximately 100 g/hr. The aerosol is flowed into a 2-inch quartz tube placed in a temperature-controlled tube furnace. The solvent evaporates and the precursor is thermally decomposed by the high temperature of the furnace, nominally set to 900ºC, at which point nanoparticles nucleate. The product is collected downstream of the furnace on a stainless-steel mesh filter.

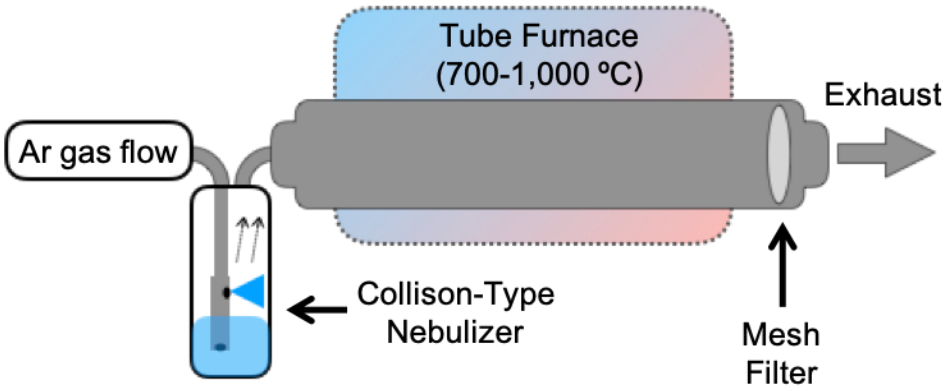


*Figure 4.1. Schematic of the YSZ aerosol spray pyrolysis synthesis apparatus.*

After collection, the powder is processed to ensure purity and reproducible quality. First, the material is dispersed in deionized water and cleaned of possible contaminants using a centrifuge. Then, the powder is annealed at 650ºC in air for 4 hours to remove any carbon deposits. Finally, the dry powder is ball-milled with cubic zirconia milling media at 60 RPM for 48 hours to break up any large agglomerates, which is beneficial for the sintering process. We use energy-dispersive X-Ray spectroscopy (EDS, Oxford Instruments) in a

scanning electron microscope (SEM, FEI Nova NanoSEM450) to determine the mole percent of Yttria in each powder sample. In addition, we use transmission electron microscopy (TEM, Tecnai12) analysis to determine the particle size distribution.

*4.2.2: YSZ Densification and Characterization*

After post-processing and characterizing the powder, it is densified via spark plasma sintering (SPS, Fuji-SPS Dr. Sinter Lab Jr.). 0.5 g of YSZ is loaded into a 10 mm graphite die and punch setup. The densification process is done completely under vacuum. The densification pressure is raised to 100 MPa before any current is applied. After applying the pressure, the sample is heated to 1100ºC at a rate of 200ºC/min and then to 1200ºC at a rate of 50ºC/min. The sample is held at this temperature for 10 min. The temperature is monitored with an external pyrometer.

After densification, the samples are polished to remove traces of carbon diffused from the graphite die. The surface polish is finished to 1 µm using a diamond slurry. The final thickness of the samples is 0.5 mm. Polishing the samples ensures that the measured density is only that of YSZ and not graphite contaminates. In addition, polishing reduces possible surface scattering for reliable transmittance measurement, and it provides a flat surface for hardness testing.

The density of the samples is characterized using the Archimedes method and expressed as a percentage with respect to the bulk theoretical density of 6.0 g/cm$^3$ for 6YSZ and 5.9 g/cm$^3$ for 8YSZ respectively which are used in the literature.[13,26–30] The in-line transmission of the samples is determined via UV-VIS spectrophotometry (Varian Cary

500) in a spectral range of 175nm-3000nm. We use a 2 mm mask to block any light not passing directly through the sample.

The densified samples are annealed in a furnace at 750ºC for 19 hours in air and the effect on the transparency and structure of the material is investigated. This process is introduced to remove oxygen vacancies created during the SPS process and hence improve transparency. The crystalline structure of the samples before and after the post densification annealing is characterized via X-Ray Diffraction (XRD, PANalytical Empyrean) and Raman Spectroscopy (Horiba LabRam HR). In addition, the cross section of the sintered samples is examined by SEM.

Finally, a Phase Two Vickers Indenter 900-391 is used to determine the hardness and toughness of the samples using a load of 98 N and a hold time of 15 seconds after air annealing. The toughness was determined by measuring the crack length from the indents and using Anstis' formula.[31]

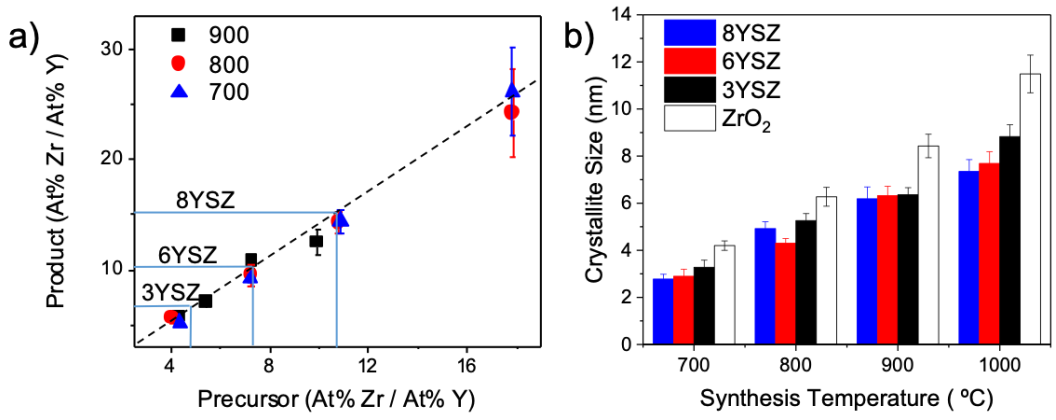


*Figure 4.2. a) EDS composition of YSZ samples produced at different temperatures and precursor compositions. The precursor composition is linearly related (black line) to the target YSZ compositions (3%, 6% and 8% molar Y2O3, highlighted by blue lines in the figure). B) Crystallite size calculated from Scherrer analysis of the 1st XRD peak for $ZrO_2$, 3YSZ, 6YSZ and 8YSZ.*

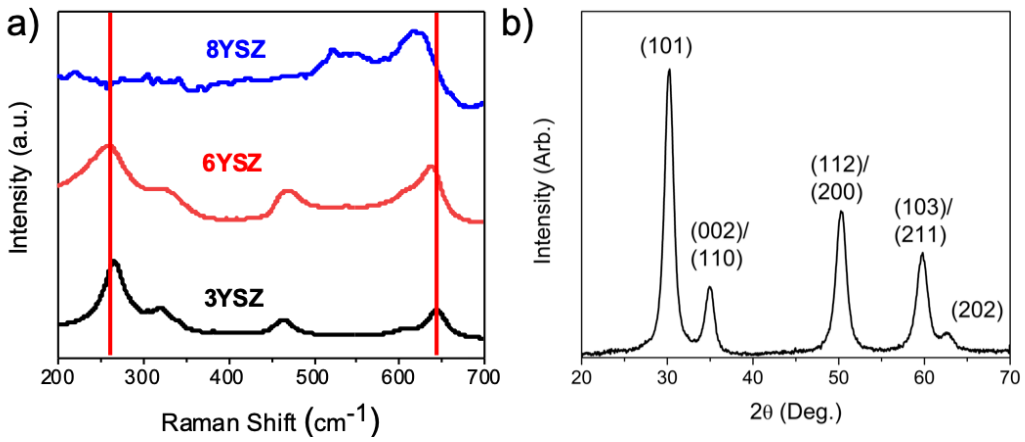


*Figure 4.3. a) Raman spectra from a series of samples produced at 900 ºC with different Yttria concentrations (increasing from bottom to top). The spectrum shifts from pure tetragonal phase (3YSZ) to pure cubic phase (8YSZ) with increasing dopant content. The vertical red lines indicate the gradual shift in the 640 $cm^{-1}$ peak position associated with tetragonal YSZ to 615 $cm^{-1}$ associated with cubic YSZ, as well as the disappearance of the 260 $cm^{-1}$ peaks going from tetragonal to cubic YSZ, with intermediate peak positions indicating a mixture of the two phases. b) XRD pattern of an 8YSZ sample.*

### 4.3: Results and Discussion

We started our investigation by carefully studying the relation between the process parameters of the spray pyrolysis process and the corresponding properties of the synthesized materials. At every processing temperature, the precursor composition appears linearly related to the yttria doping of the produced YSZ nanomaterials (see Figure 2a). While commercially only 3YSZ and 8YSZ are available, notably, our fabrication protocol enables a simple precursor concentration calibration to achieve any desired target composition (3YSZ, 6YSZ, and 8YSZ are indicated for reference in Figure 2a). Additionally, as depicted in Figure 2b, we can precisely tune the YSZ crystallite size from 3 nm to 10 nm by simply tuning the furnace temperature during the initial spray pyrolysis synthesis between 700 °C and 1,000°C. In the sintering experiments described later, the

synthesis temperature for nanoparticle production was fixed at 900°C based on the size range and quality of the produced material.

The phase of the material was investigated via XRD and Raman Spectroscopy. Figure 3a shows the Raman spectra for increasing amounts of yttria content. The 640 $cm^{-1}$ peak position of the tetragonal YSZ Raman spectrum shifts to 615 $cm^{-1}$ as the yttria content increases, which is indicative of a shift from tetragonal to cubic phase.[32] In addition, the peak at 260 $cm^{-1}$ in tetragonal YSZ disappears once the structure is sufficiently doped to stabilize in the cubic phase.[33] The corresponding XRD pattern of these materials is reported in Figure 3b. The planes labeled (101), (002)/(110), (112)/(200), (103)/(211), and (202) are characteristic of tetragonal YSZ. However, due to small particle sizes and peak broadening, the diffraction patterns for cubic and tetragonal phases are indistinguishable from each other. Scherrer 1st peak analysis of the XRD pattern indicates that the crystallite size is roughly 7 nm, which is corroborated with the TEM analysis of the powder in Figure 4,

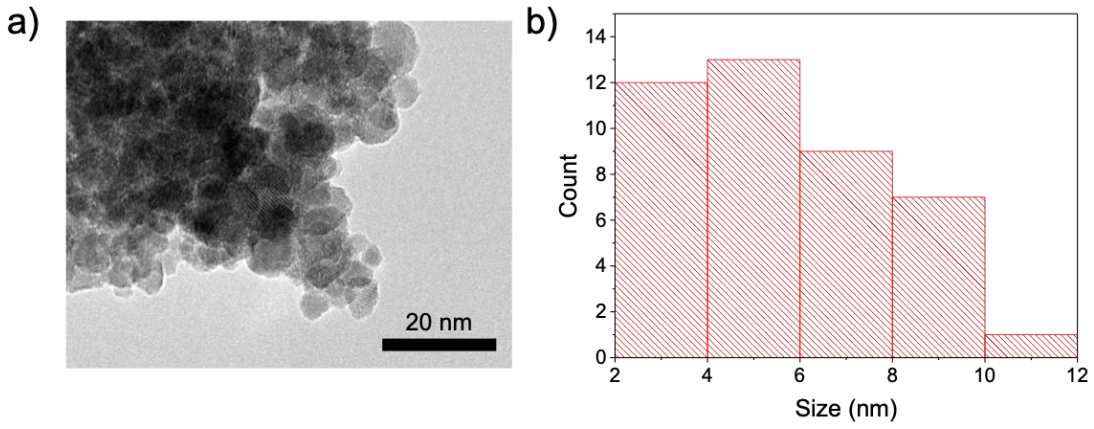


*Figure 4.4. a) TEM image of representative 8YSZ nanoparticle sample. b) The particle size distribution (n = 42) of the particles determined by TEM.*

where average particle size, morphology, crystallinity, and crystal structure may also be determined.

We tuned the composition of our materials to obtain 8YSZ and 6YSZ powder, with the goal of densifying these samples via SPS to investigate their bulk mechanical and optical properties. After the densification process, the crystal size grew to roughly 100 nm as determined by Scherrer 1$^{st}$ peak analysis of XRD spectrum. While significant grain growth occurred during the densification, this gran size is still relatively small compared to the wavelengths of the visible spectrum. After densification, the samples exhibit a dark grey color due to both some carbon in-diffusion from the graphite die and the formation of oxygen vacancies. This drastically impairs the transparency of the material (See black curve in Figure 5a). Prior investigations demonstrated that the described effects can be mitigated through the introduction of an air annealing post processing step to saturate the oxygen vacancies and reduce the levels of carbon impurities in the material.[18] Following a similar approach, we annealed our samples in air at 750°C for 19 hours. Figure 5 shows the difference in transparency before and after the described thermal process. As depicted in Figure 6, no significant variation of the Raman spectrum of sintered 8YSZ and 6YSZ samples was observed after the annealing process, indicating no discernible change in structure. This supports the hypothesis that the saturation of oxygen vacancies is the cause of the improved transparency instead of a structural effect.

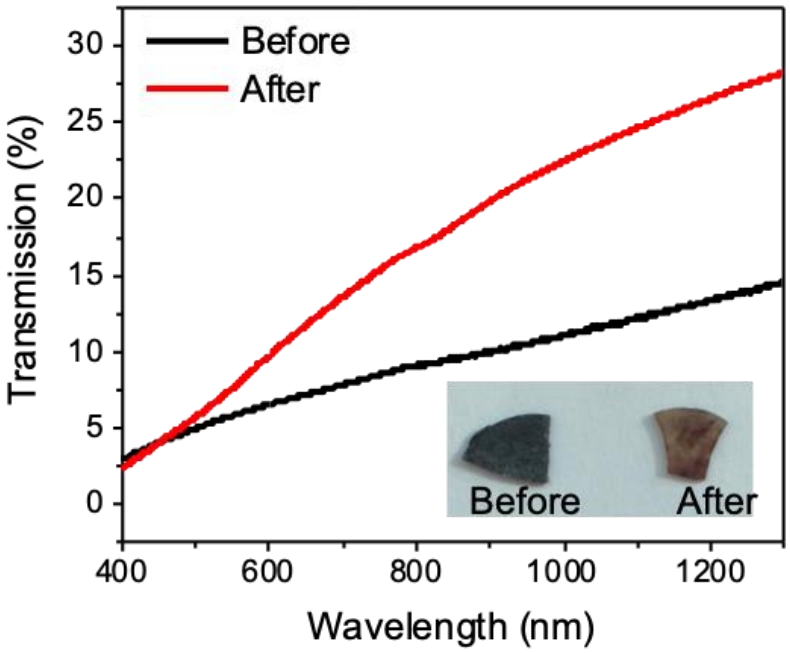


*Figure 4.5. Transmission percentage of 8YSZ sample before and after the air annealing process. Inset displays a picture of the color change during the polishing and annealing process.*

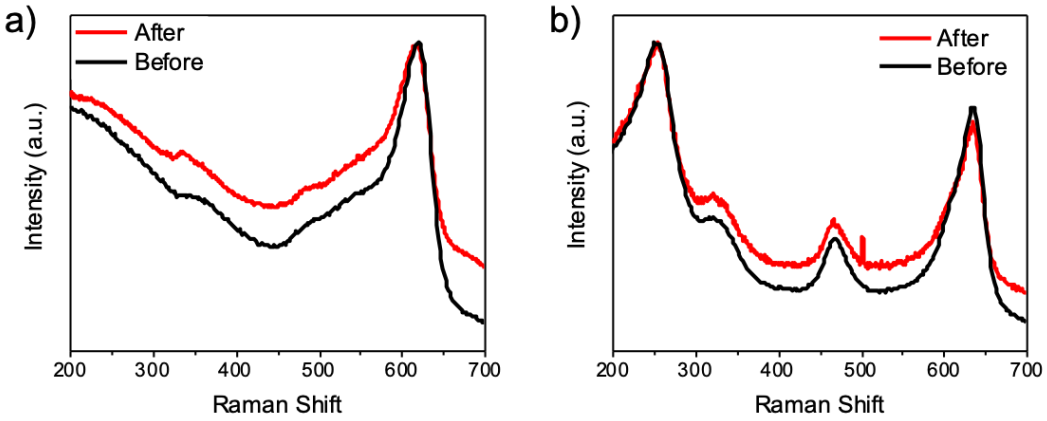


*Figure 4.6. Raman spectra of a) 8YZ and b) 6YSZ before and after the air annealing process.*

Figure 7 compares the difference in transmission percentage between the 6YSZ and 8YSZ bulk samples after annealing in air. As both the samples have a density greater than 98% dense and grain size around 100 nm, we contend that a difference in scattering from the grain boundaries and pores cannot be the differentiating factor in transparency between the two materials. The only difference among the 8YSZ and 6YSZ is represented by their structure (See Figure 6), which suggests that the difference in transparency is caused by the birefringent nature of the tetragonal domains of 6YSZ, while 8YSZ has an isotropic cubic structure. The change in orientation of tetragonal crystals causes the change in index of refraction leading to light to scatter within the bulk.[13]

We also show cross section SEM of the sintered samples for the 8YSZ and 6YSZ in Figure 8. Both samples exhibit large grains, in particular the 8YSZ samples show micron-sized grains. This is not consistent with XRD analysis, which suggests that the large grains visible in the SEM micrographs are actually polycrystalline, *i.e.*, composed of smaller crystallite domains. This difference may be an effect of the isotropic nature of the cubic structure in the 8YSZ sample. This appearance in comparison with the smaller (~500 μm) and more irregular grain pattern in the 6YSZ samples would seem to correlate with the scattering behavior inferred from Figure 7, though more data from different YSZ compositions would be required to formulate definitive conclusions.

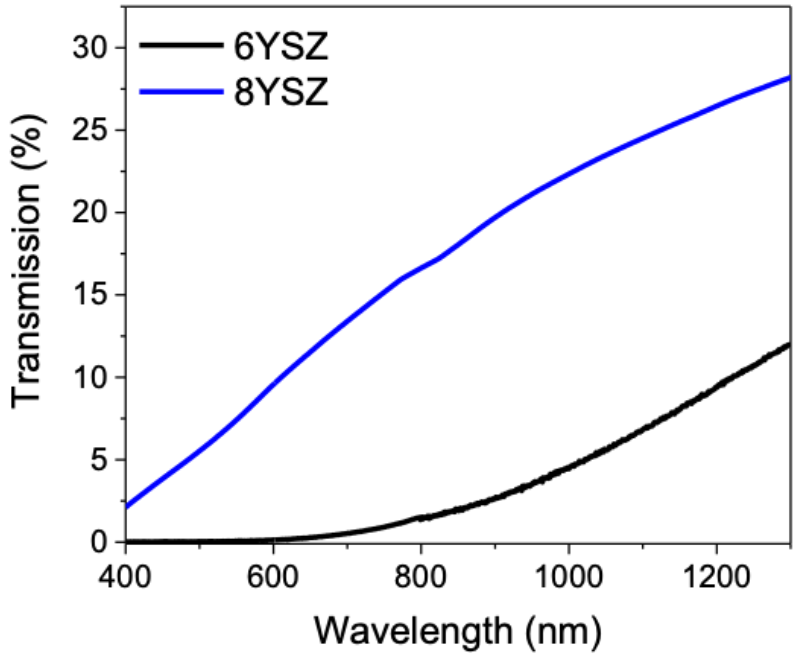


*Figure 4.7. Transmission of 8YSZ and 6YSZ after the air annealing process*

Finally, we compared the mechanical properties of 8YSZ and 6YSZ (Figure 9). Both samples have comparable hardness at 13-14 GPa while the toughness of 6YSZ is slightly higher. The hardness of YSZ materials increases significantly from undoped-zirconia to 3YSZ reaching a peak of 14 GPa and decreases only slightly from 3YSZ to 8YSZ.[34] Ghatee also measured only a small difference in the hardness of 3YSZ and 8YSZ with 12.7 and 11.8 respectively.[28] The increasing yttria content and subsequent change from tetragonal to cubic structure when moving from 3YSZ to 8YSZ does not have a large effect on the hardness but the material becomes significantly more brittle and less tough, however the isotropic cubic structure leads to increased optical transparency.

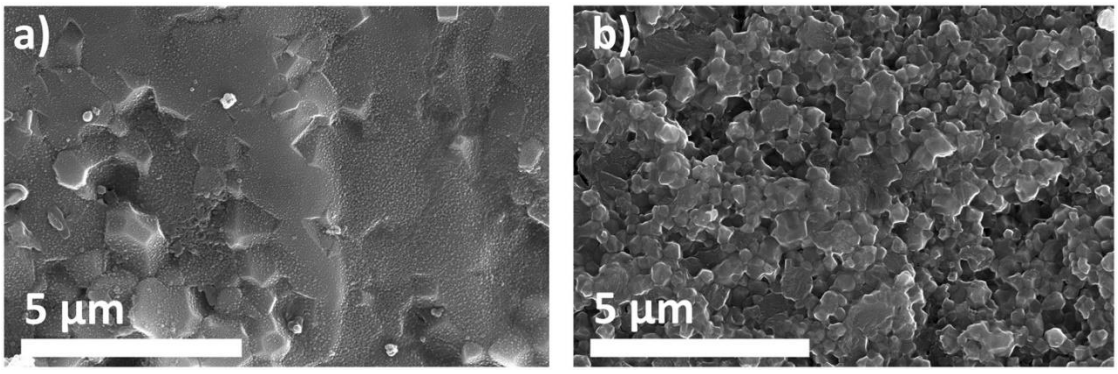


*Figure 4.8. SEM images of the cross section of a) 8YSZ and b) 6YSZ sintered samples.*

| **Composition** | **Density (%)** | **Densification T (°C)** | **Hardness (GPa)** | **Toughness (MPa $m^{-5}$)** |
|---|---|---|---|---|
| 8YSZ | 102.1% | 1200 | 13.9 ± 0.7 | 1.67 ± 0. 49 |
| 6YSZ | 98.9% | 1200 | 14.9 ± 0.9 | 2.27 ± 0.27 |

*Figure 4.9. Mechanical properties of densified 8YSZ and 6YSZ samples*

Sakuma et al. prepared a sample with 6.3 mol percentage of yttria by arc melting of yttria and zirconia together and determined the toughness was about 2.5 MPa $m^{.5}$.[34] Another study found the toughness of 5 percent molar YSZ was 3.8 MPa $m^{.5}$.[35] These values agree with our study measuring the toughness of 6YSZ to be 2.27 MPa $m^{.5}$. Although Sakuma et al. did not see much of a decrease in toughness from 6YSZ to 8YSZ, Liu et al. as well as Ghatee et al. found that the toughness of 8YSZ was comparable to our study with 1.6 MPa $m^{.5}$, 1.7 MPa $m^{.5}$ and 1.67 MPa $m^{.5}$ respectively.[28,35] Although these studies were using less than 3 percent yttria content, smaller grain sizes are another factor suggesting to a reduction in mechanical toughness of YSZ.[36–38] Lui et al. was the only study to reported grain sizes

with comparable yttria content to our 6YSZ sample finding that the grains were more than 500 nm which suggests that since our toughness values were similar, the grain size may not have as much of an effect when the yttria content is increased above 3YSZ.

### 4.4: Conclusions

Ceramics and specifically YSZ have a broad range of applications with the combination of high strength, toughness and optical transparency. In this work, we investigate the joint-optimization of the strong mechanical properties of 3YSZ with the optical transparency of 8YSZ through SPS densification of nanoparticles. We demonstrate a route for the synthesis of YSZ nanoparticles based on spray pyrolysis where we have complete control over both the composition of the particles, by tuning the precursor mix, and the size of the particles, by changing the temperature in the furnace during processing. This control over particle composition and size is unavailable commercially and further investigations could leverage this ability to study the bulk nanostructured properties obtained.

The produced powder is densified via SPS where we deconvolve the effect of oxygen vacancies and separately the crystal structure on the transparency of the densified samples. We found the 8YSZ and 6YSZ samples to have the same porosity and same crystallite sizes, hence we conclude that the difference in optical properties was due to a difference in crystal structure and the birefringent nature of tetragonal crystals in 6YSZ.

This investigation confirmed that as yttria content increases, specifically comparing 6YSZ with 8YSZ, there was not a major loss of hardness. However, 8YSZ was less tough and much more brittle than 6YSZ. Further investigations should continue to investigate an

optimum balance between the desired optical properties of 8YSZ and the stronger mechanical properties of 3YSZ and 6YSZ to improve upon the possible applications of YSZ.

## 4.5: References


(1) Damestani, Y.; Reynolds, C. L.; Szu, J.; Hsu, M. S.; Kodera, Y.; Binder, D. K.; Park, B. H.; Garay, J. E.; Rao, M. P.; Aguilar, G. Transparent Nanocrystalline Yttria-Stabilized-Zirconia Calvarium Prosthesis. *Nanomedicine Nanotechnology, Biol. Med.* **2013**, *9* (8), 1135–1138. https://doi.org/10.1016/j.nano.2013.08.002.

(2) Zhang, Y. Making Yttria-Stabilized Tetragonal Zirconia Translucent. *Dent. Mater.* **2014**, *30* (10), 1195–1203. https://doi.org/10.1016/j.dental.2014.08.375.

(3) Cao, X. Q.; Vassen, R.; Stoever, D. Ceramic Materials for Thermal Barrier Coatings. **2004**, *24*, 1–10. https://doi.org/10.1016/S0955-2219(03)00129-8.

(4) Etsell, T. H.; Flengas, S. N. The Electrical Properties of Solid Oxide Electrolytes. **1994**, 143–172.

(5) Garvie, R. C.; Hannink, R. H.; Pascoe, R. T. Ceramic Steel? *Nature* **1975**, *258* (5537), 703–704. https://doi.org/10.1038/258703a0.

(6) Basu, B. Toughening of Yttria-Stabilised Tetragonal Zirconia Ceramics. *Int. Mater. Rev.* **2005**, *50* (4), 239–256. https://doi.org/10.1179/174328005X41113.

(7) Ilavsky, J.; Stalick, J. K. Phase Composition and Its Changes during Annealing of Plasma-Sprayed YSZ. *Surf. Coatings Technol.* **2000**, *127* (2–3), 120–129. https://doi.org/10.1016/S0257-8972(00)00562-4.

(8) Shukla, S.; Seal, S. Mechanisms of Room Temperature Metastable Tetragonal Phase Stabilisation in Zirconia. *Int. Mater. Rev.* **2005**, *50* (1), 45–64. https://doi.org/10.1179/174328005x14267.

(9) Hannink, R. H. J.; Kelly, P. M.; Muddle, B. C. Transformation Toughening in Zirconia-Containing Ceramics. *J. Am. Ceram. Soc.* **2004**, *83* (3), 461–487. https://doi.org/10.1111/j.1151-2916.2000.tb01221.x.

(10) Kelly, P. M.; Rose, L. R. F. The Martensitic Transformation in Ceramics - Its Role in Transformation Toughening. *Prog. Mater. Sci.* **2002**, *47* (5), 463–557. https://doi.org/10.1016/S0079-6425(00)00005-0.

(11) Lange, F. F. Transformation Toughening. *J. Mater. Sci.* **1982**, *17*, 225–234.

(12) Anselmi-Tamburini, U.; Woolman, J. N.; Munir, Z. A. Transparent Nanometric Cubic and Tetragonal Zirconia Obtained by High-Pressure Pulsed Electric Current Sintering. *Adv. Funct. Mater.* **2007**, *17* (16), 3267–3273. https://doi.org/10.1002/adfm.200600959.

(13) Klimke, J.; Trunec, M.; Krell, A. Transparent Tetragonal Yttria-Stabilized Zirconia Ceramics: Influence of Scattering Caused by Birefringence. *J. Am. Ceram. Soc.* **2011**, *94* (6), 1850–1858. https://doi.org/10.1111/j.1551-2916.2010.04322.x.

(14) Krell, A.; Hutzler, T.; Klimke, J. Transmission Physics and Consequences for Materials Selection, Manufacturing, and Applications. *J. Eur. Ceram. Soc.* **2009**, *29* (2), 207–221. https://doi.org/10.1016/j.jeurceramsoc.2008.03.025.

(15) Wang, S. F.; Zhang, J.; Luo, D. W.; Gu, F.; Tang, D. Y.; Dong, Z. L.; Tan, G. E. B.; Que, W. X.; Zhang, T. S.; Li, S.; Kong, L. B. Transparent Ceramics : Processing , Materials and Applications. *Prog. Solid State Chem.* **2013**, *41*, 20–54.

(16) Zhang, H.; Kim, B. N.; Morita, K.; Yoshida, H.; Lim, J. H.; Hiraga, K. Optical Properties and Microstructure of Nanocrystalline Cubic Zirconia Prepared by High-Pressure Spark Plasma Sintering. *J. Am. Ceram. Soc.* **2011**, *94* (9), 2981–2986. https://doi.org/10.1111/j.1551-2916.2011.04477.x.

(17) Kodera, Y.; Hardin, C. L.; Garay, J. E. Transmitting, Emitting and Controlling Light: Processing of Transparent Ceramics Using Current-Activated Pressure-Assisted Densification. *Scr. Mater.* **2013**, *69* (2), 149–154. https://doi.org/10.1016/j.scriptamat.2013.02.013.

(18) Alaniz, J. E.; Perez-Gutierrez, F. G.; Aguilar, G.; Garay, J. E. Optical Properties of Transparent Nanocrystalline Yttria Stabilized Zirconia. *Opt. Mater. (Amst).* **2009**, *32* (1), 62–68. https://doi.org/10.1016/j.optmat.2009.06.004.

(19) Hotza, D.; García, D. E.; Castro, R. H. R. Obtaining Highly Dense YSZ Nanoceramics by Pressureless, Unassisted Sintering. *Int. Mater. Rev.* **2015**, *60* (7), 353–375. https://doi.org/10.1179/1743280415Y.0000000005.

(20) Bokov, A.; Zhang, S.; Feng, L.; Dillon, S. J.; Faller, R.; Castro, R. H. R. Energetic Design of Grain Boundary Networks for Toughening of Nanocrystalline Oxides. *Journal of the European Ceramic Society*. 2018, pp 4260–4267. https://doi.org/10.1016/j.jeurceramsoc.2018.05.007.

(21) Casolco, S. R.; Xu, J.; Garay, J. E. Transparent/Translucent Polycrystalline Nanostructured Yttria Stabilized Zirconia with Varying Colors. *Scr. Mater.* **2008**, *58* (6), 516–519. https://doi.org/10.1016/j.scriptamat.2007.11.014.

(22) Garay, J. E. Current-Activated, Pressure-Assisted Densification of Materials. *Annu. Rev. Mater. Res.* **2010**, *40* (1), 445–468. https://doi.org/10.1146/annurev-matsci-070909-104433.

(23) Davoodzadeh, N.; Aguilar, G.; Jonak, C.; Binder, D. K.; Cuando, N.; Aminfar, A. H.; Halaney, D. L. Laser Speckle Imaging of Brain Blood Flow through a

Transparent Nanocrystalline Yttria-Stabilized-Zirconia Cranial Implant. **2018**, *1049303* (February 2018), 2. https://doi.org/10.1117/12.2285953.

(24) Gutierrez, M. I.; Penilla, E. H.; Leija, L.; Vera, A.; Garay, J. E.; Aguilar, G. Novel Cranial Implants of Yttria-Stabilized Zirconia as Acoustic Windows for Ultrasonic Brain Therapy. *Adv. Healthc. Mater.* **2017**, *6* (21), 1–11. https://doi.org/10.1002/adhm.201700214.

(25) Messing, G. L.; Zhang, S.-C.; Jayanthi, G. V. *Ceramic Powder Synthesis by Spray Pyrolysis*; 1993.

(26) Liu, C.; Xiang, M.; Fu, Z.; Shen, Z.; Xiong, Y. Microstructural Refinement in Spark Plasma Sintering 3Y-TZP Nanoceramics. *J. Eur. Ceram. Soc.* **2016**, *36* (10), 2565–2571. https://doi.org/10.1016/j.jeurceramsoc.2016.03.019.

(27) Cottom, B. A.; Mayo, M. J. FRACTURE TOUGHNESS OF NANOCRYSTALLINE ZrO , - 3mol % Y , 03 DETERMINED BY VICKERS INDENTATION. **1996**, *34* (5), 809–814.

(28) Ghatee, M.; Shariat, M. H.; Irvine, J. T. S. Investigation of Electrical and Mechanical Properties of 3YSZ/8YSZ Composite Electrolytes. *Solid State Ionics* **2009**, *180* (1), 57–62. https://doi.org/10.1016/j.ssi.2008.10.006.

(29) Ghosh, S.; Teweldebrhan, D.; Morales, J. R.; Garay, J. E.; Balandin, A. A. Thermal Properties of the Optically Transparent Pore-Free Nanostructured Yttria- Stabilized Zirconia. **2012**, *113507* (October 2009). https://doi.org/10.1063/1.3264613.

(30) INGEL, R. P.; Lewis III, D. Lattice Parameters and Density for Y2O3-Stabilized ZrO2. *J. Am. Ceram. Soc.* **1986**, *69* (4), 325–332. https://doi.org/10.1111/j.1151-2916.1986.tb04741.x.

(31) Anstis, G. R. A Critical Evaluation of Indentation Techniues for Measuring Fracture Toughness: I, Direct Crack Measurements. **1981**, *46* (September), 533–538.

(32) Hemberger, Y.; Wichtner, N.; Berthold, C.; Nickel, K. G. Quantification of Yttria in Stabilized Zirconia by Raman Spectroscopy. *Int. J. Appl. Ceram. Technol.* **2016**, *13* (1), 116–124. https://doi.org/10.1111/ijac.12434.

(33) Yashima, M.; Ohtake, K.; Kakihana, M.; Arashi, H.; Yoshimura, M. Determination of Tetragonal-Cubic Phase Boundary of Zr(1-x)R(x)O(2-x/2) (R=Nd,Sm,Y,Er and Yb) by Raman Scattering. *J. Phys. Chem. Solids* **1996**, *57* (I), 17–24. https://doi.org/10.1016/0022-3697(95)00085-2.

(34) Sakuma, T.; Yoshizawa, Y. I.; Suto, H. The Microstructure and Mechanical Properties of Yttria-Stabilized Zirconia Prepared by Arc-Melting. *J. Mater. Sci.*

**1985**, *20* (7), 2399–2407. https://doi.org/10.1007/BF00556069.

(35) Liu, H.; Zhao, W.; Ji, Y.; Cui, J.; Chu, Y.; Rao, P. Determination of Fracture Toughness of Zirconia Ceramics with Different Yttria Concentrations by SEVNB Method. *Ceram. Int.* **2017**, *43* (13), 10572–10575. https://doi.org/10.1016/j.ceramint.2017.04.064.

(36) Swain, M. V. Grain-Size Dependence of Toughness and Transformability of 2 Tool % Y-TZP Ceramics. **1986**, *5*, 2–5.

(37) Becher, P. F.; Swain, M. V. Grain-Size-Dependent Transformation Behavior in Polycrystalline Tetragonal Zirconia. *J. Am. Ceram. Soc.* **1992**, *502*, 493–502.

(38) Bravo-Leon, A.; Morikawa, Y.; Kawahara, M.; Mayo, M. J. Fracture Toughness of Nanocrystalline Tetragonal Zirconia with Low Yttria Content. *Acta Mater.* **2002**, *50* (18), 4555–4562. https://doi.org/10.1016/S1359-6454(02)00283-5.

# Chapter 5: Nanocrystalline Yttria-Stabilized Zirconia for Cranial Widow Applications

## 5.1: Introduction

Brain disorders such as Alzheimer's, Parkinson's, tumors and traumatic brain injuries (TBI) are steadily increasing in recent years[1] which with increased optical access to the brain could be monitored for diagnostics and treatment. Motivated by advances in light-based therapies,[2] increased optical access of the brain opens new possibilities for treatments. For light to pass through biological tissues with minimal damage to optical probing inside the body the wavelengths of light must be within Near Infrared (NIR) biological window. There are three NIR biological windows of wavelengths between 800-1700 nm with NIR-I, NIR-2, and NIR-3 ranging from 800-1000 nm, 1000-1400, and 1500-1700 nm respectively. The NIR windows allow light to enter the body for both diagnostic and treatment.[2] Examples include photodynamic therapy which is used for acne[3] but also brain cancer[4] as well as photobiomodulation which uses low power lasers to treat traumatic brain injuries.[5] Although these therapies have shown success, the lack of transparency of scalp and skull tissues limits the possibilities of light treatments and diagnoses for brain diseases which currently require thinning or opening a hole in the skull for each treatment repeating the trauma. A window to the brain with the right material properties would solve this problem and motivates the research.

Materials such as polydimethylsiloxane (PDMS)[6], glass, and nanocrystalline yttria-stabilized zirconia (YSZ) have been researched as to address the lack of optical access from the skull and skin tissues.[7] To replace part of the skull with a transparent material, the

material must maximize its optical transparency, and biocompatibility, as well as having strong mechanical properties to protect the brain from further damage and trauma. PDMS lacks the mechanical properties to protect the brain with a compressive modulus up to 5 times less than that of a human skull.[8,9] Glass has great transparency but mechanically too brittle to protect the brain. Even the improved mechanical properties of Pyrex glass were too brittle for safe cranial window applications.

YSZ ceramics looks to be optimize the mechanical toughness, optical transparency, as well as the biocompatibility necessary to replace part of the skull and provide a window to the brain. A number of studies have investigated YSZ ceramics and found excellent mechanical and optical properties such as Sakume et al. and Anselmi-Tamburini et al.[10,11] Depending on the concentration of $Y_2O_3$ between 3-8 mol%, the hardness was determined to be 13-15 GPa with a fracture toughness of 7-12 MPa $m^{1/2}$.[10] The optical properties engineered by Anselmi-Tamburini et al. to reach 60% transparency at 1000 nm, within the biological window, and close to the theoretical single crystal transparency limit of 75%.[11] YSZ has passed biocompatibility test before as it is used in dental implants[12] and hip replacement prosthesis[13]. For example, similar cell densities to the cells-only control group were reported by Shih-Fu Ou et al. in direct culture experiments.[14] Additionally, zirconia implants into the femurs of Sprague-Dawley rats outperformed the titanium ones showing stronger mineralized bone-to-implant interfaces.[15]

YSZ nanoparticles change their crystal structure from monoclinic with a small amount added to $ZrO_2$, roughly 0-3 mol% $Y_2O_3$, and tetragonal to cubic as the $Y_2O_3$ concentration increases from 3-8 mol %. YSZ in the monoclinic phase has the best mechanical properties

due to its transition toughness[16] but is not transparent while YSZ in the cubic phase is optically transparent but too brittle. Optimizing the optical with the mechanical properties is necessary for the application of using YSZ as a cranial window.

In this work, YSZ with 3-8 mol % yttria concentrations are compared using different densification methods and evaluated for in vitro cytocompatibility. Commercial YSZ nanoparticles with 3, 6, 8 mol % concentrations were processed and densified into discs using current activated pressure-assisted densification (CAPAD) and compared with spark plasma sintered (SPS) of house aerosol spray pyrolysis-synthesized YSZ with 4 and 8 mol % YSZ. The polished and unpolished YSZ discs were investigated for their microstructures, surface morphologies and hydrophilicity as well as the in vitro cytocompatibility in terms of cell spreading area, cell aspect ratio, and cell adhesion density. To account for possible effects of ions released from the YSZ on cell responses, pH values and $Zr^{4+}$ and $Y^{3+}$ concentrations are measured. To the best of our knowledge this work is the first study determining the cytocompatibility of these discs with BMSCs in terms of different composition, synthesis methods, densification processing and microstructure of the YSZ discs. As to date YSZ discs as cranial windows has not been extensively studied, this work is necessary to build the foundation for future preclinical and clinical translation.

## 5.2: Experimental Methods

### *5.2.1: YSZ Discs*

YSZ powder synthesized in the lab was compared with commercial nanopowders purchased from Toshoh USA Inc. The YSZ powder synthesized in house used an aerosol

spray pyrolysis system described in a previous paper.[17] In summary, the anhydrous $ZrCl_4$ (Alfa Aesar) and $YCL_3 \cdot 6H_2O$ (Sigma-Aldrich) was sonicated in deionized (DI) water. Argon flowing at 7000 standard cubic centimeters per min (sccm) aerosolized the solution through a nebulizer (BGI/Mesa Laboratories). The aerosolized droplets are then carried through a 2-inch diameter tube furnace (MTI OTF-1200x) set to 900 ℃. By varying the ratio of $ZrCl_4$:$YCl_3$, specific $Y_2O_3$ content in the YSZ nanoparticles is obtained. For this study 8% mol YSZ and 4% mol YSZ were used. After synthesis, the particles are rinsed with DI water and centrifuged at 3400 revolutions per min (rpm) for 10 minutes repeated 3 times to remove any contaminants. The powder was then dried on a hot plate and then annealed in air at 650 ℃ for 3 hours to remove any oxygen vacancies in the nanostructures. The in-house synthesized nanopowders were densified using a similar process as a previous paper.[17] Before densifying, the powder is ball milled for 48 hours at 60 rpm. After breaking up large agglomerates in the ball mill, .5 g of powder is placed into a 10 mm graphite die and punch setup for Spark Plasma Sintering (SPS, Fuji SPS, Dr. Sinter Lab Jr.). The densification process was completed under vacuum. The pressure is set to 100 MPa before any current is applied. The sample is then heated to 1100 ℃ at a rate of 200 ℃/min and then to a final temperature of 1200 ℃ at 50 ℃/min. Finally, the temperature is held at 1200 ℃ for 10 min. The temperature is measured throughout the process using an external pyrometer.

Commercial YSZ powder purchased from Toshoh USA Inc was used for comparison. The nanocrystalline YSZ contained 3, 6, and 8 % mol $Y_2O_3$ respectively and densified using a current-activated pressure-assisted densification (CAPAD) process described in an earlier

paper.[18] 1.5 g of commercial YSZ powder was placed into a 19 mm graphite die and placed in the CAPAD apparatus. Graphite spacers and copper electrode secure the die in the chamber at a pressure of $1 \times 10^{-3}$ Torr. The pressure on the graphite die was set to 106 MPa and applied on the sample for 2 min before any current is applied. Then, the sample is heated at a rate of 160 ℃/min until the temperature reaches 1200 ℃. Once the temperature reaches 1200 ℃, the pressure on the die is steadily increased to 141 MPa and held at that temperature and pressure for 10 min.

After obtaining densified samples, the samples are polished both to remove any carbon contaminants from the densification process as well to remove surface roughness to increase the transparency. The disks were polished using an automatic polisher (Pace technologies) and diamond slurry. Starting with a diamond slurry with a size of 30 μm and progressing down to 1 μm colloidal silica slurry the discs increased transparency. Polished YSZ discs densified with SPS using in house made YSZ nanoparticles are labeled as 4YSZ_P and 8YSZ_P respectively while the rough surfaces are referred to as 4YSZ_PR and 8YSZ_PR. The commercial powdered densified using CAPAD are called 3YSZ, 6YSZ, and 8YSZ when they are polished and 3YSZ_R, 6YSZ_R, and 8YSZ_R respectively when they are still rough.

*5.2.2: Transparency of YSZ disks*

The transparency of the YSZ discs was quantified using a spectrophotometer (Infinite M200 Pro, Tecan) where the disks were placed in a 96-well plate (Falcon, USA). The absorbance was measured at wavelengths between 300-900 nm and converted into a percentage of transmission using Beer's Law in eqn. 1:

$$A = 2 - log_{10}(\%T) \qquad (5.1)$$

Where A is the absorbance and %T is the percentage of transmission.

In addition to measuring the transparency, a polished 8YSZ disk densified with CAPAD from commercial powder with a thickness of .48 mm is shown placed on a piece of paper with the writing, “Transparent nc-YSZ” to demonstrate the transparency.

*5.2.3: YSZ Disc Microstructure Characterization*

The cross section of the discs and microstructure was analyzed with scanning electronic microscopy (SEM). YSZ discs were first cut in half and then placed in a sample holder at 90° under the SEM. Due to the low conductivity of YSZ, the samples were sputtering (model 108, Cressington Scientific Instruments Ltd., Watford, U.K.) with platinum/palladium with 20 mA for 60s to increase to improve the imaging. Images were taken using an SEM (Nova NanoSEM 450, FEI Co.) and analyzed using *ImageJ* software to determine the diameters of polycrystalline grains and nanoscale domains.

*5.2.4: Water contact angle with YSZ discs*

A goniometer (model G16, Wet Scientific) was used to measure the water contact angles of both polished and unpolished YSZ discs. A 10 μL droplet was placed on the surface of the discs and the water contact angle was calculated from the measurement at five different areas of triplicate samples.

*5.2.5: Harvest and Culture BMSCs*

The protocol followed was approved by the Institutional Animal Care and Use Committee (IACUC) at University of California Riverside. To summarize the cultured and harvested rat BMSCs that is similar to a previous work,[19] after removing the distal and proximal ends

of the femoral and tibial bones, the bone marrow was flushed out of the bones with a syringe by Dulbecco's modified Eagle's medium (DMEM, #SLBC9050, high glucose, D5648, Sigma-Aldrich) and mixed with 10% fetal bovine serum (FBS, HyClone, #SH30910, Thermo Fisher Scientific Inc.), 1% penicillin/streptomycin (P/S, HyClone, #SV30010, Thermo Fisher Scientific Inc.) before getting placed in a centrifuge tube. The mixture of DMEM with 10% FBS and 1% P/S is the cultured media in this study. Standard cell culture conditions were used (37℃, 5%/95% CO2/Air, humidified and sterile environment) to 90-95% confluency after filtering the cells with a 70 μm nylon strainer (Fisher Scientific).

*5.2.6: BMSC Culture with YSZ Discs and Controls*

To compare the discs made from commercial powder and densified with CAPAD process with the discs made in house, the volume was controlled between the samples. The CAPAD discs were cut into quarters to ensure similar volume of the discs. Both discs, polished and rough, as well as both powders, commercial and synthesized, were used in this study. Titanium, the most commonly used bio implant material since it is bioiner, was used as a control to compare the YSZ nanoparticles as well as glass slides for reference of standard cell cultures. Before the study, glass slides, in addition to the discs made of YSZ and titanium were all sterilized and heated in an oven at 160℃ for 30 min. To test the unlikely possibility of YSZ discs degrading and releasing nanparticles in vivo, the nanoparticles are tested as well. The concentration of YSZ particles was 10 mM which is not expected to have much of an effect on cell viability and adhesion density as reported previously.[20] YSZ

discs are not expected to release any nanoparticles during the BMSC studies as they are considered bioinert.

Direct culture method described in a previous publication[19] determinations the cytocompatibility of YSZ discs. In summary, 12-well tissue culture-treated plates are rinsed with 2 ml of PBS and DMEM respectively to standardize the osmotic pressure under sterile conditions. After sterilization, BMSCs (P2) are planted onto the surface with a density of 10,000 cells/cm$^2$ and gestated in 3 mL of DMEM under standard cell culture conditions for 24 hours. The positive control had BMSCs cultured with only DMEM in the wells alone. The negative control of DMEM without any cells was also tested.


*Figure 5.1. Schematics of A) Direct culture of bone marrow-derived mesenchymal stem cells (BMSCs) with YSZ discs. B) the BMSCs under direct and indirect contact conditions*

### *5.2.7: Characterize the BMSC Adhesion and Morphology*

The culture with the BMSCs attached on the samples was secured with 4% formaldehyde (10% neutral buffered formalin; VWR) for 20 min, then stained with Alexa Flour 488-phalloidin (A12379, Life Technologies) for 20 min and finally 4',6-diamindino-2-

phenylindole dilactate (DAPI, Invitrogen) for nuclei for 10 min. Both the BMSC directly in contact with the sample in addition to the ones in indirect contact attached to the well plate around each sample were imaged using a fluorescence microscope (Eclipse Ti and NIS software, Nikon).

10 random spots were used and analyzed using ImageJ software to determine quantitatively the cell spreading area, aspect ratio and the number of cells per unit area. The cell adhesion density was calculated by counting the number of cells divided by the image area (cells/$cm^2$).

*5.2.8: pH of the Post Culture Media*

Both the pH value, the $Zr^{4+}$ and $Y^{3+}$ concentrations were measured right after collection. The pH meter (Symphony, model SB70P, VWR) was purchased calibrated. Inductively coupled plasma optical emission spectrometry (ICP-OES; Optima 8000, PerkinElmer) determined the concentrations of $Zr^{4+}$ and $Y^{3+}$. Ionic concentrations were calculated taking into account the 1:10 DI water diluted solutions to minimized matrix effects in ICP-OES.

*5.2.9: Mineral Deposition of the YSZ Discs*

All polished YSZ samples were characterized with X-ray diffraction (XRD, Empyrean PANalytica) to determine if there was any mineral deposition during the 24-hour cell culture. *HighScore* software (PANalytical) was used to determine the crystal phases present in the sample.

*5.2.10: Statistical Analysis*

When the data set fulfilled the parametric criteria that normality is greater than .05 from the experiments run in triplicates, the numerical data was examined using a one-way

analysis of variance (ANOVA) followed by a Tukey test. The data sets that were determined to be statistically significant if $p < 0.05$ for the Tukey test. For the nonparametric data where the normality was greater than .05, Kruskal-Wallis analysis followed by a Dunn test and adjusted by Hochberg's method was used. Statistical significance was considered for the Dunn test to be $p < .0025$.

## 5.3: Results and Discussion

### *5.3.1: Optical and Mechanical Investigation YSZ Discs*

A chosen cranial window material must optimize the mechanical, optical, and biocompatible properties. A window without strong mechanical properties will not be able to provide protection for brain tissues so it cannot be too brittle or too soft. Obtaining the desired mechanical properties without the optical and biocompatiblity necessary, there would not possibility for treatments and diagnostics in addition to being dangerous to implant the window. The optical window must be available to perform further treatments without introducing new traumas by reopening the skull. If the material is not biocompatible, then it will be prone to adverse side effects such as tissue necrosis, inflammation and infections.

First investigating the optical properties, Figure 2 displays the transparency of polished 8YSZ disc samples that had a thickness of .48 mm with the light source above the sample in a and below in b. The lettering on the paper reads "Transparent nc-YSZ". The wording is clear in both cases through the transparent 8YSZ discs. Figure 2c shows the transmission of light with wavelengths from 300-900 nm. The transmission increases from only .4% to

38% as the wavelength enters the first NIR biological window. The sample tested in 2c is a polished 8YSZ disc with a thickness of .66 mm.

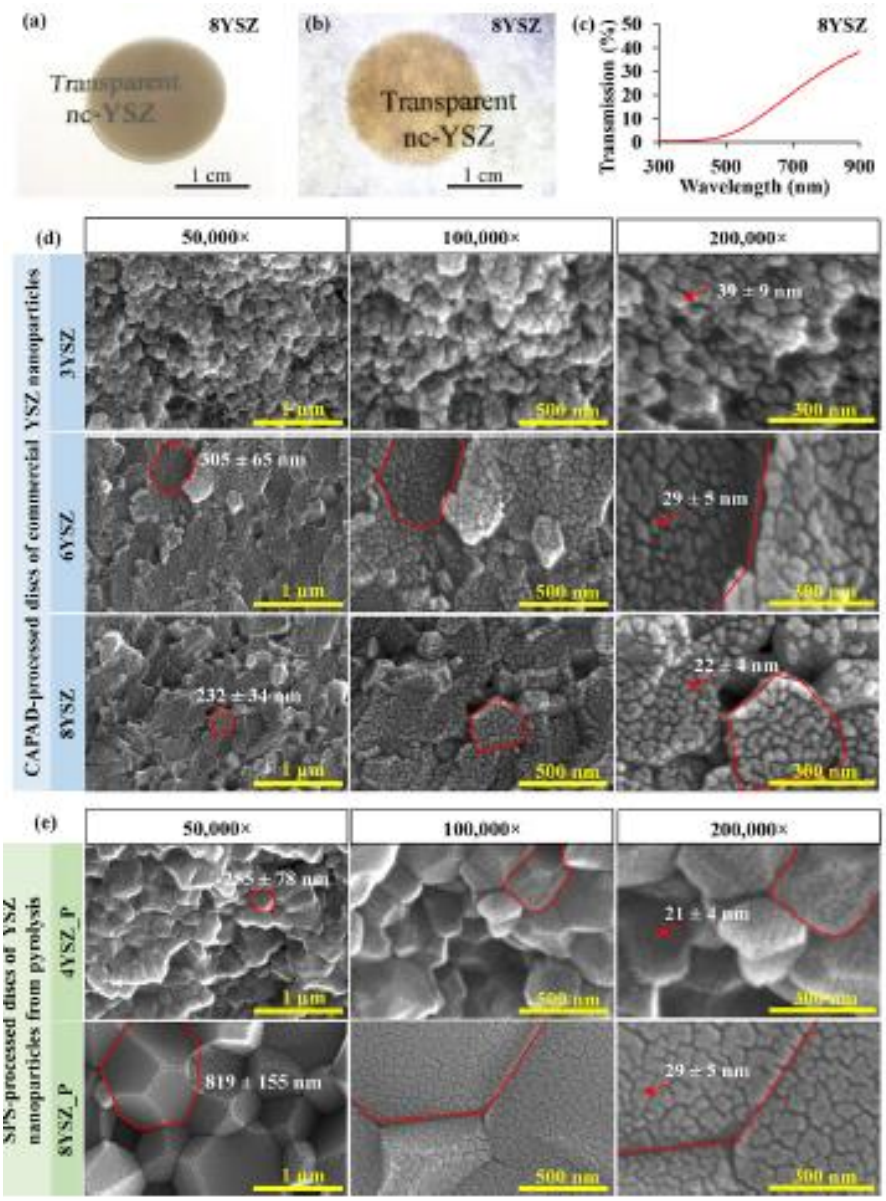


*Figure 5.2. Photographs displaying written words through the transparent YSZ disc with the light source above (A) and below (B). C) Displays the optical transmission through the same YSZ disc with wavelengths between 300-900 nm. SEM images display the microstructures.*

The lowest energy configuration for the crystal structure of YSZ is monoclinic and increasing amounts of $Y_2O_3$ will change the structure to tetragonal and finally to the cubic structure increasing its transparency.[21] The cubic structure is the best for optical properties due to its similar index off refraction in every direction although it is the most brittle YSZ crystal structure.[22] Transparency for ceramic materials is highly depended on the crystal structure as well as the size of the grains.[23]

The grain size is an important factor in making a ceramic transparent as Alaniz et al confirmed.[18] They compared the transmission of light in the wavelength range 450-850 nm on YSZ discs that had different grain sizes from varying the sintering times. Their results show that the shorter the sintering time the grains will be smaller and have better transparency.[18] To maximize the transparency of YSZ windows and that of other ceramic nanostructured materials, a grain size of less than 100 nm is optimal.[24] Figure 2 shows how the YSZ discs with higher yttria concentrations had small crystallite domains and polycrystalline grains which improved the transparency when compared with the discs with lower yttria content.

The microstructures of the YSZ discs are next examined with SEM analysis. Figure 2d, e displays a grid of the cross sections of YSZ discs containing the different $Y_2O_3$ concentrations studied. The magnification went from 50,000x to 100,000x and finally to 200,000x to show both the larger polycrystalline grains with the red outlines as well as crystalline domains on the order of a few tens of nanometers.

To find a good material for a particular application, it is important to consider the performance, property, structure and processing of that material. The progress YSZ shows

in the transparency and mechanical properties of figure 2 is due to the dense microstructures with few pores that resulted from the densification process. The 6YSZ and 8YSZ discs showed transgranular fractures from the SEM images of the cross section which typically are a result of multiple dislocations in the crystal grains.[25] On the other hand, 4YSZ_P and 8YSZ_P had intergranular fractures which occur more often since the grain boundaries are the weaker areas of the material. Previous studies indicated that there was limited difference on the mechanical properties when processing YSZ with CAPAD or SPS. The CAPAD processed 8YSZ disc had a hardness of 13.2 ± .1 GPa[26] which was comparable to the SPS processed 8YSZ_P of 13.9 ± .7 GPa.[17]

3YSZ commercial nanopowders densified with CAPAD had nanoscale crystalline grains of about 39 ± 9 nm while the 6YSZ and 8YSZ discs had grain sizes much larger with polycrystals between 200-350 nm again highlighted with red boundaries. The smaller crystallite domains inside the larger grains were between 20-30 nm.

In house pyrolysis-synthesized nanoparticles densified with SPS obtained polycrystalline grains of 255 ± 78 nm and 21 ± 4 nm for the crystalline domains for the 4YSZ_P sample. The 8YSZ_P sample had larger polycrystalline grains with 819 ± 155 nm and 29 ± 5 nm crystalline domains. It is worth noting that the densified samples using commercial powder showed transgranular fractures on their cross sections while the house synthesized and densified samples had intergranular fractures in the SEM.

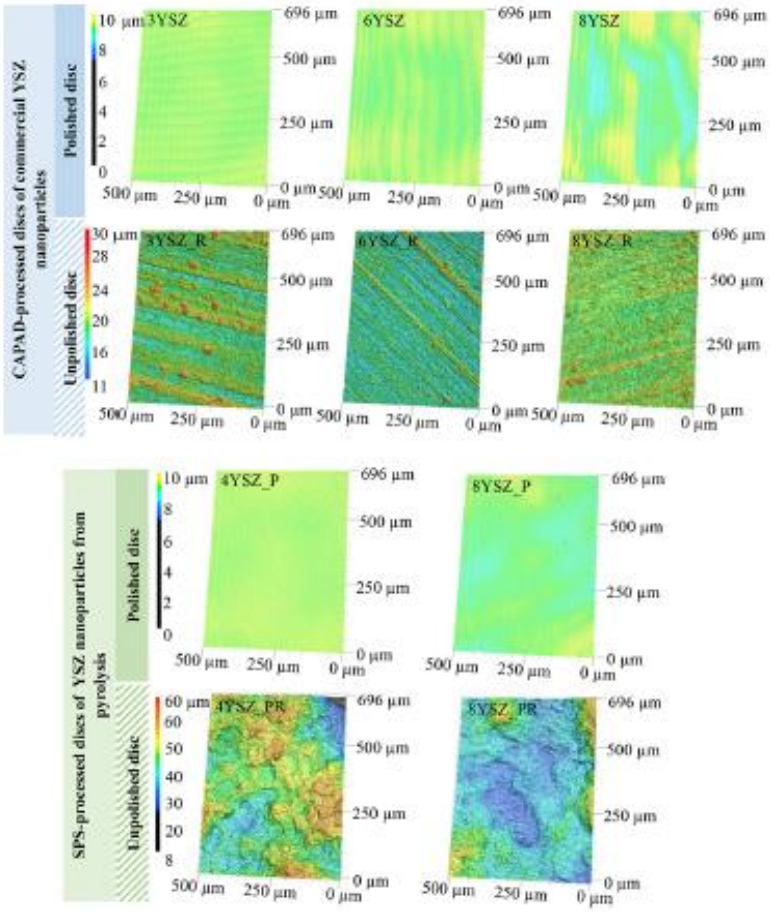


*Figure 5.3. Surface morphologies displayed from 3D microscopic images before and after polishing.*

### *5.1.2: Biocompatibility of YSZ Discs*

After evaluating the mechanical and optical properties of the YSZ discs, the next factor is determining their biocompatibility. We used the direct culture method with BMSCs to compare the in vitro cytocompatibility between CAPAD processed and SPS processed discs. The direct culture method places the cells on YSZ discs with different compositions, microstructure, grain size, surface roughness, topography and hydrophilicity. This method simulates the in vivo conditions between newly seeded implants and the surrounding cells.

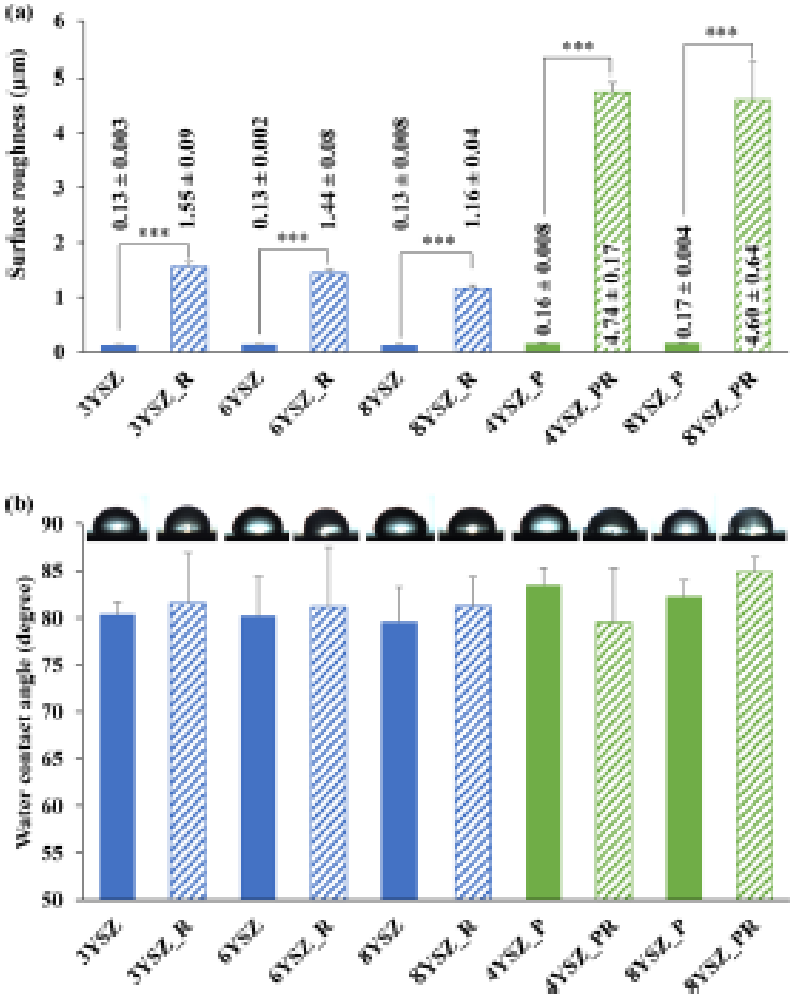


*Figure 5.4. (a) 3D laser scanning microscopy to quantify the Surface roughness (Sq) of YSZ discs. (b) Photographs of water droplets and contact angles of YSZ discs before and after polishing. Data shown as a mean ± standard deviation (n = 3); *p < 0.05, **p < 0.01*

The surface topographies of polished and unpolished YSZ discs are investigated with 3D microscopic images in Figure 3. The SPS process YSZ with synthesized nanoparticles had a rougher surface before polishing than the CAPAD densified commercial powders. Figure 4a shows measurements of the root mean squared of the height, to quantify the surface roughness (Sq) for image area is shown in Figure 4a. It is clear from the images that the

roughness of the samples was greatly decreased due to the polishing. The commercial particles densified with CAPAD had slight less surface roughness.

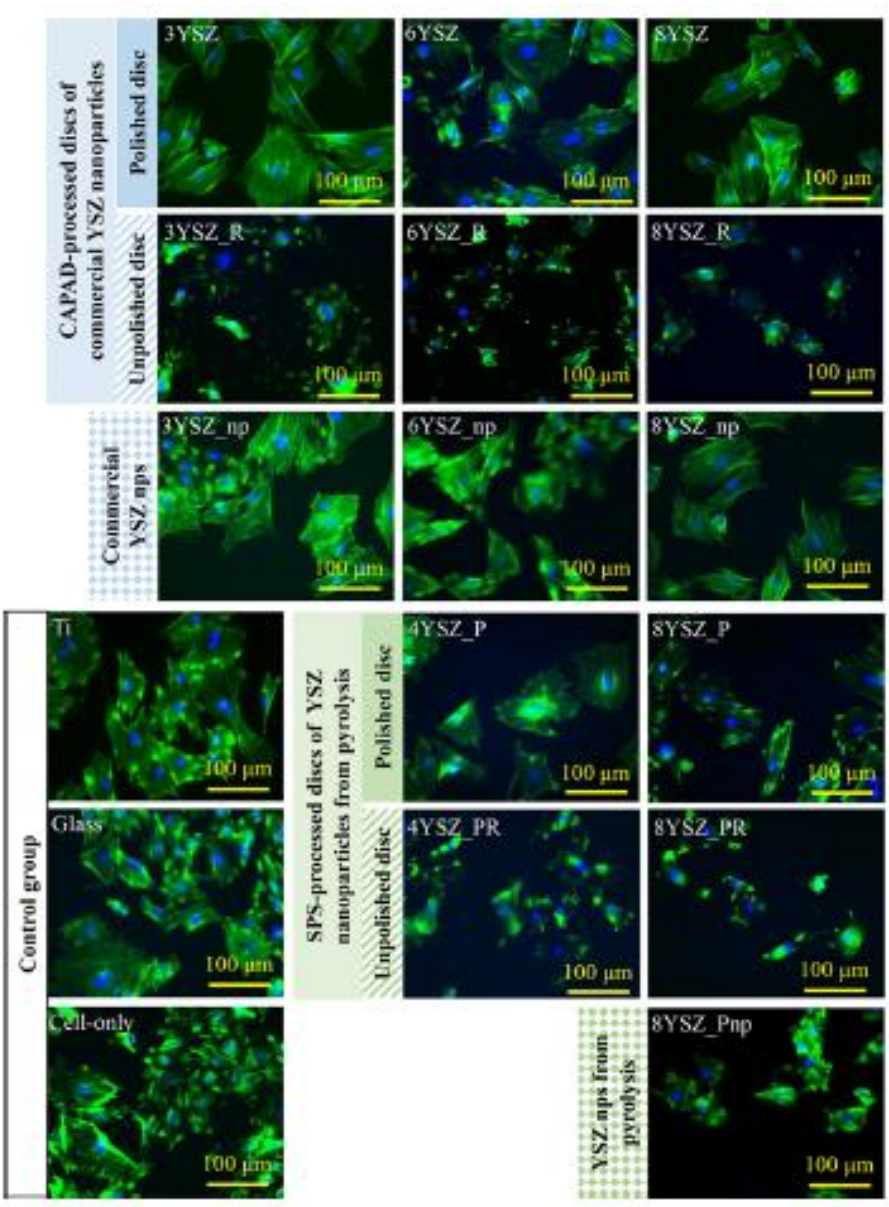


*Figure 5.5. Representative fluorescence images after 24-hour direct culture with the green color indicating Alexa Flour 488-phalloidin-stained cell cytoskeleton and the blue color indicating DAPI-stained cell nuclei. The BMSCs are adhered on YSZ discs as well as other reference and control groups.*

The water contact angles of the YSZ discs before and after polishing was investigated next and shown in figure 4b. There was no statistical difference between the samples as the water contact angle was all within the range of 79.5 to 84.9° and the photographs of the 10 μL droplets are shown on top.

After the samples were polished, the surface roughness and topography were the same across the CAPAD and SPS processed YSZ discs as shown in figures 3 and 4. There was no statistical difference in the hydrophilicity of the samples shown in figure 4b. The water contact angle was detected and determined to be statistically the same for both polished and unpolished YSZ discs.

After 24 hours of direct culture, figure 5 shows the florescence images of BMSCs stuck to the YSZ discs as well as the control group. The green color is from Alexa Flour 488-phalloidin-stained cell cytoskeleton and the blue color is from DAPI-stained cell nuclei. All the tested materials including YSZ discs, Ti, class and the cell only group had similar morphology of BMSC's. The only one that exhibited less spreading was the unpolished YSZ discs and the 8YSZ_Pnp nanoparticle synthesized in lab. The commercial nanoparticle tests with 3YSZ_np, 6YSZ_np, and 8YSZ_np all had comparable morphology with BMSC controls.

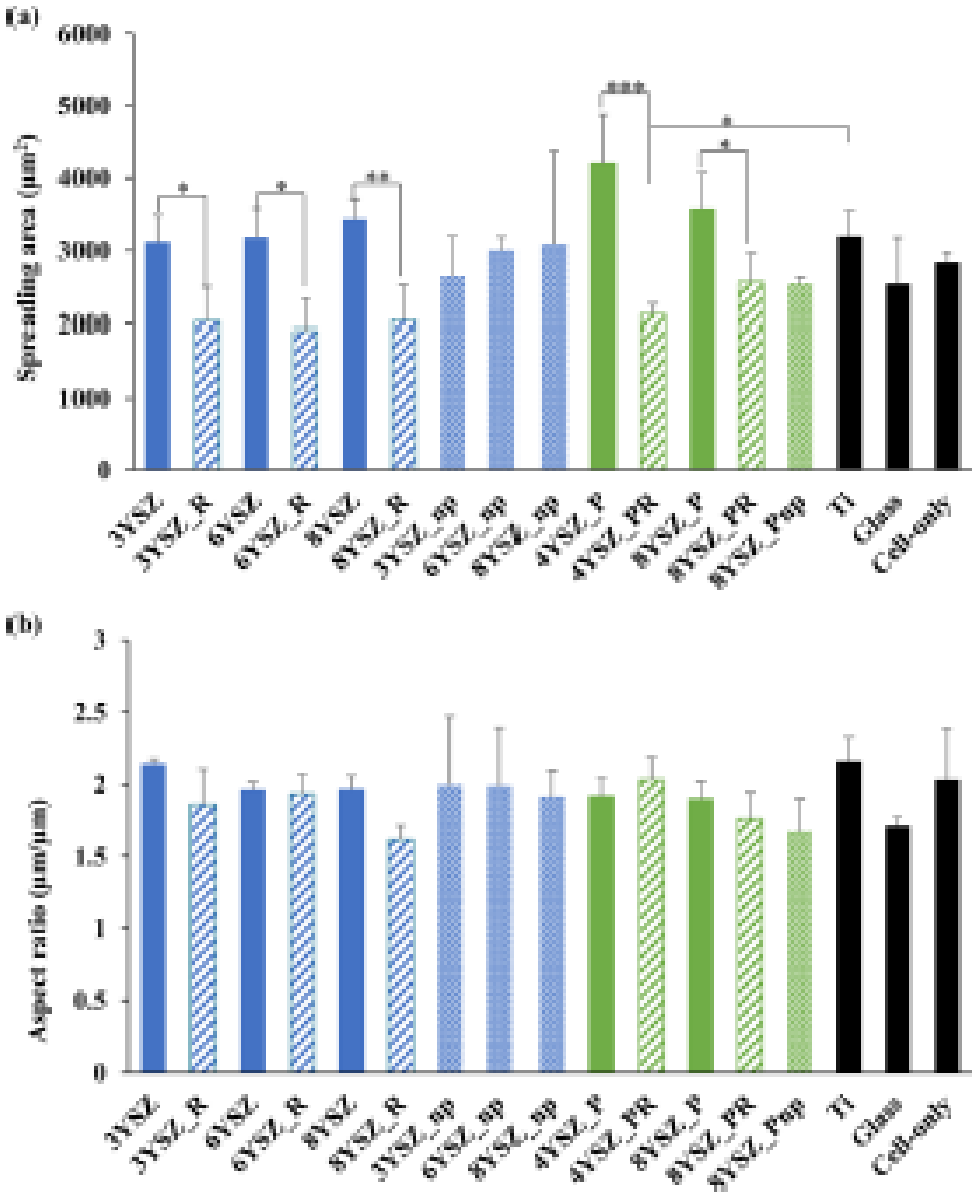


*Figure 5.6. (a) Spreading areas and (b) aspect ratios of BMSC adhered on YSZ discs, Ti controls, and the Glass references after 24 hours of direct culture. Additionally, nanoparticle controls and cell only controls are displayed as well. Data is shown as a mean ± standard deviation (n = 3), *p < 0.05, **p < 0.01, and ***p < 0.001.*

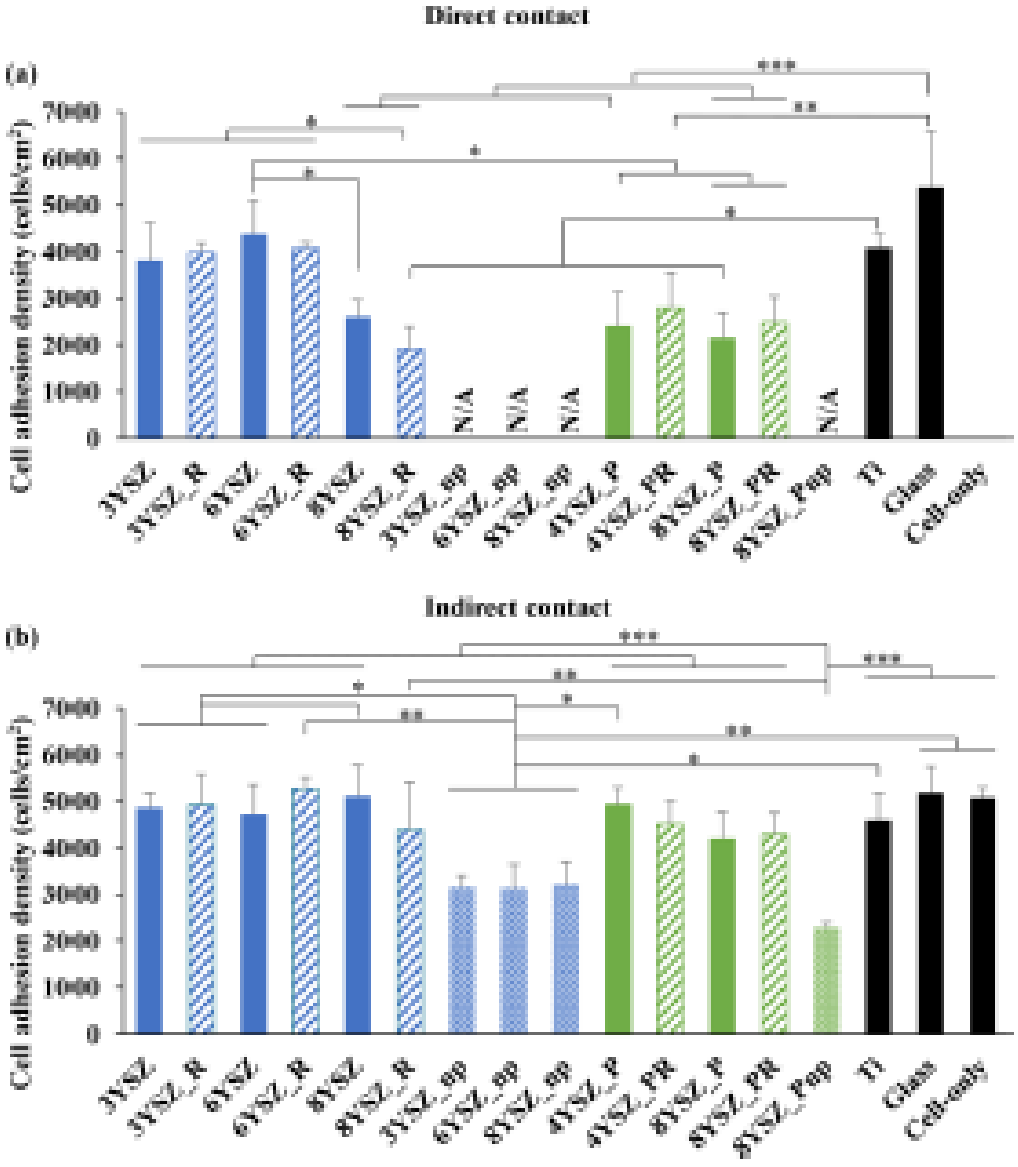


*Figure 5.7. (a) Direct contact densities of BMSCs adhere on the YS discs, Ti controls and Glass Reference after 24-hour direct culture. (b) Indirect contact densities of BMSCs adhered on the well-plates surrounding the samples and control references including the cell only comparison. Data is shown as a mean ± standard deviation (n = 3), *p < 0.05, **p < 0.01, and ***p < 0.001.*

Figure 6a displays the quantified data plotting the average spreading area and aspect ratio of BMSCs. All of the spreading areas were statistically greater in the polished samples than

the unpolished ones. The spreading areas was statistically the same as the Ti control for all the samples except that of 4YSZ_PR which was smaller. Figure 6b shows the aspect ratios of the BMSCs on all the different YSZ samples to be between 1.62-2.16 with no statistical difference between them.

Yang et al. compared the osteoblast spreading area on nanocrystalline diamond and microcrystalline diamond finding that the osteoblast spreading area was almost 2 times greater than nanocrystalline diamond. The spreading was deflected by larger grains while moving over smaller grains without a problem. Additionally, Yang et al. found that a rougher surface inhibits the spread of cells.[27] This is in agreement with our findings that polished YSZ discs had larger spreading areas than the unpolished discs that had the same composition.

Figure 7a shows the densities of BMSCs in the direct contact condition for the YSZ discs, Ti controls and a glass reference. Under direct contract conditions, the polished discs showed no statistical difference when compared with unpolished discs of the same composition. Both polished discs (8YSZ, 4YSZ_P, and 8YSZ_P) as well as unpolished ones (8YSZ_R, 4YSZ_PR and 8YSZ_PR) showed statistically lower BMSC adhesion densities than the Glass reference. Additionally, the 8YSZ_R and 8YSZ_P discs had statistically lower densities than the Ti control group. Polished and unpolished 3YSZ, 3YSZ_R, 6YSZ, 6YSZ_R were the only sample that did not have cell adhesion densities lower than either the glass or Ti reference under direct contact conditions.

Figure 7b displays the BMSC adhesion densities under indirect contact conditions on the culture plates. As expected, the YSZ discs had larger adhesion density than the nanoparticle

samples. Polished discs and unpolished discs of the same composition showed similar BMSC adhesion densities. The only adhesion density that was statistically less than all the other YSZ discs and that of Ti and Glass was 8YSZ_Pnp. No statistical difference was measured between the YSZ discs and the controls of Ti, Glass and Cell-only but the nanoparticle controls were statistically lower.

Although it is unlikely that densified YSZ discs would release nanoparticles, nanoparticles are known to have a dosage dependent cytotoxicity.[28] It is known from a previous study that when BMSCs were cultured with 10-60 mM YSZ nanoparticles the average cell adhesion density was lower than the BMSC-only control group.[20] This is confirmed in figure 7b where the nanoparticle control groups had lower cell adhesion densities under indirect contact conditions. YSZ densified discs are regarded as nondegradable materials and not expect to release nanoparticles. The concentration used in the control groups (10 mM) is a larger number of nanoparticles than expected to be degraded in the application.

The pH values of post culture media as well as the ion concentrations of $Zr^{4+}$ and $Y^{3+}$ are analyzed in figure 8. Figure 8a displays the pH values in a narrow range between 8.05-8.24 with some statistical differences. Figure 8b shows that the nanoparticle control groups, 3YSZ_np, 6YSZ_np, 8YSZ_np, and 8YSZ_Pnp, had statistically higher $Zr^{4+}$ concentrations than all the YSZ discs except 3YSZ as well as the other Ti, Glass, Cell-only and Media-only controls. The 3YSZ disc had a lower $Zr^{4+}$ concentration than the nanoparticle groups with an average of $1.45 \pm 0.69$ μM ($0.13 \pm 0.06$ mg/L). Figure 8c, displays that the YSZ samples with synthesized nanoparticles densified with SPS have a higher average $Y^{3+}$ concentration than CAPAD YSZ discs. The 8YSZ_Pnp that were

synthesized in house had the highest $Y^{3+}$ concentration, statistically greater than all the other commercially bought nanopowder samples, with a concentration of 13.62 ± 6.97 μM (1.21 ± 0.62 mg/L).

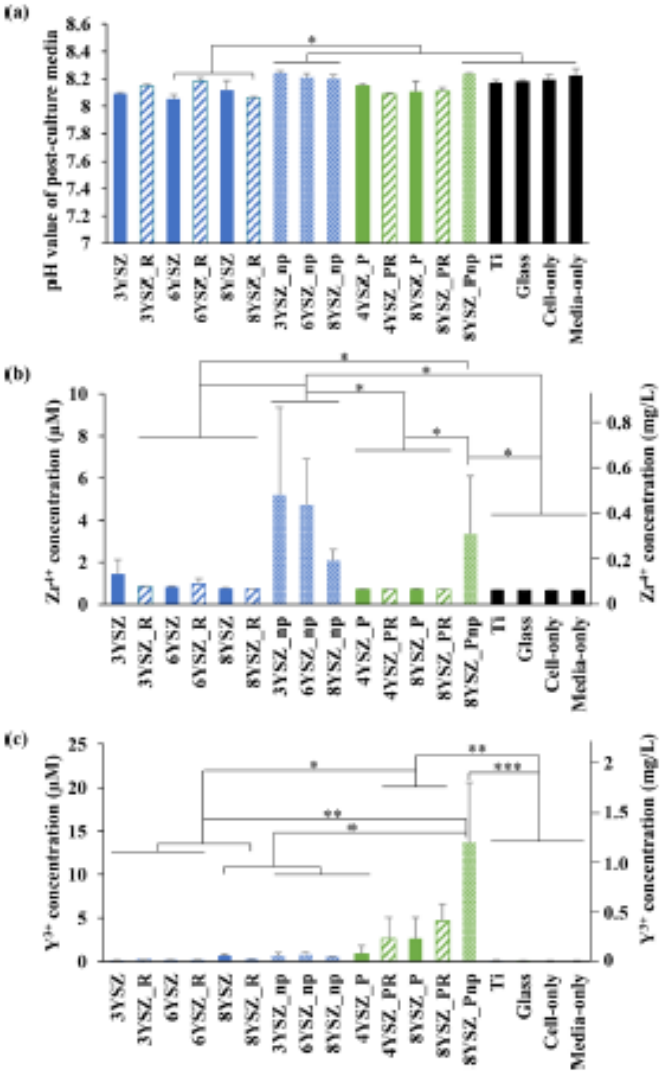


*Figure 8. (a) pH values of post culture media. (b) Zr4+ and (c) Y3+ ion concentrations in post culture media after 24-hour direct culture. Data is shown as a mean ± standard deviation (n = 3), *p < 0.05, **p < 0.01, and ***p < 0.001.*

The standard pH value for post culture media is in the range of 7.2-7.4 while we measured values slightly higher in the range of 8.05-8.24. The 5% $CO_2$ in the incubator works to keep the pH relatively neutral at 7.4. The YSZ discs in the culture sometimes release $Zr^{4+}$ and $Y^{3+}$ ions which can affect the pH and thus manipulating the BMSC adhesion and morphology in the indirect contact condition. To determine whether the increased value of pH that we measured was a result of the materials released from the YSZ, a media-only control was used. The media only control had a similar pH value as that of the YSZ ceramics demonstrating that the YSZ was not the source of higher pH values. The raised pH value is likely due to the evaporation of $CO_2$ when the media is moved outside the incubator.

Releasing of ions such as $Zr^{4+}$ and $Y^{3+}$ could have adverse effects on the cytocompatibility with BMSCs. Figure 7a shows how both the polished (8YSZ, 4YSZ_P, and 8YSZ_P) and unpolished (8YSZ_R, 4YSZ_PR, and 8YSZ_PR) groups showed lower average cell adhesion density than other YSZ samples under direct contact conditions. This could be attributed to higher average $Y^{3+}$ concentrations from those same samples in the post culture media as shown in figure 8c. BMSCs under direct contact conditions could be exposed to higher $Y^{3+}$ concentrations since there are more $Y^{3+}$ ions closer to the YSZ sample. However, the average $Y^{3+}$ concentrations were in a safe range (lower than 10 μM) for those groups which explains the similar BMSC adhesion densities for all the samples in indirect contact conditions.

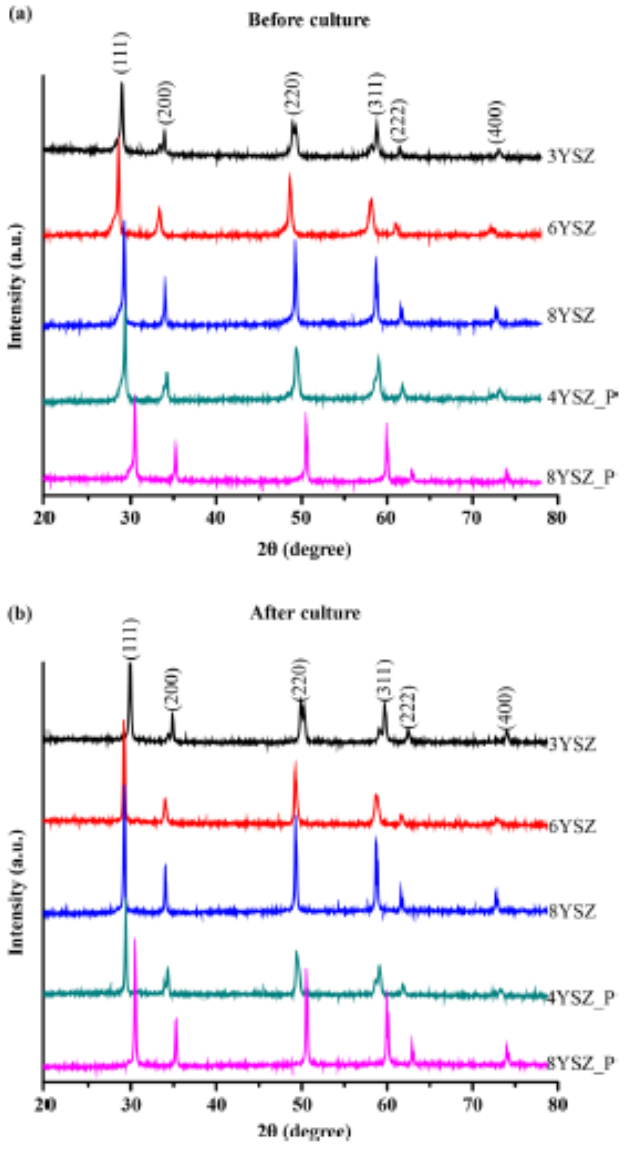


*Figure 9. XRD spectra of polished YSZ (a) before and (b) after 24-hour cell culture.*

The XRD spectra is shown in figure 9 has before (a) and after (b) the 24h cell culture. The spectra look the same with crystal planes of (111), (200), (220), (311), (222), and (400) meaning that the material stayed stable with no mineral depositions throughout the 24 h culture study.

## 5.4: Conclusions

As the cranial window is implemented, strong mechanical properties and biocompatibility are important but maintaining transparency on the window determines the potential applications. Therefore, preventing scratches from occurring which could greatly reduce the transparency by scattering the light. Polymeric cranial windows, glasses such as pyrex do not have the wear resistance that YSZ discs have. While the implant is inserted in the cranium, other factors may decrease the transparency such as mineral deposition and cell adhesion. The mechanical properties and cytocompatibility of commercially available ALON discs were investigated by Bodhak et al. for orthopedic applications.[29] While ALON has good transparency and hardness (15.14 ± .46 GPa), the adhesion density of human fetal osteoblast cells (hFOB) on the ALON discs was significantly higher than that on the control of titanium along with deposition of minerals meaning it lacked the necessary cytocompatibility.[29] The XRD spectra shown in Figure 9 after 24 h of cell culture indicated that there was no mineral deposition from the YSZ discs. Additionally, the polished discs of 8YSZ, 8YSZ_P and 4YSZ_P had lower cell adhesion densities than any of the other YSZ samples, the Ti control and glass reference under direct contact conditions indicating they might be able to retain their transparency longer.

The potential for YSZ discs to be use for cranial window applications was investigated in this article in terms of composition, processing, microstructure, surface properties and cytocompatibility. Generally, YSZ disc groups showed good cytocompatibility with BMSCs in addition to no mineral deposition on the surface after cell culture. The samples

of polished 8YSZ, 4YSZ_P and 8YSZ_P look to be the best samples due to their lower BMSC adhesion density than the other groups meaning they could maintain their transparency for longer time. On the other hand, 4YSZ_P and 8YSZ_P released more $Y^{3+}$ ions indicated potential problems with cytotoxicity in long term cell cultures. Leaving 8YSZ as the best option for cranial window applications in terms of transparency, cytocompatibility, cell adhesion density, $Y^{3+}$ ion release and mineral deposition. Further studies will be needed including clinical trials to further evaluate the potential for 8YSZ as a cranial window application.

## 5.5: References


(1) Bener, A.; Omar, A. O. K.; Ahmad, A. E.; Al-Mulla, F. H.; Abdul Rahman, Y. S. The Pattern of Traumatic Brain Injuries: A Country Undergoing Rapid Development. *Brain Inj.* **2010**, *24* (2), 74–80. https://doi.org/10.3109/02699050903508192.

(2) Xue, D.; Wang, Y.; Zhang, H. Advances of NIR Light Responsive Materials for Diagnosis and Treatment of Brain Diseases. *Adv. Opt. Mater.* **2023**, *2202888*, 2202888. https://doi.org/10.1002/adom.202202888.

(3) Rotunda, A. M.; Bhupathy, A. R.; Rohrer, T. E. The New Age of Acne Therapy: Light, Lasers, and Radiofrequency. *J. Cosmet. Laser Ther.* **2004**, *6* (4), 191–200. https://doi.org/10.1080/14764170410008124.

(4) Rozhkova, E. A. Nanoscale Materials for Tackling Brain Cancer: Recent Progress and Outlook. *Adv. Mater.* **2011**, *23* (24), 136–150. https://doi.org/10.1002/adma.201004714.

(5) Pan, W. T.; Liu, P. M.; Ma, D.; Yang, J. J. Advances in Photobiomodulation for Cognitive Improvement by Near-Infrared Derived Multiple Strategies. *J. Transl. Med.* **2023**, *21* (1), 135. https://doi.org/10.1186/s12967-023-03988-w.

(6) Heo, C.; Park, H.; Kim, Y. T.; Baeg, E.; Kim, Y. H.; Kim, S. G.; Suh, M. A Soft, Transparent, Freely Accessible Cranial Window for Chronic Imaging and Electrophysiology. *Sci. Rep.* **2016**, *6* (February), 1–11. https://doi.org/10.1038/srep27818.

(7) Cramer, S. W.; Carter, R. E.; Aronson, J. D.; Kodandaramaiah, S. B.; Ebner, T. J.; Chen, C. C. Through the Looking Glass: A Review of Cranial Window Technology for Optical Access to the Brain. *Journal of Neuroscience Methods*. 2021. https://doi.org/10.1016/j.jneumeth.2021.109100.

(8) McElhaney, J. H.; Fogle, J. L.; Melvin, J. W.; Haynes, R. R.; Roberts, V. L.; Alem, N. M. Mechanical Properties of Cranial Bone. *Journal of Biomechanics*. 1970. https://doi.org/10.1016/0021-9290(70)90059-X.

(9) Lee, W. S.; Yeo, K. S.; Andriyana, A.; Shee, Y. G.; Mahamd Adikan, F. R. Effect of Cyclic Compression and Curing Agent Concentration on the Stabilization of Mechanical Properties of PDMS Elastomer. *Materials and Design*. 2016, pp 470–475. https://doi.org/10.1016/j.matdes.2016.02.049.

(10) Sakuma, T.; Yoshizawa, Y. I.; Suto, H. The Microstructure and Mechanical Properties of Yttria-Stabilized Zirconia Prepared by Arc-Melting. *J. Mater. Sci.* **1985**, *20* (7), 2399–2407. https://doi.org/10.1007/BF00556069.

(11) Anselmi-Tamburini, U.; Woolman, J. N.; Munir, Z. A. Transparent Nanometric Cubic and Tetragonal Zirconia Obtained by High-Pressure Pulsed Electric Current Sintering. *Adv. Funct. Mater.* **2007**, *17* (16), 3267–3273. https://doi.org/10.1002/adfm.200600959.

(12) Sevilla, P.; Sandino, C.; Arciniegas, M.; Martínez-Gomis, J.; Peraire, M.; Gil, F. J. Evaluating Mechanical Properties and Degradation of YTZP Dental Implants. *Materials Science and Engineering C*. 2010, pp 14–19. https://doi.org/10.1016/j.msec.2009.08.002.

(13) Chevalier, J.; Deville, S.; Münch, E.; Jullian, R.; Lair, F. Critical Effect of Cubic Phase on Aging in 3 Mol% Yttria-Stabilized Zirconia Ceramics for Hip Replacement Prosthesis. *Biomaterials* **2004**, *25* (24), 5539–5545. https://doi.org/10.1016/j.biomaterials.2004.01.002.

(14) Ou, S. F.; Huang, M. S.; Chiou, S. Y.; Ou, K. L. Research of Antibacterial Activity on Silver Containing Yttria-Stabilized-Zirconia Bioceramic. *Ceramics International*. 2013, pp 3591–3596. https://doi.org/10.1016/j.ceramint.2012.10.186.

(15) Kohal, R. J.; Wolkewitz, M.; Hinze, M.; Han, J. S.; Bächle, M.; Butz, F. Biomechanical and Histological Behavior of Zirconia Implants: An Experiment in the Rat. *Clin. Oral Implants Res.* **2009**, *20* (4), 333–339. https://doi.org/10.1111/j.1600-0501.2008.01656.x.

(16) Garvie, R. C.; Hannink, R. H.; Pascoe, R. T. Ceramic Steel? *Nature* **1975**, *258* (5537), 703–704. https://doi.org/10.1038/258703a0.

(17) Rudnicki, C.; Exarhos, S.; Mariano, C.; Mangolini, L. Spray Pyrolysis of Yttria-Stabilized Zirconia Nanoparticles and Their Densification into Bulk Transparent Windows. *J. Nanoparticle Res.* **2020**, *22* (2). https://doi.org/10.1007/s11051-020-4766-0.

(18) Alaniz, J. E.; Perez-Gutierrez, F. G.; Aguilar, G.; Garay, J. E. Optical Properties of Transparent Nanocrystalline Yttria Stabilized Zirconia. *Opt. Mater. (Amst).* **2009**, *32* (1), 62–68. https://doi.org/10.1016/j.optmat.2009.06.004.

(19) Zhang, C.; Lin, J.; Nguyen, N. Y. T.; Guo, Y.; Xu, C.; Seo, C.; Villafana, E.; Jimenez, H.; Chai, Y.; Guan, R.; Liu, H. Antimicrobial Bioresorbable Mg-Zn-Ca Alloy for Bone Repair in a Comparison Study with Mg-Zn-Sr Alloy and Pure Mg. *ACS Biomater. Sci. Eng.* **2020**, *6* (1), 517–538. https://doi.org/10.1021/acsbiomaterials.9b00903.

(20) Rutherford, D.; Exarhos, S.; Xu, C.; Niacaris, M.; Mariano, C.; Dayap, B.; Mangolini, L.; Liu, H. Synthesis, Characterization, and Cytocompatibility of Yttria Stabilized Zirconia Nanopowders for Creating a Window to the Brain. *J. Biomed.*

*Mater. Res. - Part B Appl. Biomater.* **2020**, *108* (3), 925–938. https://doi.org/10.1002/jbm.b.34445.

(21) Ilavsky, J.; Stalick, J. K. Phase Composition and Its Changes during Annealing of Plasma-Sprayed YSZ. *Surf. Coatings Technol.* **2000**, *127* (2–3), 120–129. https://doi.org/10.1016/S0257-8972(00)00562-4.

(22) Klimke, J.; Trunec, M.; Krell, A. Transparent Tetragonal Yttria-Stabilized Zirconia Ceramics: Influence of Scattering Caused by Birefringence. *J. Am. Ceram. Soc.* **2011**, *94* (6), 1850–1858. https://doi.org/10.1111/j.1551-2916.2010.04322.x.

(23) Apetz, R.; Van Bruggen, M. P. B. Transparent Alumina: A Light-Scattering Model. *J. Am. Ceram. Soc.* **2003**, *86* (3), 480–486. https://doi.org/10.1111/j.1151-2916.2003.tb03325.x.

(24) Kodera, Y.; Hardin, C. L.; Garay, J. E. Transmitting, Emitting and Controlling Light.Pdf. Scripta Materiala 2013, pp 149–154.

(25) Bond, D. M.; Zikry, M. A. Differentiating between Intergranular and Transgranular Fracture in Polycrystalline Aggregates. *J. Mater. Sci.* **2018**, *53* (8), 5786–5798. https://doi.org/10.1007/s10853-017-1847-2.

(26) Davoodzadeh, N.; Cano-Velázquez, M. S.; Halaney, D. L.; Sabzeghabae, A.; Uahengo, G.; Garay, J. E.; Aguilar, G. Characterization of Ageing Resistant Transparent Nanocrystalline Yttria-Stabilized Zirconia Implants. *J. Biomed. Mater. Res. - Part B Appl. Biomater.* **2020**, *108* (3), 709–716. https://doi.org/10.1002/jbm.b.34425.

(27) Yang, L.; Gong, Z.; Lin, Y.; Chinthapenta, V.; Li, Q.; Webster, T. J.; Sheldon, B. W. Disordered Topography Mediates Filopodial Extension and Morphology of Cells on Stiff Materials. *Adv. Funct. Mater.* **2017**, *27* (38), 1–9. https://doi.org/10.1002/adfm.201702689.

(28) Wetteland, C. L.; Nguyen, N. Y. T.; Liu, H. Concentration-Dependent Behaviors of Bone Marrow Derived Mesenchymal Stem Cells and Infectious Bacteria toward Magnesium Oxide Nanoparticles. *Acta Biomater.* **2016**, *35*, 341–356. https://doi.org/10.1016/j.actbio.2016.02.032.

(29) Bodhak, S.; Balla, V. K.; Bose, S.; Bandyopadhyay, A.; Kashalikar, U.; Jha, S. K.; Sastri, S. In Vitro Biological and Tribological Properties of Transparent Magnesium Aluminate (Spinel) and Aluminum Oxynitride (ALON ®). *J. Mater. Sci. Mater. Med.* **2011**, *22* (6), 1511–1519. https://doi.org/10.1007/s10856-011-4332-5.

## Chapter 6: Conclusion and Outlook

The work in this dissertation investigated the application of two different nanomaterials and their application potential to improve public health. ZrN demonstrates efficient use of the sun's green energy source for the purpose of removing heavy metals contaminating water. YSZ is proposed and comprehensively investigated to optimize the mechanical properties of 3YSZ with the optical properties of 8YSZ for a ceramic cranial implant or a "Window to the Brain". The implant would allow for improved diagnostic and treatments for the rising number of brain injuries in the world. I will now comment on the viability of these applications of ZrN and YSZ to contribute to public health.

In chapter 2, I demonstrated that ZrN achieved more efficient reduction of chromium (VI) than the more commonly used semiconductor $TiO_2$ without an additional cancerous catalysis like methanol. I measured a reasonable quantum yield with ZrN in the visible part of the spectrum meaning that ZrN is able to oxidize the water to facilitate the reduction of the heavy metal chromium (VI). Material characterizations and experiments in the dark provide convincing evidence that ZrN is not participating in the reaction in addition to thermal experiments in the dark that rule out major photothermal contributions.

In chapter 3, the reduction kinetics of ZrN in solutions with water and methanol is investigated and compared with another alternative plasmonic material, TiN in using visible radiation to reduce platinum (IV). ZrN is shown to have more potential as a photocatalytic material with visible radiation than TiN. However, TiN has a potential for NIR applications because the plasmonic response that is closer to the biological windows. Then ZrN is compared to $TiO_2$ in the removal of chromium (VI) in solutions but with

methanol to facilitate the reaction. ZrN demonstrates a practical quantum yield with visible radiation and even demonstrates a higher quantum yield than $TiO_2$ in the far UV.

Chapters 2 and 3 I discuss the mechanisms which plasmonic particles, specifically ZrN, are able to photocatalyzed reactions. I comprehensively investigate the reduction kinetics as a function of illumination power and found a sub-linear dependance that is consistent with the photogeneration of charge carriers. Furthermore, the solution must reach a temperature in the dark much higher than it achieved when the solution is illuminated to have the same reduction rate. Future work should continue to investigate the photothermal properties of plasmonic nanoparticles by attempting to directly measure the temperature of the particles.

Zirconium Nitride is proposed as an alternative plasmonic material to efficiently use a wide spectrum the suns energy for the removal of heavy metals from solution. However, research suggests that nanoparticles are potentially harmful to human health removing the environmental flair to apply ZrN for water purification. It is important as well to take into account the energy needed for both the removal of nanoparticles from water and already high energy production of plasmonic nanoparticles to do a full environmental impact.

In chapter 4, the synthesis and densification of YSZ nanopowder was investigated. First, I optimized the YSZ synthesis such that we have both control over the composition of the material as well as the size of the particles. Then I combine the mechanical properties of 3YSZ with the optical properties of 8YSZ by synthesizing 6YSZ nanopowders and densified them using a Spark Plasma Sintering process that uses fast heating rates and a lot of pressure to solidify the powder into a puck. The 6YSZ was compared with an 8YSZ

nanostructured ceramic cranial implant and find that further investigations should continue to try to optimize the balance.

Chapter 4 screened the cytocompatibility for YSZ cranial implants using commercial powder densified with a CAPAD process and in house synthesized particles densified with an SPS process. The results here point to the problem both having an optical transparent but as the skin and bio tissues grow, they also block light. I determine in this work that 8YSZ seems to be the best option in terms of the optical transparency, mechanical properties, and cytocompatibility however long-term studies need to investigate the commercial viability as well as the potential harm to the environment.

Chapters 3-4 were part of a collaboration containing nine research labs across Southern California and Mexico focusing on nanopowder synthesis, densification, characterization, waveguide writing, optical fibers, antibacterial studies, biocompatibility, cytocompatibility, imaging and therapy. Collaborative work is important science for the pursuit of knowledge, but the cranial implant seems to only provide limited optical access of the brain even optimized. That NIR wavelengths are able to pass through skin without damage already.

Scientific research opens the potential for technology to improve public health but it is important to be critical of the cost and the cradle-to-gate energy demand of these materials. If plasmonic particles are able to more efficiently facilitate chemical reactions than current methods, I propose whether the energy cost in production greater than that which is saved? Is the cost to research for certain applications the best use of resources to improve public health?